

Aus der Klinik für Anästhesiologie und Operative Intensivmedizin

der Medizinischen Fakultät Mannheim
Direktor: Prof. Dr. med. Manfred Thiel

Characterization of muscle tissue in sepsis induced mouse models

Inauguraldissertation
zur Erlangung des akademischen Grades
Doctor scientiarum humanarum (Dr. sc. hum.)
der
Medizinischen Fakultät Mannheim
der Ruprecht-Karls-Universität
zu
Heidelberg

vorgelegt von
Marion Patrick Ivey Williams

aus
Florence, South Carolina
2021

Dekan: Prof. Dr. med. Sergij Goerd
Referent: Prof. Dr. med. Manfred Thiel

Table of Contents

Abbreviations	1
1. Introduction	4
1.1 Confocal microscopy and optical resolution	4
1.1.1 The vertical turn, light sheet imaging techniques	8
1.1.2 Fluorescence and the behavior of light	11
1.2 Tissue clearing.....	13
1.2.1 Organic solvents	15
1.2.2 High refractive index aqueous solutions	18
1.2.3 Hyperhydrating solutions	18
1.2.4 Tissue transformation.....	19
1.3 Sepsis.....	20
1.3.1 Animal models of sepsis	25
1.3.2 Lipopolysaccharide, a model for endotoxemia	26
1.3.3 Cecal ligation and puncture and colon ascendens stent peritonitis	27
1.3.4 Cecal slurry	29
1.3.5 Less common models of sepsis	31
1.4 Muscle anatomy and sepsis induced myopathies and neuropathies.....	31
1.4.1 General muscle anatomy	31
1.4.2 Muscle innervation and the neuromuscular junction	34
1.4.3 Sepsis, muscle, and the intensive care unit	35
1.4.4 The imbalance between muscle regeneration and degradation in septic induced muscle wasting	36
1.4.5 Risk factors contributing to muscle atrophy within the intensive care unit	37
1.4.6 Animal models outside of sepsis to investigate specific mechanisms which contribute to muscle dysfunction and atrophy	39
2. Aims of the study	42
3. Material and Methods	43
4. Results	54
4.1 MYOCLEAR, a reliable SDS-free hydrogel-based clearing protocol which retains NMJ staining	54
4.1.1 Green/red autofluorescence and spectral unmixing of near-infrared fluorescence signals enable the visualization of muscle fibers, nuclei, and NMJs	58
4.1.2 Whole mount analysis of MYOCLEAR processed MDX muscle allows for the detection of local NMJ fragmentation index heterogeneity	60
4.1.3 VACHT antibody staining confirms the integrity of the NMJ presynaptic apparatus upon MYOCLEAR	62
4.2 MYOCLEAR+ a PFA free hydrogel fixation protocol.....	64
4.2.1 Optimization of acrylamide/bis-acrylamide tissue fixation	66

4.2.2 DIMM, a reliable glycerol replacement for refractive index matching and mounting	67
4.2.3 Application of MYOCLEAR+ to tissues other than muscle.....	69
4.3 Cecal slurry model of sepsis.....	71
4.3.1 Evaluation of the cecal slurry model of sepsis as a systemic model and the classification of risk factors associated with muscle wasting	72
4.3.2 The cecal slurry model of sepsis, a reliable model for studying septic induced diaphragm dysfunction.....	76
4.3.3 Degradation of the sympathetic nervous system may contribute to NMJ instability and muscle dysfunction.....	78
4.3.4 Sepsis induces fibrosis in the diaphragm and an increase in typical western blotting “housekeeping” proteins	79
5. Discussion	81
5.1 MYOCLEAR, a reliable skeletal muscle tissue clearing protocol but with limitations	81
5.2 MYOCLEAR+, a promising approach for multi-channel LSFM acquisition.....	83
5.3 Cecal slurry model of sepsis, a robust animal model for evaluating muscle wasting....	85
6. Summary	89
7. Appendix	91
8. References	98
9. Curriculum Vitae and Publications	108
10. Acknowledgements	111

Abbreviations

2D	Two-dimensional
3D	Three-dimensional
3DISCO	3D imaging of solvent-cleared organs
A	Amps
AChR	Nicotinic acetylcholine receptor
ADP	Adenosine diphosphate
ADRB2	Beta-2 adrenergic receptor
ALT	Alanine aminotransferase
AOTF	Acousto-optic tunable filter
AST	Aspartate aminotransferase
ATP	Adenosine triphosphate
BABB	Benzyl alcohol:benzyl benzoate
BnP	Blocking and Permeabilization solution
CAD	Computer-aided design (software)
CARS	Compensatory Anti-inflammatory Response
CASP	Colon Ascendens Stent Peritonitis
CFU	Colony forming unit
CIM	Critical illness myopathy
CIP	Critical illness polyneuropathy
CIPM	Critical illness polyneuromyopathy
CLARITY	Clear Lipid-exchanged Acrylamide-hybridized Rigid imaging, Immunostaining, in-situ-hybridization-compatible Tissue hYdrogel
CLP	Cecal Ligation and Puncture
CS	Cecal slurry
CVP	Central venous pressure
DBE	Dibenzyl ether
DCM	Dichloromethane
DIMM	Deep Imaging Mounting Media
DLS	Digital light sheet
DMD	Duchenne muscular dystrophy
DMSO	Dimethyl sulfoxide
DMSO	Dimethyl sulfoxide
DNA	Deoxyribonucleic acid
ECi	Ethyl cinnamate
ECM	Extracellular matrix
EDL	Extensor digitorum longus
EDTA	Ethylenediaminetetraacetic acid
eMHC	Embryonic myosin heavy chain
ETC	Electrophoresis chamber
FACT	Fast free-of-acrylamide clearing tissue
FDISCO	DISCO with superior fluorescence-preserving capability

FRET	Förster resonance energy transfer
GAPDH	Glyceraldehyde 3-phosphate dehydrogenase
GB	Gigabyte
GFP	Green fluorescent protein
HCL	Hydrochloric Acid
i.p.	Intraperitoneal
ICU	Intensive care unit
ICUAW	ICU acquired weakness
iDISCO	Immunolabeling-enabled 3DISCO
IPM	Imipenem
IR	Infrared
kDa	Kilo Dalton
LPS	Lipopolysaccharide
LSFM	Light sheet fluorescence microscopy
M	Mole
MDX	Mouse model of Duchenne muscular dystrophy
MHC	Myosin heavy chains
MLC	Myosin light chains
MSS	Murine sepsis score
MuRF1	Muscle RING-finger protein-1
MW	Molecular weight
n	Refractive index
NA	Numerical aperture
NMJ	Neuromuscular junction
NO	Nitric oxide
PAMP	Pathogen associated molecular pattern
PBS	Phosphate buffered saline
PCT	Procalcitonin
PFA	Paraformaldehyde
pH	Potentia hydrogenii
PLA	Polylactic acid
PMT	Photomultiplier tube
PSF	Point spread function
qSOFA	Quick SOFA score
Quadrol	Aminoalcohol N,N,N',N'-Tetrakis(2-hydroxypropyl)ethylenediamine
RI	Refractive index
RNA	Ribonucleic acid
ROI	Region of interest
s.c.	Subcutaneous
sClarity	The stochastic electrotransport method of the CLARITY protocol
sCMOS	Scientific complementary metal-oxide-semiconductor
SD	Standard deviation
SDS	Sodium dodecyl sulfate

SIRS	Systemic inflammatory response
SNR	Signal-to-noise ratio
SNS	Sympathetic nervous system
SOFA	Sequential organ failure assessment
SSC	Surviving sepsis campaign
TB	Terabyte
TDE	2,2'-thiodiethanol
TH	Tyrosine Hydroxylase
THF	Tetrahydrofuran
TLR	Toll-like receptor
TNF- α	Tumor necrosis factor α
TOC	Tissue optical clearing
uDISCO	Ultimate DISCO
UPS	Ubiquitin-proteasome pathway
UTI	Urinary tract infection
VAcHT	Vesicular acetylcholine transporter
vDISCO	Nanobodies(V _H H)-boosted DISCO
w/v	Weight by volume
α -BGT	α -bungarotoxin

1. Introduction

1.1 Confocal microscopy and optical resolution

Driven by the desire to image biological events as they occurred in living tissue (*in vivo*), Marvin Minsky introduced the first scanning confocal microscope in 1955 (Minsky 1988). Although his work gained little interest at the time, his invention was later extended to dissected and preserved tissue (*in vitro*) and eventually led to the revolution of “optical sectioning” techniques such as: commercial laser scanning confocal microscopes, laser scanning 2-photon microscopy, parallelized confocal (spinning disk), computational image deconvolution methods, and light sheet approaches. This introduced several advantages over conventional widefield microscopy, such as, longer working distances, an increase in resolution, eliminating out-of-focus glare, and the ability to gather serial optical sections from thicker samples (Minsky 1988, Conchello and Lichtman 2005). In contrast to widefield microscopy, where a sample is flooded with light from a light source evenly over the whole sample, the aim of confocal microscopes is to illuminate the smallest spot possible with a concentrated light source in the plan of focus and is accomplished by a series of events, with a visual representation shown in Figure 1. First, a laser excitation source produces a beam of light at a certain wavelength. This beam then travels through the excitation pinhole and excitation filter. After, it is reflected off a dichromatic mirror and through the objective. The objective takes the excitation beam and focuses it on one distinct spot on one focal plane of the sample. Here, the excitation beam excites the fluorophores found in this area, and, in turn, these excited fluorophores give off emission light. This emitted light is then collected by the objective, refocused by the objective, and passed through the dichromatic mirror. Where it then goes through a fluorescence filter and a pinhole the objective focused it on. Lastly, the signal goes on to a photomultiplier tube (PMT), or hyD detector, where its intensity is multiplied and interpreted as pixels on a computer screen (Pawley 2006).

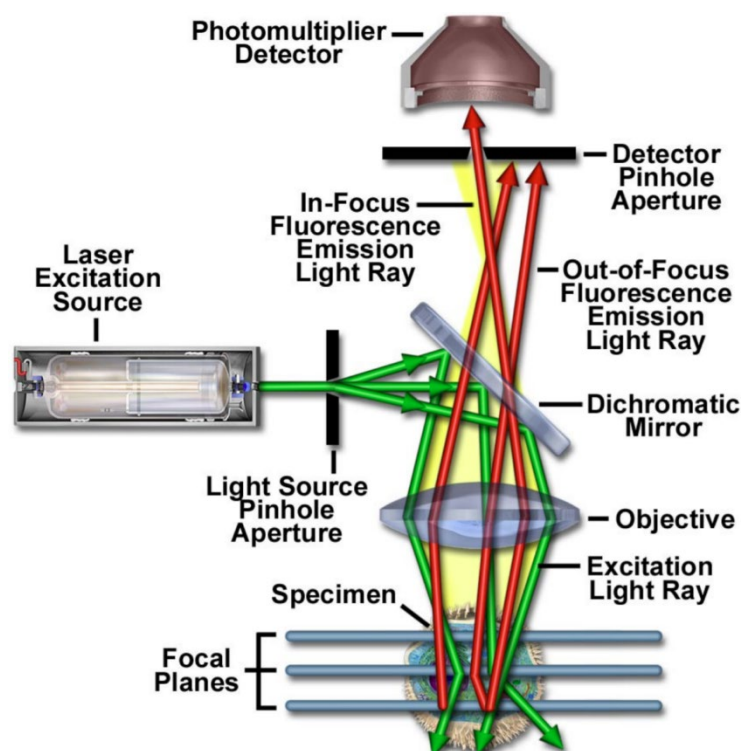


Figure 1 – Schematic diagram of the optical pathway and principal components of a laser scanning confocal microscope. Adapted from Claxton, Fellers et al. (2005) (Rights obtained for use).

For clarity, one can imagine a digital picture that is made up of 500x500 pixels. This single image can be designated as our optical section, i.e. the focal plane, in this analogy. A confocal microscope builds this digital picture, pixel by pixel, by applying the series of events described above to each pixel in the picture. While this single image is suitable when imaging extremely thin slices, more focal planes are needed for thick samples. This is known as optical sectioning and a confocal microscope can achieve this by refocusing the light source by a set distance above or below the focal plane and creates a new image from this plane. This “stack” of images is known as a “Z-stack” and can be collected, grouped, and displayed as one image in a three-dimensional (3D) representative model, Figure 2(A). While Z-stacks add depth, it only represents a small area in XY for large samples. Therefore, tile scanning has been introduced, which is the process of taking multiple Z-stacks over the whole sample, with a small overlap between each stack. These individual stacks are then stitched together to create a 3D representative model, Figure 2(B). In the past, this stitching process was only possible by tediously aligning each stack manually in post-processing (Legesse, Chernavskaia et al. 2015). However, many companies have now made embedded automatic stitching programs a built-in standard to their respective image acquisition software, such as the tile scan and LAS-X navigator function in Leica’s LAS-X software.

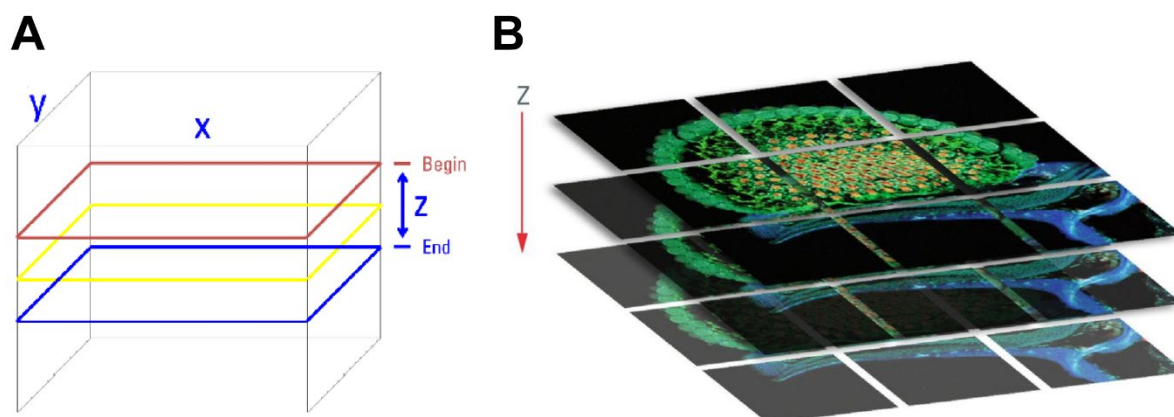


Figure 2 – Representation of a microscopy Z-stack and tile scan merging. Where (A) is a visual representation of a Z-stack and (B) of tile scan merging. Adapted from: www.Leica-Microsystems.com (2016)

Though, a confocal microscope's optical resolution, i.e. resolving power, or the absolute closest two signals can be with the microscope still able to distinguish them as separate signals, is not based on pixels, as it could be interpreted in the previous analogy, but is on a much smaller scale and is dependent on a few variables. Many assume the optical resolution of a microscope is strictly related to magnification, and while this may not even seem unreasonable, diffraction is what actually limits the resolving power of a microscope. Diffraction, or the bending of waves, occurs as light waves pass through a circular aperture, such as a microscope's pinhole. This results in a XY diffraction pattern consisting of a bright spot of light with a series of concentric rings, decreasing in intensity the further away the ring is from the center. This is known as an airy disk and is the smallest focused spot of light the objective can create, with its 3D diffraction pattern making up the point spread function (PSF), as shown in Figure 3(A and C). While in Z, the center of the bright spot is located at the so-called “waist” of an hourglass-shaped beam, Figure 3(B) (Pawley 2006).

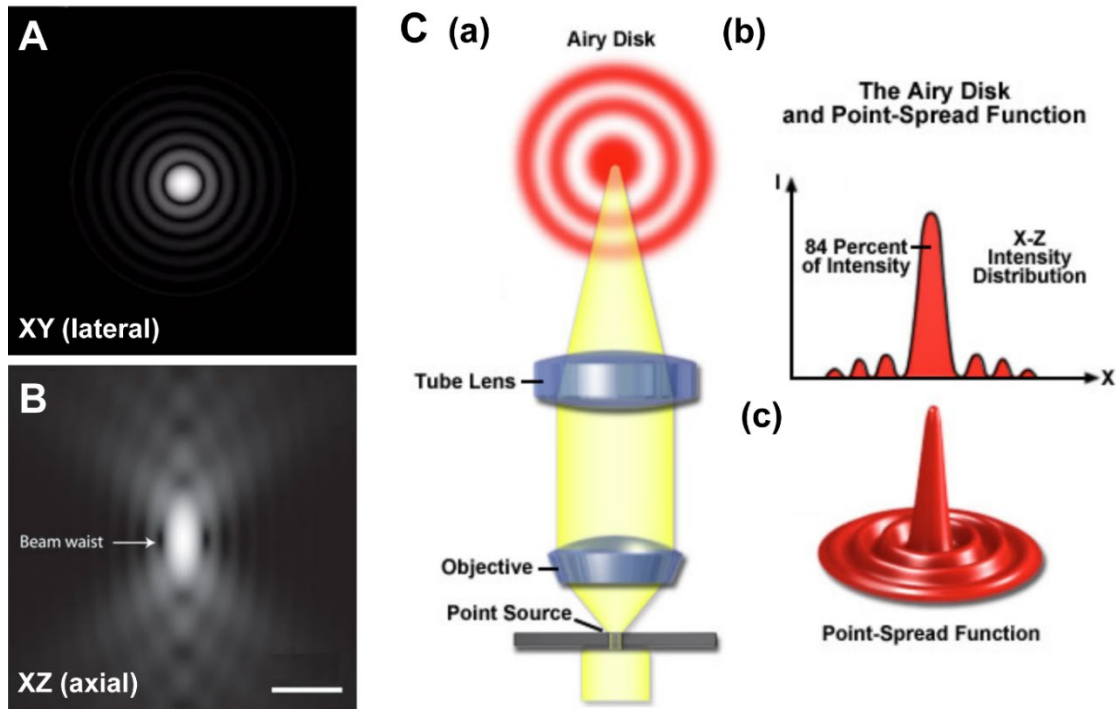


Figure 3 – Concepts of Microscopy. Depiction of an air disk in XY (A) and XZ (B). While (C) portrays the beam path in the creation of the airy disk (a), its relative intensity distribution (b), as well as a 3D representation of the PSF. Adapted from: (A) <https://www.ibiology.org/talks/resolution-in-microscopy/> (2020), (B) Conchello and Lichtman (2005) (rights permitted for use), and (C) <http://zeiss-campus.magnet.fsu.edu/print/basics/resolution-print.html> (2020)

The size of the airy disk, thereby the PSF, is dictated by an objectives numerical aperture and is defined as:

$$NA = (n) \sin(\alpha)$$

Equation 1 – calculating the numerical aperture of an objective. n = refractive index of the immersion medium, α = one-half the angle aperture.

To understand this effect, one needs to examine the extreme wavelets from a curved spherical wave in a high NA objective and a low NA objective in XZ, as shown in Figure 4(A and B). If compared, one can see that the NA directly effects the banding pattern, with the high NA objective giving rise to a shorter fringe period and narrower fringes. This is what limits the resolution, how fine an objective can produce this banding pattern. Thus, with a higher NA there is a wider separation between wavelets and, as a result, there is a smaller central peak. Whereas with a low NA, only a narrow separation between the wavelets is possible and gives rise to a broad central peak and less resolution. Moreover, higher NA objectives are also able to collect more of the emitted light from fluorescent samples due to their wider angle of aperture. A great example of this in XY can be seen in Figure 4(D), where it is clearly evident that the broader central peak generated by the lowest NA objective cannot differentiate between the fluorescent beads, whereas a higher NA objective is able to due to its smaller airy disk (Françon 1961, Conchello and Lichtman 2005, Pawley 2006).

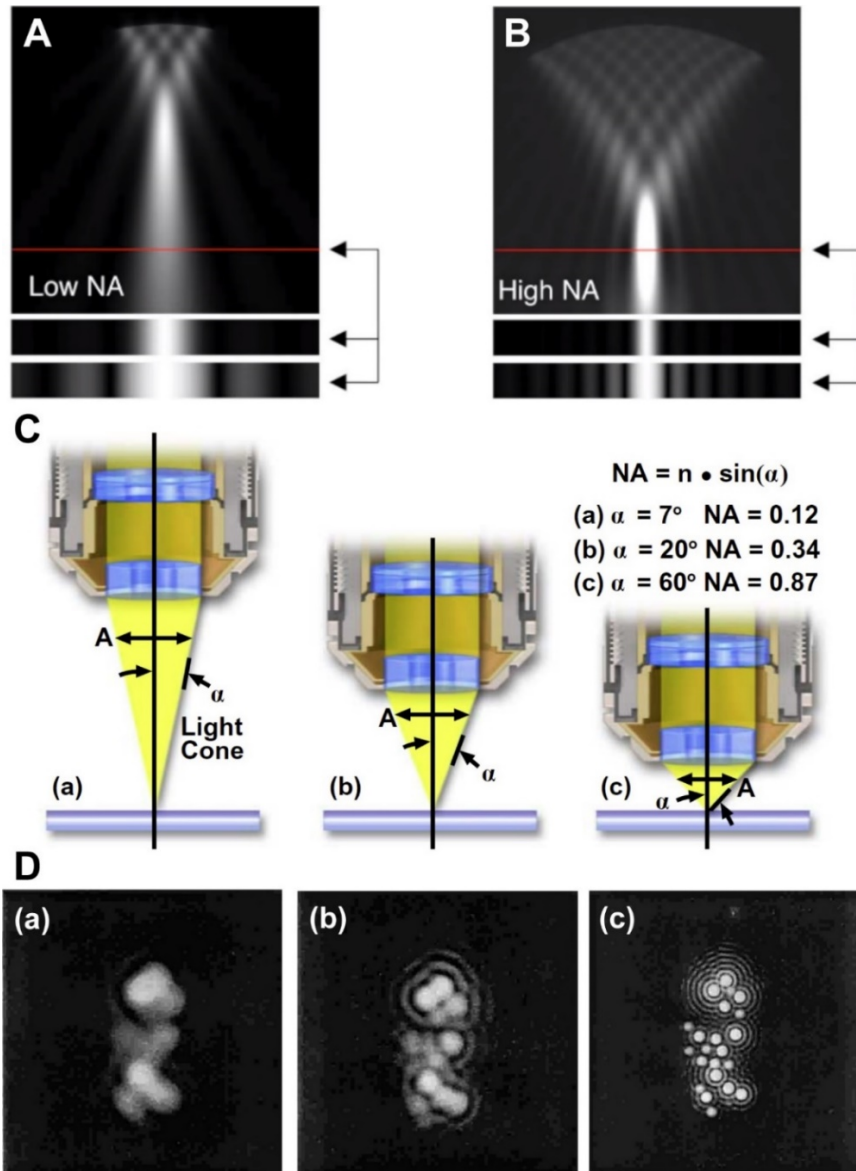


Figure 4 – The effects of Numerical Aperture on resolution. (A) low and (B) high NA objectives result in different banding patterns of diffracted light in XZ, with high NA objectives able to produce a wider separation between wavelets and a smaller central peak. This is due to (C) the higher NA objectives wider angular aperture (α) which allows for a more focused banding pattern while also collecting more of the emitted light. (D) depicts the effects of NA on the resolving power of an objective in XY while imaging the same beads with a (a) low, (b) average, and (c) high NA objective. Sources adapted from: (A and B) <https://www.ibiology.org/talks/resolution-in-microscopy/> (2020), (C) <https://www.microscopyu.com/microscopy-basics/numerical-aperture> (2020), and (D) Françon (1961)

While there is no generally accepted criterion for calculating the resolving power of an objective, most microscopists rely on the arbitrary Rayleigh criterion. This criterion is based on the distance from the center of the airy disk to the first dark ring and is calculated for both XY and Z as:

$$Resolution_{xy} = \frac{0.61(\lambda)}{NA}$$

$$Resolution_z = \frac{2(n)(\lambda)}{NA^2}$$

Equation 2 – Calculation for resolution in confocal microscopy. λ = wavelength, NA = numerical aperture, n = refractive index of the medium.

For example, an objective, no matter its magnification, with a NA of 1.4 using a 488 nm excitation laser can resolve two objects as close as 225 nm in XY and 861 nm in Z. Thus, a higher NA and shorter wavelength, correlate to a higher resolving power (Conchello and Lichtman 2005).

1.1.1 The vertical turn, light sheet imaging techniques

Although confocal microscopes have the benefit of high-resolution imaging, acquiring wholmount data, as one could assume, can be a lengthy endeavor as it takes a relatively long time to complete the scanning process. Indeed, many advances have been made to shorten imaging time, such as bidirectional scanning and the use of acousto-optic tunable filters (AOTF) (Conchello and Lichtman 2005). However, these advances are still not sufficient when considering the sheer size of wholmount samples. Moreover, the increased risk of bleaching is another potential concern when using confocal for thick samples. Bleaching is an irreversible photochemical alteration of a fluorophore molecule, making it unable to emit fluorescence. Depending on a fluorophore's chemistry, this can occur after absorbing just a few photons, with more robust fluorescent proteins able to undergo many absorption/emission cycles before destruction. In confocal microscopy, bleaching can occur in the plane-of-focus. However, out-of-focus fluorophores, located above and below the in-focus plane, are also situated in the beam path and receive almost the same amount of irradiance at every depth if the effects of scattering and absorption are negligible (Lichtman and Conchello 2005). Therefore, imaging deep into tissue introduces many unnecessary out-of-focus absorption/emission cycles that can quickly bleach fluorophores and degrade the quality of the in-focus signals, Figure 5(B and D).

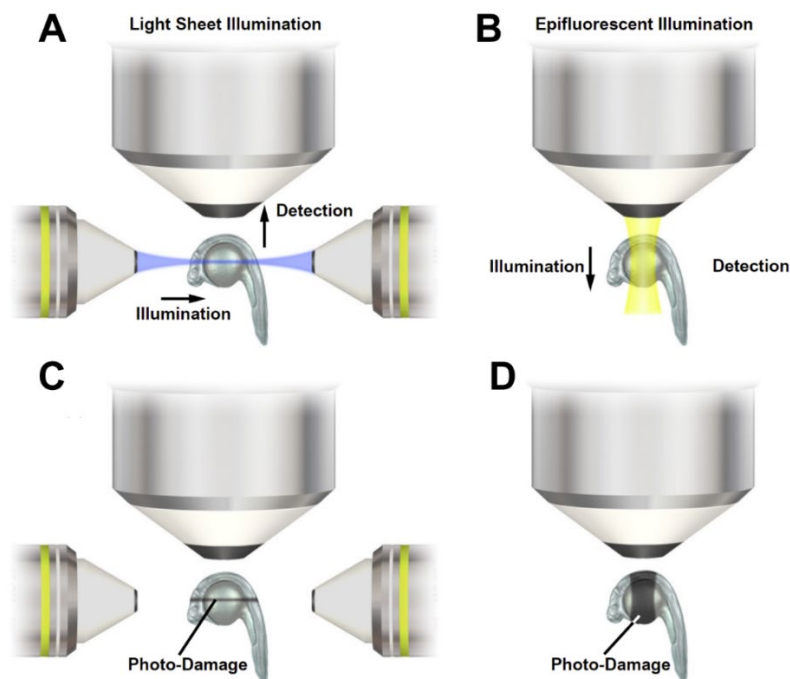


Figure 5 – Affected fluorophore bleaching areas of Confocal and Light Sheet microscopy. (A,C) LSFM results in less out-of-focus fluorophore bleaching when compared to (C,D) confocal microscopy. Adapted from: <https://www.microscopyu.com/techniques/light-sheet/light-sheet-fluorescence-microscopy> (2020)

Recently, these issues have led to a growing trend of wholmount clearing methods being optimized for Light Sheet Fluorescence Microscopy (LSFM) over standard confocal microscopy (Dodt, Leischner et al. 2007, Ertürk, Becker et al. 2012). LSFM is a general term for a growing family of planar illumination techniques which have revolutionized how biological specimens can be optically imaged. Unlike confocal, the illumination and detection

pathways are decoupled. Here, a vertically placed excitation objective(s) forms an extremely thin hyperbolic “sheet” of illumination which covers the entire in-focus plane. An orthogonally placed detection objective, usually located above the sample, then collects the emitted light and transfers it to a high-speed scientific complementary metal-oxide-semiconductor (sCMOS) camera which simultaneously acquires the fluorescence from the entire in-focus plane, Figure 6. Thus, creating extremely fast optical sections (Girkin and Carvalho 2018).

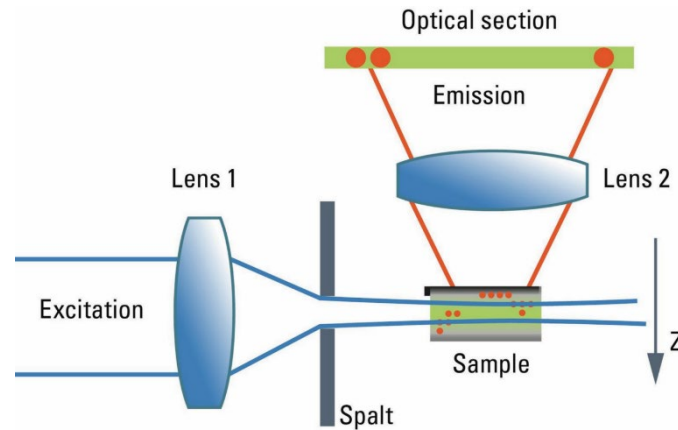


Figure 6 – Traditional light sheet microscope beam path. Adapted from: <https://www.leica-microsystems.com/science-lab/confocal-and-digital-light-sheet-imaging/> (2020)

One highly innovative approach to LSFM was implemented by Leica and was introduced as “digital” light sheet (DLS). Unlike conventional LSFM, which typically requires a dedicated optical setup on an independent system, Leica was able to adapt light sheet imaging as an add-on package for existing inverted TCS SP8 confocal microscopes. Instead of using vertically placed objectives to create the thin “sheet” of illumination, DLS uses an excitation objective located below the sample. This objective takes the typical confocal point illumination and rapidly oscillates the excitation light back and forth, thus creating a pseudo, or “digital”, light sheet. This sheet of light is directed toward mirrors located on both sides of the sample, where it is deflected at a 90° angle into the specimen. This optical plane is collected by a detection objective located above the sample in the manner as previously described, Figure 7. By doing so, Leica’s DLS imaging system is able to acquire up to 70 frames per second (FPS) at 2048 x 2048, which is incredibly impressive considering the 0.4 – 1 FPS at 1024 x 1024 a typical confocal is capable of (Fahrbach and Knebel 2019).

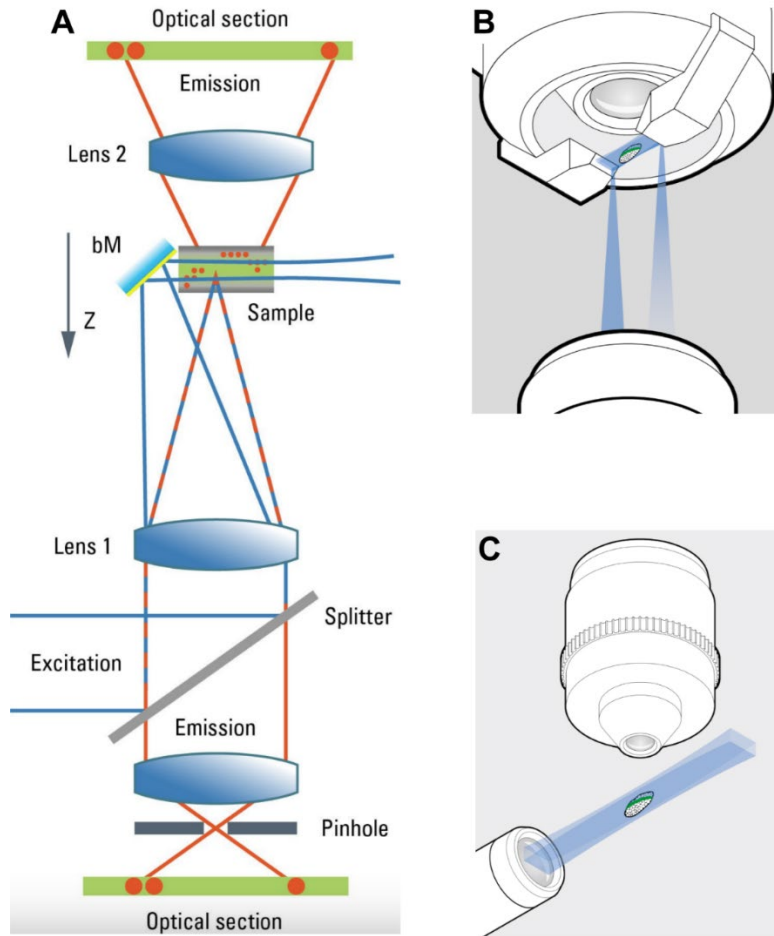


Figure 7 – Leica Microsystem’s Digital Light Sheet. (A) beam path of Leica’s DLS excitation laser, with a visual representation of (B) DLS compared to (C) traditional LSFM. Adapted from: <https://www.leica-microsystems.com/science-lab/confocal-and-digital-light-sheet-imaging/> (2020)

Although LSFM is a magnificent tool for imaging deep into tissue, it does present its own unique set of disadvantages. LSFM is notoriously difficult to implement, usually requiring two or more additional objectives, and involves challenging alignment procedures. Moreover, sample preparation typically uses non-standard protocols and mounting these samples can be extremely tricky. LSFM is also more sensitive to mounting solution “swirling”, caused by refractive index (RI) mismatching throughout the mounting medium which can degrade image quality. The massive amounts of data generated by these techniques must also be dealt with and require exceedingly planned workflows (Girkin and Carvalho 2018). Furthermore, LSFM usually correlates to an increase in background fluorescence when compared to traditional confocal imaging. Thus, attributing to the need of additional post-processing steps involving advanced image deconvolution methods. While Leica’s DLS TwinFlect mirror implementation does alleviate the need for multiple objectives and independent systems, it inadvertently limits the size a sample can be. Given that the widest mirrors Leica offers is 7.8 mm, samples are limited to a size of $\leq \sim 4.5$ mm in Y, whereas the length on the X axis can theoretically be an infinite size. The overall depth across the Z axis is just 1.5 mm and is limited by a combination of the working distance of the objective and the travel distance of the equipped Z-galvo, which is responsible for moving the stage up and down. Unsurprisingly, native tissue typically does not fall into these strict size constraints, thereby creating issues when imaging tissue other than spheroids or organoids (Girkin and Carvalho 2018).

1.1.2 Fluorescence and the behavior of light

In order to fully grasp the concept of confocal microscopy it is important to understand fluorescence and its relationship to confocal microscopy. In 1961, Shimomura and Johnson successfully isolated aequorin along with green fluorescent protein (GFP) from the luminescent jellyfish *Aequorea victoria* for the first time, a moment Shimomura marked as the beginning of GFP research (Shimomura 1995). Soon after, Ridgeway and Ashley exploited the high sensitivity of aequorin to calcium in their publication “Calcium transients in single muscle fibers”. Here, it was found that by injecting this extracted fluorescent protein they could follow the course of the intracellular release and reabsorption of calcium during the contraction of a single muscle fiber of the acorn barnacle, *Balanus nubilus* (Ridgway and Ashley 1967). However, the full potential of GFP was not realized until much later (Prasher, Eckenrode et al. 1992).

Fluorescent proteins, in general, work on the bases that light of a particular wavelength, the excitation wavelength, gets absorbed by the fluorophore and forces it into an excited state. As the fluorophore returns to a ground state, it releases this excess energy in the form of light at a longer, lower energy wavelength, termed the emission wavelength (Lichtman and Conchello 2005). For example, GFP has an excitation peak at 488 nm and emission peak at 509 nm. Since its initial discovery, scientists have found ways to improve the original GFP, create GFP variants with different excitation and emission profiles, and have even extracted new fluorescent proteins from coral. For a visual representation of fluorescent proteins across the spectrum see Figure 8. Thus, enabling researchers to take advantage of fluorophores with different excitation and emission profiles through the use of multiple excitation lasers and fluorescent filters, allowing the labeling and imaging of various structures in a single sample. Furthermore, these fluorophores can be attached to small toxins, antibodies, ligands, and even genetically encoded to study hard to stain structures or cell signaling pathways through techniques such as Förster resonance energy transfer (FRET) (Cranfill, Sell et al. 2016). New cationic near infrared fluorescent dyes have also been created which can be directly perfused into animals to rapidly label blood vessels (Huang, Brenna et al. 2019).

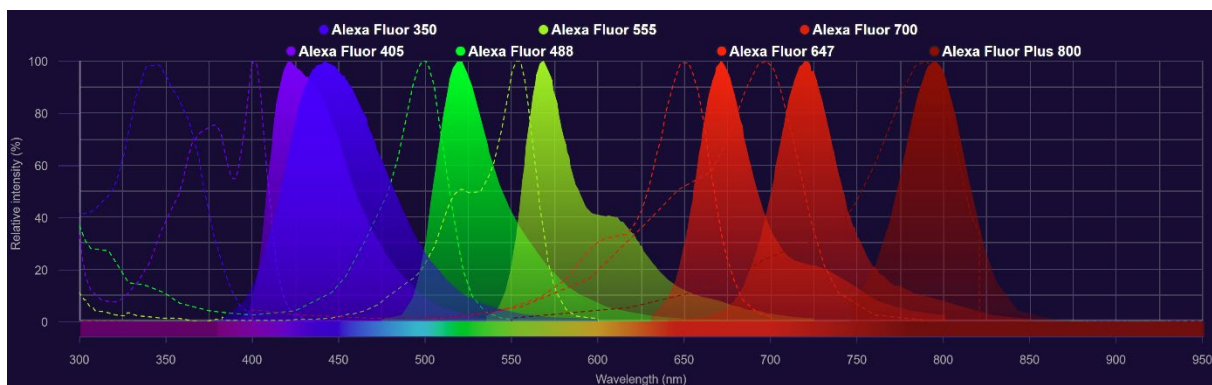


Figure 8 – Representative fluorescent proteins across the spectrum. created using ThermoFisher Scientific’s fluorescence spectraviewer.

However, in order for a microscope to interpret a fluorescent signal, an excitation wavelength must reach the fluorophore and its emission collected back by the objective, both of which can be affected by light scattering. Light waves of a particular wavelength vibrate at a specific frequency and exhibit both electrical and magnetic components, with this electrical component mostly responsible for interacting with atoms in biological tissues. As a plane wave (light that propagates in a single direction, like a microscope’s excitation laser) reaches an atom or molecule it may impart some of its energy to the outer most electrons (Richardson

and Lichtman 2015). This energy causes a short-lived electron vibration where the energy is quickly released in the form of another light wave. Unlike the excitation plane wave, this outgoing light wave is sent in all directions as a spherical wave, thus scattering the light. Since this process happens without any energy loss, the vibrational frequency of the scattered light is unchanged and is therefore considered elastically scattered. However, the interaction between the incoming plane wave and the electron cloud of the scatterer, although brief, does cause a momentary pause in the light's progression. This causes the new scattered wave to be delayed by around one half of a wavelength. This process can happen many times as light passes through a material, with these small delays adding up. As a result, the light's propagation through a material is slowed down, with this reduced velocity being the basis of the refractive index of the medium, Equation 3, Table 1.

$$n = \frac{c}{v}$$

Equation 3 – Calculation for Refractive Index. n = Refractive Index, c = speed of light, v = phase velocity of light

The amount of slowdown per unit volume is directly proportional to the density of molecules, and thus the number of electrons the light wave can interact with. However, density is only one variable which affects the RI, as some materials, such as the hydrophobic molecules in the plasma membrane, have electrons that are more susceptible to absorbing light energy than others. Therefore, even though the density of water surrounding a cell is higher than the density of the fatty cells in the membrane, the membrane ($n = 1.45$) (n = Refractive Index) has a higher index of refraction than water ($n = 1.33$) (Pawley 2006).

List of common refractive indices		
Material	Refractive Index (n)	Conditions
Air	1.000293	0°C and 1 atm
water	1.333	20°C
Ethanol	1.361	20°C
Nucleus	1.36 - 1.37	20°C
Silicone oil	1.393 - 1.403	20°C
Mitochondria	1.40 - 1.42	20°C
Sugar solution (50%)	1.42	20°C
Glycerol (88%)	1.45539	20°C
Fused silica (quartz)	1.458	RT
borosilicate glass (Pyrex)	1.47	RT
Glycerol (100%)	1.4729	20°C
Dimethyl Sulfoxide	1.479	20°C
Benzene	1.501	20°C
Schott D 263® (cover slip glass)	1.51	RT
Microscope immersion oil	1.515	20°C
Lysosome	1.6	20°C

Table 1 – Commonly encountered refractive indexes in microscopy. Information compiled from: Hecht (2002) and Pawley (2006)

Although it is commonly explained that scattering only occurs due to mismatches of the RI at the interfaces between different substances in a tissue, scattering actually happens everywhere there are molecules and not just at these RI mismatch sites. Moreover, the emitted spherical wave, just like the incoming plane wave, can and will interact with electrons in other atoms or molecules repeatedly and propagate spherical waves at many different sites. If two of these waves reach the same place half a wavelength out of phase, i.e. one wave is in the crest and the other is in the trough at the same place, the sum of their amplitudes is zero and no light from

those wavelets appear at that site, Figure 9. This is known as destructive interference and explains why homogenous materials, such as air, water, and glass, appear clear even though the molecules in these materials are scattering light. For example, when a plane wave of light passes through such materials, all the molecules in a plane are set into vibration simultaneously which gives rise to many densely packed spherical waves. Such a high density of scatterers results in a situation where for every cresting wave, there is another wave at its trough at the same place. Consequentially, nearly complete destructive interference prevents hardly any light to propagate perpendicular to the direction of the incoming plane wave. However, in the forward direction, the molecules in front of the plane are activated later when the primary wave reaches them. This causes the crest of the scattered light wave from the earlier illuminated molecules to crest at the same point as the scattered light waves from molecules at more forward sites. Therefore, they are said to be in phase and their amplitudes are added together resulting in constructive interference and light propagation (Richardson and Lichtman 2015).

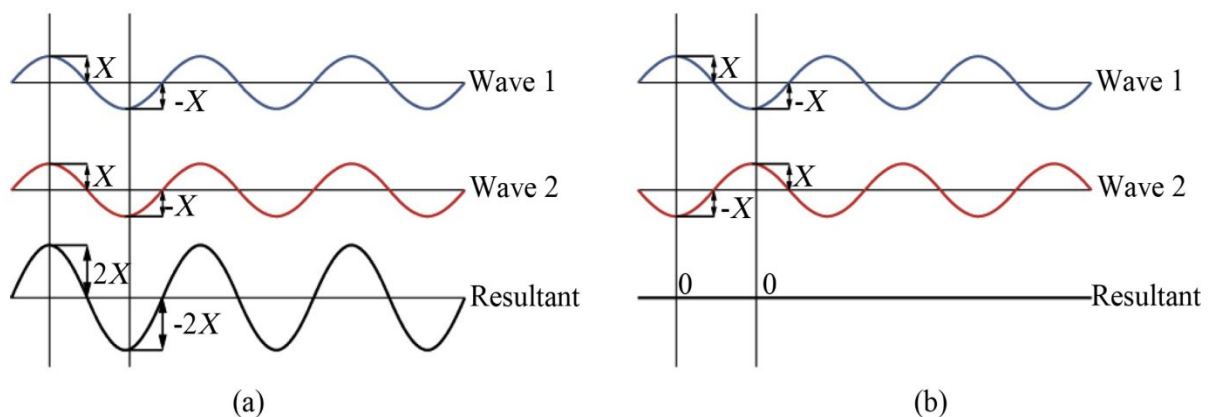


Figure 9 – Constructive and destructive interference. Visual representation of (a) constructive and (b) destructive interference. Adapted from: Geesink and Meijer (2018) (free use under creative commons (CC) license)

However, the prevention of lateral scattering requires each scattering molecule to be of an equal distance from other scatterers at every point in the plane. In living tissue, the amount of scattering from physiological saline solutions located near cell membranes will differ from the membrane itself and may not completely destructively interfere. Thus, both materials will generate light scattered perpendicular to the direction of the incoming plane wave. This multiple scattering property is what generates the whitish translucency of tissues and implies that all wavelengths of visible light are scattered due to the intrinsic inhomogeneities of scatterers in the tissue. Thus, “tissue clearing is not aimed at preventing scattering, but rather assuring that there is a high uniform density of scatterers so lateral scattering is minimal and that all wavelengths of light can pass “through” the tissue” (Richardson and Lichtman 2015).

1.2 Tissue clearing

The long-appreciated technique of tissue slicing, which involves cutting whole tissue into thin slices, has been heavily utilized over the past century to provide microscopic information about cellular constituents within two-dimensional (2D) sections of biological tissues (Silvestri, Costantini et al. 2016). However, there has been a growing trend over the past decade to inquire about the inherently 3D structure of cells and organs. The most obvious example for the need of 3D analysis is the nervous system, given that most individual neurons extend in many directions, thus making their true nature unattainable by 2D analysis. Moreover, developmental biology requires the understanding of morphogenesis of organs and even whole animals in a 3D context (Richardson and Lichtman 2015).

One utilized approach to reconstruct 3D information consists of acquiring images from a sequence of serial thin sections and then merging these images together. However, this tactic is technically challenging for most researchers due to loss or distortion of individual sections that become torn, folded, compressed, or stretched during the slicing process. This inevitably leads to a loss of information in the inadequate final volumetric reconstruction (Richardson and Lichtman 2015, Lee, Choi et al. 2016). Another possible technique is to image the surface of a block of tissue and then sequentially shave off the surface, image that surface, and continue this process until the whole block is imaged. Indeed, these “blockface” methods have been successfully used in both light (Toga, Ambach et al. 1994, Tsai, Blinder et al. 2009) and electron (Denk and Horstmann 2004, Ichimura, Miyazaki et al. 2015) microscopy. This approach does eliminate the loss and reconstruction alignment issues which plague serial slicing but are destructive in the sense that once each section is imaged, it is destroyed to reveal the next surface. Moreover, this method requires special state-of-the-art equipment in order to perform, thus limiting its implementation to only highly funded and well-equipped laboratories (Matryba, Kaczmarek et al. 2019). One more possible route to obtain 3D information from biological samples is to image the whole volume without physically slicing, but rather utilize “optical sectioning” techniques. These non-sectioning approaches circumvent the issues previously mentioned for serial sectioning methods, with an additional advantage of allowing samples to, in principle, be imaged multiple times, in contrast to blockface methods (Silvestri, Costantini et al. 2016).

However, acquiring data based on whole mount imaging can be difficult since imaging depths in native tissue can only achieve shallow depths of $\sim 50 - \sim 150 \mu\text{m}$ into the tissue, depending on what type of tissue is being investigated (Silvestri, Costantini et al. 2016). This lack of imaging depth is caused by three major factors. First, some tissues contain pigments which gives the tissue a color. This, in turn, has the consequence of absorbing the light within a sample and can limit both the excitation light entering the tissue as well as the fluorescence emission returning to the detector. The primary molecules responsible for this in biological tissue are hemoglobin, myoglobin, and melanin. Secondly, inherently fluorescent molecules are typically present in tissue and can mask fluorescently labelled structures of interest. This phenomenon is known as autofluorescence, or the background “glow” of a sample resulting from excitation of the aforementioned inherently fluorescent molecules within tissue. Nicotinamide adenine dinucleotide phosphate (NADPH), collagen, flavins, tyrosine, as well as other biomolecules can also be responsible for this. Further compounding this issue, autofluorescence is also introduced by the formation of Schiff’s bases during fixation with aldehydes (Conchello and Lichtman 2005, Richardson and Lichtman 2015). In addition, it is well documented different commonly used fixation methods can induce varying degrees of autofluorescence, with glutaraldehyde introducing a much higher background autofluorescence than paraformaldehyde (Collins and Goldsmith 1981). The final issue afflicting whole mount imaging is the fact most biological tissues have an aforementioned, intrinsic milky appearance, which gives tissues the property of frosted glass or translucence. This lack of clarity induces blurriness in acquired images and becomes progressively worse the deeper one tries to image. This milky appearance is caused by light scattering. This happens when light rays, which should travel in straight lines, are deviated many times as it is reflected off molecules, membranes, organelles, and cells within the tissue. Although this scattering of light is commonly attributed to the mismatch of the index of refractions at the interfaces between different compartments in a tissue, a more precise description, given by Richardson and Lichtman (2015), is that the heterogeneity in the amount of scattering between different regions in biological samples is what actually gives rise to the scattering and milky appearance, as previously discussed.

A plethora of tissue optical clearing (TOC) methods have been developed in the attempt to circumvent these limitations and include bleaching and chemical treatments to remove tissue pigmentation and decrease autofluorescence as well as using high refractive index solutions and lipid removal to homogenize tissue. This assures a highly uniform density of scattered light so lateral scattering is minimal and all wavelengths of light pass through the tissue (Clancy and Cauller 1998, Duong and Han 2013, Matryba, Kaczmarek et al. 2019). First classified by Richardson and Lichtman (2015) and later extended to include 21 protocols by Silvestri et al. (2016) in their “classical taxonomy of tissue clearing”, TOC methods are usually categorized on the bases of which chemicals are used and consist of four main groups: organic solvent-based, high-refractive index aqueous solutions, hyperhydrating solutions, and tissue transformation. Moreover, the field of tissue clearing has gained considerable traction in recent years. This was highlighted in 2019 when Matryba et al. published a proposed newly revised version of Silvestri’s classical taxonomy, adding an impressive 19 new methods in just three short years, shown in Figure 10. However, it is important to note that these representations only include the most well-known clearing methods and exclude many others that were also developed during this time (Shah, Kulkarni et al. 2017, Williams, Rigon et al. 2019, Tu, Xu et al. 2020). Yet, even with so many newly developed methods, the four primary categories have not changed, owing to the fact many “new” protocols just consist of modifications to previously established ones. Unsurprisingly, this is done to either address some of the drawbacks of a particular method, thus creating a more universally applicable method, or to optimize a method for a specific use case. Therefore, the following sections will review the evolution of each category, with a focus on skeletal muscle clearing.

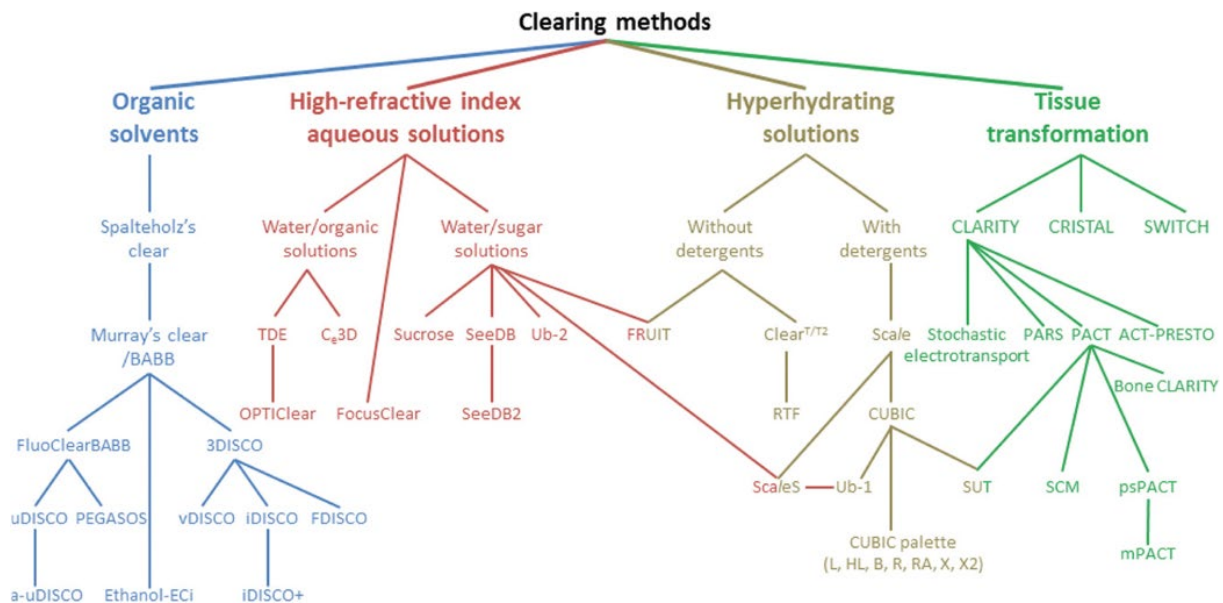


Figure 10 - Updated classical taxonomy of tissue clearing methods. Adapted from: Matryba, Kaczmarek et al. (2019) (free to use under CC license)

1.2.1 Organic solvents

Solvent based tissue clearing is commonly a two-step procedure which relies on the process of sample dehydration in an alcohol gradient, followed by sample incubation in a high Refractive Index (RI) matching solution. This general strategy was first introduced in 1914 by the German anatomist Werner Spalteholz and has endured for more than a century with only slight, but essential modifications (Spalteholz 1914, Matryba, Kaczmarek et al. 2019). In his study, he found that muscle tissue becomes most transparent when placed in a medium where the tissue sample’s RI matches that of the medium. This RI matching enables light to more readily pass

through the surface of tissue due to a decrease in the heterogeneity of light scattering and, thus, leaves tissue “optically cleared”. Based on this principle, Spalteholz created a method, termed Spalteholz’s clear, to substitute water with a mixture of benzyl benzoate, methyl salicylate, and wintergreen oil which resulted in a rather high RI of about 1.55, roughly matching that of dry tissue ($n_{\text{dry}} = 1.50$). Additionally, to decrease light absorption, a bleaching step utilizing hydrogen peroxide to remove tissue pigmentation was introduced (Spalteholz 1914). Andrew Murry further improved the RI matching solution and created a mixture consisting of a 1:2 ratio of benzyl alcohol:benzyl benzoate, now known as BABB or Murray’s Clear ($n = 1.55$) (Ariel 2017). However, due to the insoluble property of benzyl benzoate in water, a tissue dehydration step using ethanol, in lieu of methanol, was added to the protocol and was reintroduced by Dodt et al. (2007). Though, this protocol was found to quickly quench fluorescence and was not applicable for adult organs containing high amounts of lipids. Therefore, the same group decided to investigate different dehydration and optical clearing agents and used dichloromethane (DCM), as a delipidating agent, and tetrahydrofuran (THF) for delipidation and dehydration. However, this method still exhibited suboptimal imaging results as before, which led Becker et al. (2012) to perform a follow up study by screening several solvents and introduced a superior protocol in which BABB was replaced with dibenzyl ether (DBE, $n = 1.56$).

Even with the many advancements and modifications to the original BABB protocol up to this point, rapid fluorophore quenching still plagued solvent-based clearing methods. Moreover, due to a rise in the implementation of novel microscopy techniques, such as light sheet fluorescence microscopy (LSFM), as well as advancements in computer hardware, imaging data for whole organs could now be acquired in a matter of hours rather than days. Predictably, these advancements led to a substantial increase in the typical size of microscopy datasets. Expanding acquired datasets from ~10 gigabytes (GB) to well over 500 GB or even 1 terabyte (TB) in size. Thus, introducing a new problem of how to properly store, manage, and analyze big data. Both limitations were partially addressed by Ertürk et al. (2012) with the introduction of 3D imaging of solvent-cleared organs (3DISCO). Built upon previously published chemical combinations, 3DISCO replaces the methanol dehydration step with incubation in THF and is an optimized solvent-based method for LSFM which preserved fluorescence longer than previous methods, albeit only for ~24 hours. More notably, the authors also included a heavily detailed pipeline for not only sample preparation, but also data acquisition, storage, and analysis (Ertürk, Becker et al. 2012). This approach made for a highly alluring and reproducible protocol which set into motion a surge of new advancements for solvent-based clearing techniques based on 3DISCO, including FluoClearBABB, immunolabeling-enabled 3DISCO (iDISCO), iDISCO+, ultimate DISCO (uDISCO), nanobodies(V_{HH})-boosted DISCO (vDISCO), and DISCO with superior fluorescence-preserving capability (FDISCO) (Molbay, Kolabas et al. 2021). Although each of these iterations improved and addressed various aspects of solvent-based clearing, only FDISCO, a modified iDISCO, and 3DISCO have been used for clearing skeletal muscle to date. However, the application of the modified iDISCO protocol from Khan et al. (2016) was not characterized and would need further evaluation. Yin et al. (2019) demonstrated the ability of 3DISCO by applying it to impressively clear mouse gastrocnemius muscles, as shown in Figure 11.

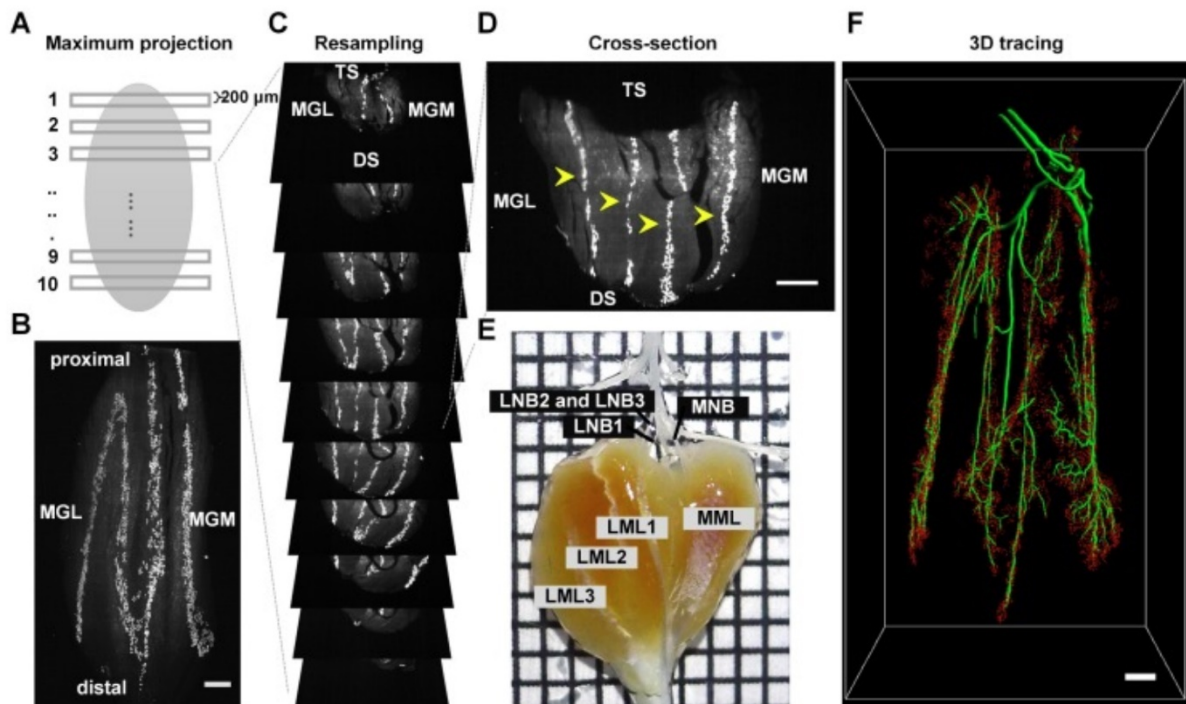


Figure 11 - Distribution of NMJs and the innervation pattern of the gastrocnemius. Source: (Yin, Yu et al. 2019) (free to use under CC license)

Here, they were able to visualize the distribution of Neuromuscular Junctions (NMJ) throughout the entire muscle, as well as characterize the degradation pattern of NMJs before and after a denervated state over a 6-month period. They were also able to show the loss of muscle volume during this same time frame. Though, the authors did point out that FDISCO was used in lieu of 3DISCO for mice containing transgenically expressed fluorescent proteins in order to preserve their fluorescence. FDISCO is one of the more unique methods as the authors decided to focus on the influences of temperature and pH, rather than switching to different solvents. In doing so, they found fluorescent markers could be preserved up to 28 days by preparing samples at 4°C using a pH adjusted THF (pH = 9.0) and DBE (Qi, Yu et al. 2019). Unfortunately, this is the only published example utilizing solvent-based clearing methods for whole mount skeletal muscle.

While Yin et al. (2019) expertly demonstrates the major advantages of using solvent-based clearing methods, they also inadvertently highlight many of its pitfalls. The toxicity of the chemicals used in such protocols is a key concern, not only for humans but also delicate microscopy equipment. To put these highly corrosive solutions in perspective, xylene, a commonly used chemical in solvent-based clearing, is added to many paint thinners and adhesive removers due to its excellent solubilizing properties (Shah, Kulkarni et al. 2017). Thus, expensive special objectives, microscopy systems, or non-immersion lenses must be used as the chemicals can degrade the glue holding the lenses in place. Moreover, an accidental spill of mounting media, a fairly common occurrence, could prove disastrous compared to other mounting mediums frequently used. Undeniably, this was the rationale as to why Yin et al. utilized LaVision BioTec's UltraMicroscope I, as it was specifically made for handling solvent-based tissue clearing methods. However, many researchers do not have access to such equipment and would be extremely costly to implement. While toxicity has been addressed in newer methods, such as replacing DBE with non-toxic ethyl cinnamate (ECi) in ECi methods (Huang, Brenna et al. 2019) or even using kerosene as a replacement for xylene (Shah, Kulkarni et al. 2017), these alternatives are rarely used. This is presumably due to their lower clearing

capacities as well as being less documented in literature when compared to more traditional methods such as 3DISCO. Interestingly, once interpreted as a major disadvantage, the unavoidable shrinkage of tissue observed when using solvent-based methods is now considered an advantage. Proponents of these methods praise this feature as shrinkage does decrease the time needed for imaging and, naturally, leads to much smaller datasets. Thus, making data acquisition and analysis faster and easier. However, this effect can be detrimental when investigating very small structures or in colocalization studies where the resolving power of an objective may already be at its limit. Lastly, all solvent-based methods prevent the analysis of lipids and cannot be used for such studies (Silvestri, Costantini et al. 2016, Matryba, Kaczmarek et al. 2019).

1.2.2 High refractive index aqueous solutions

Driven by the inability of solvent-based methods to preserve fluorescent protein emission and to prevent changes in tissue architecture, many researchers have decided to pursue aqueous based clearing solutions (Richardson and Lichtman 2015). The overall concept of this set of clearing methods consists of a simple passive immersion in an aqueous-based solution which is RI matched to the average RI of tissue (greater than $n = 1.45$). Thus, removing the harsh dehydration steps which are responsible for creating environments not always suitable for proteins and laid the foundation for creating faster, more applicable, and versatile methods (Silvestri, Costantini et al. 2016). Indeed, Aoyagi et al. (2015) found that a simple soak in 2,2'-thiodiethanol (TDE, $n = 1.42$) for as short as 30 minutes was able to increase transparency and penetration depth in both confocal and two-photon microscopy for 400 μm thick brain slices. Other methods found in this group, seeDB, SeeDB2, and FRUIT ($n = 1.48$), utilize sugar solutions, with various additives, to increase the RI of the medium to match that of the tissue, which also yielded optically clear tissue (Ke, Fujimoto et al. 2013, Hou, Zhang et al. 2015, Ke, Nakai et al. 2016). However, highly concentrated sugar or glycerol solutions can be difficult to work with due to their high viscosity. This can lead to RI mismatches caused by trapped air bubbles, precipitation at room temperature, and/or poor homogenization within tissue (Richardson and Lichtman 2015). Introduced as a less viscous alternative, FocusClear ($n = 1.45$) is a commercially available optical clearing agent whose composition, according to the patent, consists of dimethyl sulfoxide (DMSO), diatrizoate acid, ethylenediaminetetraacetic acid, glucamine, β -nicotinamide adenine dinucleotide phosphate, sodium diatrizoate, and derivatives of polyoxyalkalene (Matryba, Kaczmarek et al. 2019). However, it is important to note FocusClear was introduced to use alongside the tissue transformation X-CLARITY clearing protocol (Lee, Choi et al. 2016), thus, bringing into question the overall effectiveness of using aqueous-based optical clearing techniques as a standalone solution for tissues other than brain. Indeed, it was found these methods, while useful, lack the accountability of other important aspects to obtaining crisp images and is reinforced by the absence of adult skeletal muscle tissue clearing publications using only high refractive index matching solutions. This can be attributed to the fact that skeletal muscle alone presents a high RI mismatch between muscle fluids ($n = 1.35$, 72 – 80% of muscle weight) and muscle proteins ($n = 1.53$, 20 – 28% of muscle weight), which immersion-based methods cannot compensate for alone (Matryba, Kaczmarek et al. 2019). Furthermore, it is generally recommended to pair these methods with other clearing protocols in order to unlock their full potential and versatility.

1.2.3 Hyperhydrating solutions

Hama et al. (2011) is accredited for pioneering the field of tissue hyperhydration after observing 4 M urea has the ability to make polyvinylidene fluoride membranes transparent. This initial finding led the group to the introduction of the tissue clearing method Scale, which is of

particular interest since it not only takes advantage of high RI solutions, such as glycerol (>99.5% glycerol, $n = 1.47$), but also attempts to address other important aspects, such as decreasing RI mismatch through delipidation (Susaki, Tainaka et al. 2015). Lipids are one of the main obstacles in deep tissue imaging since its presence causes light scattering, limits the depth of light penetration, and constitutes an antibody-impermeable barrier (Magliaro, Callara et al. 2016). However, Scale was able to remove lipids by using a solution of glycerol and Triton-X, in lieu of solvents. At the same time urea was used to penetrate, partially denature, and hydrate even the most hydrophobic regions of high RI proteins (Hama, Kurokawa et al. 2011). While the atomic-level explanation is not well understood, this hyperhydration reduces the overall RI of tissue to ~ 1.38 . Although this could be caused by the spreading apart of dense, high RI scattering sites within protein complexes, with this explanation supported by the observation that samples processed with Scale tend to have an expanded volume (Richardson and Lichtman 2015). Since this initial protocol, many polyalcohols, detergents, hydrophilic compounds, and other chemical agents have been tested for their effectiveness in tissue clearing (Tainaka, Kubota et al. 2014). CUBIC ($n = 1.48$) was one method created from this in depth screening, which found that the aminoalcohol N,N,N',N'-Tetrakis(2-hydroxypropyl)ethylenediamine (Quadrol) has the ability to decolorize tissue samples by the removal of hemoglobin, or myoglobin in the case of muscle, and, in turn, is able to reduce the overall autofluorescence of tissue (Susaki, Tainaka et al. 2015). As promising as these methods seem, concerns of fluorescence quenching, protein loss, and tissue bloating have been raised (Richardson and Lichtman 2015). There is a delicate balance of chemical combinations and the percentages used in creating these solutions to avoid such problems. However, more research is needed in this area in order to create a more robust protocol (Azaripour, Lagerweij et al. 2016). Moreover, to our knowledge, there has not been a method from this group that has been published specifically for clearing adult skeletal muscle, with the exception of Decroix et al. (2015) who compared the clearing efficacy of Clear(T2), ScaleA2, and 3DISCO. Although, they suggest 3DISCO for its shorter clearing time and ability to preserve both endogenous green fluorescent protein (GFP) and immunohistochemical stainings.

1.2.4 Tissue transformation

Chung et al. (2013) revolutionized tissue clearing by creating the first tissue transformation protocol termed “Clear Lipid-exchanged Acrylamide-hybridized Rigid imaging, Immunostaining, in-situ-hybridization-compatible Tissue hYdrogel” (CLARITY) ($n = 1.45$). Here, instead of taking anywhere from 5 - 120 days to delipidate tissue samples, as previously reported in other aqueous based protocols such as Scale (Hama, Kurokawa et al. 2011), they were able to accomplish this in just 1-2 days (Chung, Wallace et al. 2013). Moreover, hyperhydration methods also tend to use very high triton levels to maximize lipid removal which inevitably results in a high degree of protein loss from 24 – 41%. CLARITY, on the other hand, is able to circumvent these shortcomings by embedding paraformaldehyde (PFA) fixed tissue with a acrylamide/bis-acrylamide hydrogel which helps crosslink and fix proteins in place, adding tissue stability and porosity (Chung and Deisseroth 2013). Thus, decreasing protein loss during clearing and accelerating staining penetration and depth. This hydrogel was also able to aid in imaging depth by uniformly stabilizing the RI across tissue from the estimated $n = 1.50$ of dry tissue to $n = 1.457$ (Lee, Choi et al. 2016, Silvestri, Costantini et al. 2016). Embedded samples were then delipidated using a custom, in house, electrophoresis chamber (ETC). Here, a current is applied over the sample coupled with a continual stream of 8% sodium dodecyl sulfate (SDS), an ionic detergent, flowing over the sample in order to increase lipid mobility. Though, some suggest implementing CLARITY or sClarity into a lab setting to be highly cumbersome due to the need of building such custom equipment (Chung and Deisseroth 2013). Fortunately, many companies have recently introduced equipment available for purchase

such as Logos Biosystem's X-CLARITY tissue clearing system II for CLARITY based protocols and Life Canvas's SmartClear II Pro for sClarity based protocols, making implementation easier, albeit more costly.

Although the original CLARITY method was only designed for brain tissue, ACT-PRESTO, a revised CLARITY protocol, was able to successfully apply it to many other types of tissue (Lee, Choi et al. 2016). While the efficiency and versatility of this method cannot be ignored, aspects of tissue damage and deformation due to high current exposure, incompatibility with certain types of staining, darkening of tissue, and vital protein loss are some concerns that have been raised (Chung, Wallace et al. 2013, Azaripour, Lagerweij et al. 2016, Milgroom and Ralston 2016). However, the stochastic electrotransport (sClarity $n = 1.45$) method was able to decrease many of these negative side effects, implement faster immunostaining, and still quickly clear tissue by circularly rotating the sample and applying only 250-380 milliamps (mA) of current compared to 1.5 amps (A) used in the original method (Kim, Cho et al. 2015). Another interesting twist to the protocol was introduced by Xu et al. (2017) and termed Fast free-of-acrylamide clearing tissue (FACT). The authors found that brain samples could be passively cleared using 8% sodium dodecyl sulfate (SDS) and resulted in relatively high protein conservation and comparable imaging depths to the original protocol, without the need of acrylamide embedding. Although promising, Williams et al. (2019) found that more heterogeneous tissue, such as skeletal muscle, needed acrylamide embedding to homogenize the RI throughout the tissue to enable deep imaging. Another issue concerning clearing skeletal muscle was initially discovered by Milgroom and Ralston (2016) who found that CLARITY based methods were incompatible with α -bungarotoxin (α -BGT), the most widely used postsynaptic NMJ marker which labels nicotinic acetylcholine receptors (AChRs) with unmatched specificity. While alternative and CLARITY compatible antibody stainings do exist, they are rarely used for this purpose due to their poor performance and un-specificity, thus emphasizing the need for compatible methods (Garg and Loring 2017). Milgroom and Ralston (2016) hypothesized α -BGT was unsuitable due to hydrogel cross-linking and fixation preventing access of the toxin to the AChRs, with this incompatibility further corroborated by Zhang et al. (2018). Yet, Williams et al. (2019) discovered this hypothesis to be incorrect and demonstrates that SDS is actually the cause as it irreversibly denatures AChRs to the point α -BGT can no longer bind. Though protein denaturation can be detrimental for stainings that rely on a specific protein conformation in order to bind, such as α -BGT, this process can result in a higher quality antibody staining since attachment sites become more accessible and is most likely a large contributing factor to the vast compatibility of antibody stainings CLARITY based protocols enjoy (Lee, Choi et al. 2016).

1.3 Sepsis

Sepsis is a common life-threatening disease with a relatively high mortality rate ranging from 28% - 80%, for a systemic inflammatory response (SIRS) and septic shock states, respectively, Figure 12. In 2017 sepsis affected an estimated 48.9 million people worldwide, with 11 million sepsis related deaths reported, representing 19.7% of all global deaths (Rudd, Johnson et al. 2020). Though, it is generally assumed the number of affected people and deaths are far higher due to most available data coming from only high-income areas, such as the United States, Germany, Australia, Taiwan, Norway, Spain, and Sweden. Thus, neglecting data from low- and middle-income areas representing 80% of the global population (Bloos 2018). Sepsis is also considered a massive burden on healthcare systems with sepsis related health care costs rising from an estimated 27.7 billion to 41.5 billion US-Dollars from 2012 to 2018 in the U.S.A. alone (Buchman, Simpson et al. 2020). As for Germany, sepsis ranked third among the most frequent

cause of death in 2013, with a 9.1 billion Euro healthcare cost burden which is projected to be higher today (Fleischmann, Hartmann et al. 2015). However, for most clinicians and scientists, sepsis has remained a long-unsolved medical mystery. Some of this is due in part to sepsis, as a clinical entity, being a very heterogeneous disease, with clinical data invariably confounded by the effects of age, coexisting diseases, and supportive therapy (Fink and Heard 1990).

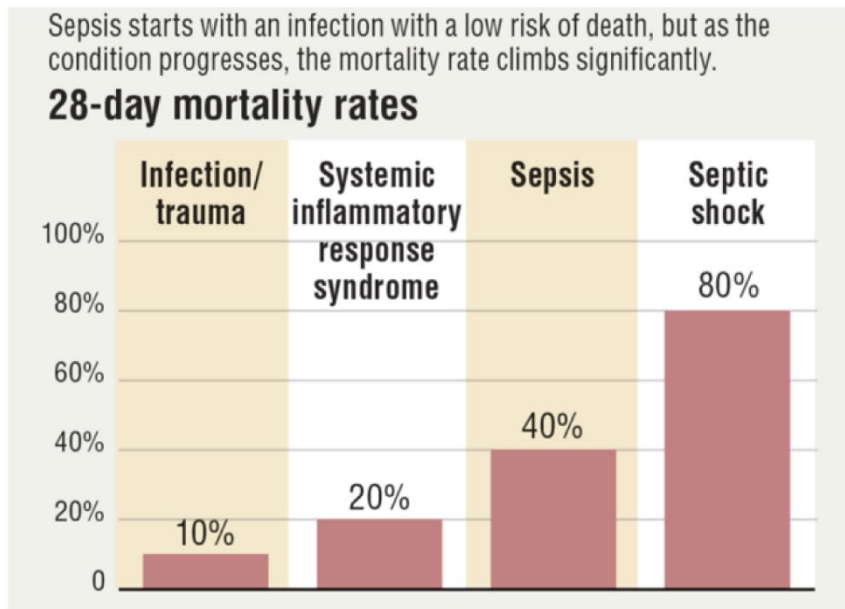


Figure 12 - Sepsis mortality rates in relation to disease severity. Adapted from: www.sepsis.com (2017)

Sepsis, in a simplistic view, can be defined by a complex dysregulation of inflammation arising when the host is unable to successfully contain an infection usually caused by bacteria but may be fungal or viral as well. This poorly understood dysregulation ultimately affects multiple organs through influences on endothelial, epithelial, and immune cell types, leading to irreversible tissue damage via self-inflicted injury induced by the immune system (Buras, Holzmann et al. 2005, Munford 2006, Suffredini and Noveck 2014). Moreover, the definition of sepsis has always been based on clinical features (Gyawali, Ramakrishna et al. 2019), therefore, typical signs and symptoms of sepsis are summarized in Table 2.

	Clinical signs and symptoms
Temperature	> 38°C or < 36°C
Inflammatory	High white blood cell count
	Immature white blood cells in circulation
	Elevated plasma C-reactive protein
	Elevated procalcitonin
Hemodynamic	Low blood pressure
	Low central venous or mixed venous oxygen saturation
	High cardiac index
Organ dysfunction	Low oxygen level
	Low urine output
	High creatinine in the blood
	Coagulation (clotting) abnormalities
	Absent bowel sounds
	Low platelets in the blood
	High bilirubin levels
Tissue perfusion	High lactate in the blood
	Decreased capillary filling or mottling
Mental decline	Confused
	Sleepy
	Difficult to rouse
Infection	Generalized infection
	circulating bacteria in blood

Table 2 – Typical signs and symptoms of sepsis. Information compiled from: Drewry and Hotchkiss (2015)

What we do know is two distinct, although not mutually exclusive, phases can be involved in the sepsis inflammatory response: The Systemic Inflammatory Response (SIRS) and the Compensatory Anti-inflammatory Response (CARS). In a normal response, SIRS acts as a functionally effective inflammatory response to infection or injury, which then can be deactivated through the expression of, anti-inflammatory, CARS mediators, as shown in Figure 13. However, in sepsis, one or, in the usual case, both of these responses become dysregulated and exhibit an exaggerated response (Buras, Holzmann et al. 2005).

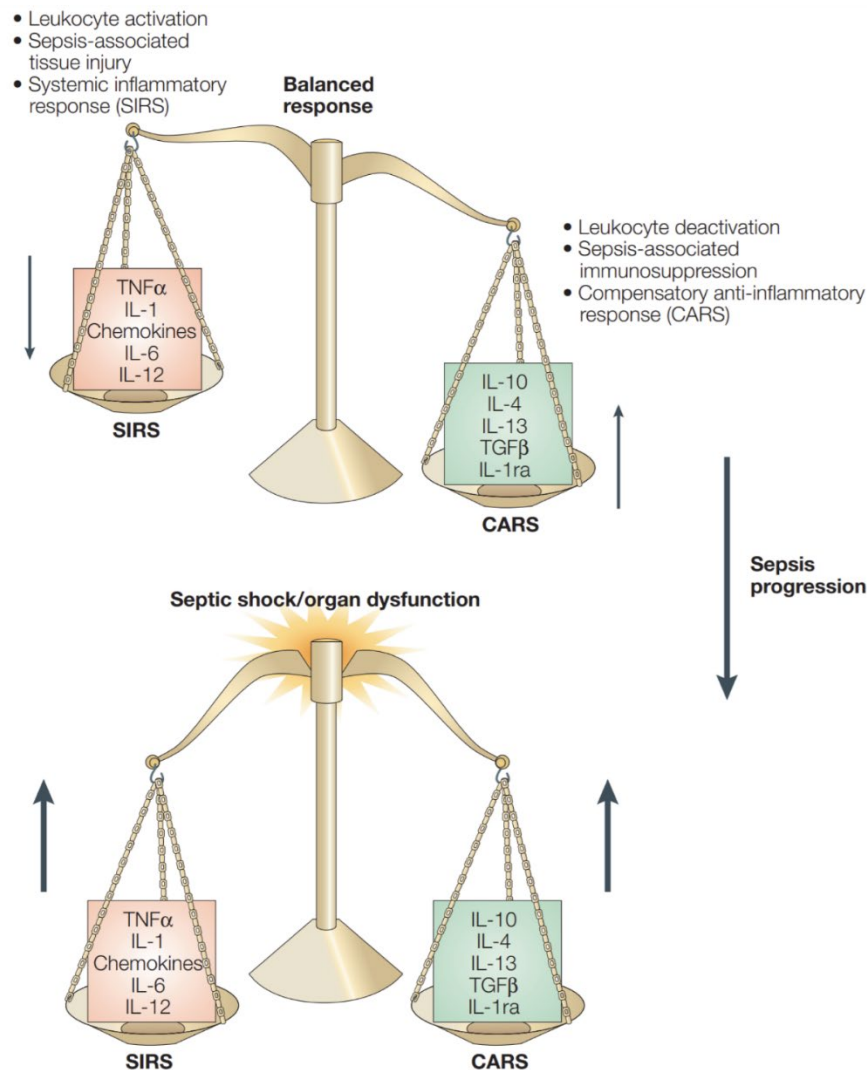


Figure 13 - Inflammatory and anti-inflammatory cytokines response in sepsis. Adapted from: Buras, Holzmann et al. (2005) (Rights obtained for use)

In humans, the guidelines for diagnosing sepsis as well as the subsequent recommended treatment regimen is an ever-evolving process, Table 3. This is in part due to the fact that identification of patients with acute organ dysfunction in need of antibiotic therapy is not always obvious, as well as the need for early diagnosis, so therapeutics can be administered promptly in life-threatening circumstances. Further compounding the issue and unlike many other diseases, there are no biomarkers currently available which allow for a rapid and reliable discrimination between sepsis and non-infectious inflammatory states (Bloos 2018). However, procalcitonin (PCT) is seen as the best investigated biomarker to differentiate between these two states with fairly good accuracy. Still, PCT does seem to be unreliable if viruses or fungi are the underlying cause (Rhodes, Evans et al. 2017).

In an attempt to bridge this gap, the first definition of sepsis was published in 1992 by expert opinion only and introduced the term systemic inflammatory response syndrome (SIRS), which was supposed to describe the inflammatory response not only seen in sepsis but in many other non-infectious diseases as well (Bone, Sibbald et al. 1992). In 2001 a second attempt to categorize sepsis, sepsis-2, was published which was also based on expert opinion and relied on the concept of SIRS (Levy, Fink et al. 2003). However, SIRS was unsurprisingly abandoned in 2015 by the third definition of sepsis (sepsis-3) after criticism of being too unspecific for any beneficial diagnostic value (Bloos 2018). Yet, sepsis-2 did introduce the idea of sequential

organ failure assessment (SOFA) as a potential definition of infection associated organ dysfunction, but the authors failed to give further advise for the application of such a scoring system (Levy, Fink et al. 2003). To overcome the shortcomings of relying on expert opinion alone, the sepsis-3 taskforce applied scientific methods to develop new sepsis definitions. The SOFA scoring system was implemented and based on six different scores, one each for the respiratory, cardiovascular, hepatic, coagulation, renal, and neurological systems (Kell and Pretorius 2017). Next, diagnostic criteria for sepsis were derived from a database consisting of 148,907 patients with suspected infection, where they found SOFA had a higher sepsis predictive validity than SIRS. However, determining the SOFA-score is time consuming and requires laboratory assessments. Therefore, the authors also introduced a quick SOFA score (qSOFA) as a screening tool for a rapid method to assess the risk of a patient. qSOFA is based on three items: altered mental status, tachypnea ≥ 22 breaths/min, and arterial hypotension (systolic blood pressure ≤ 100 mmHg). It is important to note that qSOFA has a lower predictive validity than SOFA, and thus, does not replace SIRS or SOFA, and ultimately cannot diagnose sepsis (Bloos 2018).

Term	Sepsis-1	Sepsis-2	Sepsis-3
SIRS	At least two of the following conditions: (I) temperature >38 °C or <36 °C; (II) heart rate >90 /min; (III) respiratory rate >20 /min or PaCO ₂ <32 mmHg; (IV) WBC $>12,000$ or $<4,000$ or $>10\%$ immature (band) forms	As Sepsis-1, future SIRS diagnosis by biochemical features suggested	Abandoned
Sepsis	SIRS induced by infection	Presence of both infection and systemic inflammatory response (6 main diagnostic criteria)	Acute change in total SOFA score of at least 2 points associated with infection
Severe sepsis	Sepsis associated with organ, hypo perfusion, or hypotension	Use Multiple organ dysfunction score or SOFA-score	Abandoned
Septic shock	Sepsis induced arterial hypotension (systolic arterial pressure <90 mmHg or reduction in systolic blood pressure of ≥ 40 mm Hg from baseline) despite adequate fluid resuscitation and presence of perfusion abnormalities	Systolic arterial pressure <90 mmHg, an MAP <60 , or a reduction in systolic blood pressure of 40 mmHg from baseline, despite adequate volume resuscitation, in the absence of other causes for hypotension	Sepsis with persisting hypotension requiring vasopressors to maintain MAP ≥ 65 mmHg and having a serum lactate level >2 mmol/L despite adequate volume resuscitation

Table 3 – Evolution of sepsis diagnosis criteria. Sepsis-1, ACCP/SCCM consensus conference 1992; Sepsis-2, SCCM/ESICM/ACCP/ATS/SIS International Sepsis Definitions Conference 2001; Sepsis-3, International Consensus Conference 2015. MAP, mean arterial pressure; SIRS, systemic inflammatory response syndrome; SOFA, sequential organ failure assessment; WBC, white blood cell count. Adapted from: Bloos (2018) (Rights obtained for use)

After diagnosis, early and adequate antimicrobial therapy is the cornerstone for the treatment of sepsis. In general, broad-spectrum carbapenems, such as meropenem, imipenem (IPM)/cilastatin or doripenem, or extended-range penicillin/ β -lactamase inhibitor combination is recommended as first choice drugs (Bloos 2018). However, de-escalation strategies, or switching from broad-spectrum antimicrobials to a narrower spectrum as soon as the microbiological results are available, has been recommended and is associated with a decrease in mortality (Guo, Gao et al. 2016). In addition, PCT levels may aid in the discontinuation of antibiotics after the infection site has been controlled. Resuscitation, consisting of fluids and vasopressor therapy, is also crucial as hemodynamic deterioration occurs frequently in sepsis. This is emphasized in patients suffering from septic shock as it is usually accompanied by severe hypovolemia. The surviving sepsis campaign (SSC) recommends the use of balanced crystalloid solutions or saline for fluid resuscitation. Moreover, the hemodynamic status of a patient must be evaluated regularly, and fluid administration should be continued as long as hemodynamic parameters continue to improve. However, caution must be taken since a high cumulative fluid balance is associated with increased risk of death. While central venous pressure (CVP) has been used to guide fluid resuscitation in the past, it has been found to not

adequately predict fluid response. Instead, physicians are now recommended to use dynamic measures including passive leg raising, fluid challenge, and pulse pressure/stroke volume variation in mechanically ventilated patients to help guide fluid therapies. Arterial hypotension is another factor that frequently accompanies sepsis and regularly persists during or after fluid resuscitation. Thus, it is recommended to administer norepinephrine as the first choice vasopressor to achieve a target mean arterial blood pressure of at least 65 mmHg (Bloos 2018).

1.3.1 Animal models of sepsis

Unfortunately, due to the complex and heterogeneous nature of sepsis, there are no perfect murine models of the disease. Yet, a sundry of good options for modeling sepsis exists depending on the focus of the research. To date, the list of available septic models includes but is not limited to: Endotoxemia, bacterial injection, bacteria and fibrin clot implantation, cecal/fecal slurry injection, Cecal Ligation and Puncture (CLP), Colon Ascendens Stent Peritonitis (CASP), pneumonia, and urosepsis. However, they all display similar shortcomings in the way of reproducibility and their ability to mimic true human septic conditions (Korneev 2019). Therefore, many variables need to be considered when selecting which animal model to utilize when studying sepsis. Table 4 depicts a summary of each model's specific advantages as well as their limitations and highlights their best use case scenarios.

Model	Advantages	Limitations
<i>Toxic agents are administered to induce sepsis (nonsurgical methods)</i>		
Systemic LPS administration	<ul style="list-style-type: none"> The model is easy to obtain, low invasive, controllable, standardized, and reproducible. The acute phase of Gram-negative sepsis is reproduced. Sepsis development is regulated by changing the LPS amount or its biological activity. Several alternative methods are possible for LPS administration. Manipulations with pathogens are avoided 	<ul style="list-style-type: none"> Hemodynamic, immunological, and metabolic features of sepsis are modeled poorly. Polymicrobial sepsis is not reproduced. A short-term immune response is usually triggered by LPS. LPS sensitivity differs between intraspecific and interspecific levels
LPS and D-GalN-induced toxicity	<ul style="list-style-type: none"> All the above applies. A lower LPS amount is needed because D-GalN increases the LPS sensitivity 	<ul style="list-style-type: none"> All the above applies. Septic shock develops rapidly, leading to early death
<i>Live pathogens are administered to induce sepsis (mostly by nonsurgical methods)</i>		
Bacteria introduced in the body	<ul style="list-style-type: none"> The model is easy to obtain, reproducible, and low invasive. Extreme clinical sepsis is modeled. The model is suitable for studying the immune response to a particular bacterial strain. Alternative methods are available for administering bacteria. Clinically relevant pathogenic bacterial strains are possible to use. Sepsis development is regulated by changing the number and composition of bacteria 	<ul style="list-style-type: none"> Hemodynamic, immunological, and metabolic features of sepsis are modeled poorly. Endotoxemia develops when bacteria are administered in large amounts. Certain bacteria do not induce sepsis because of their low persistence potential. One bacterial strain is commonly used, while sepsis is usually polymicrobial
Pneumonia-induced sepsis	<ul style="list-style-type: none"> The model is simple and reproducible. Sepsis development in diffuse pneumonia is modeled. Sepsis development is regulated by changing the bacterial composition or using antimicrobial therapies. Alternative low-invasive methods are available for administering bacteria 	<ul style="list-style-type: none"> Sepsis does not always develop. Hemodynamic phases are poorly distinguishable. Manipulations with pathogenic bacterial strains are necessary. Anesthesia is required in the case of intrabronchial administration. An inverted response develops to anti-cytokine therapy
Intraperitoneal administration of cecal slurry or fecal solution	<ul style="list-style-type: none"> The model is simple and reproducible. The model mimics polymicrobial peritonitis. The method is low invasive. The dynamics of sepsis development is regulated by changing the amount of the substance injected 	<ul style="list-style-type: none"> Metabolic, hemodynamic, and immunological features of sepsis are not always reproduced. The model is difficult to standardize because of the variation in microbiota composition and sample preparation. The body may be tolerant of its own microbiota
Intraperitoneal implantation of a fibrin clot infected with bacteria	<ul style="list-style-type: none"> The model mimics microbial peritonitis and is simpler than CLP or CASP. Early mortality is not induced. The model is suitable for studying mono-infections and their treatment with antibiotics. Sepsis development is regulated by changing the bacterial concentration and the clot density 	<ul style="list-style-type: none"> Reproducibility is problematic because the infected fibrin clot preparation and surgical technique are difficult to standardize. Tissues are wounded by surgery. One bacterial strain is often used, while sepsis is usually polymicrobial. The method does not work in newborn mice
<i>The integrity of barrier tissue is disrupted to induce sepsis (surgical methods)</i>		
Cecal ligation and puncture (CLP)	<ul style="list-style-type: none"> The model mimics the development of polymicrobial peritonitis with tissue ischemia. Both proinflammatory and anti-inflammatory immune responses are activated. Sample preparation is avoided (microbiota diversity is preserved to a maximum extent). Sepsis development is regulated by changing the puncture diameter or ligation site length and by dissection of the necrotic intestinal region 	<ul style="list-style-type: none"> Reproducibility is poor because standardization is difficult to achieve. Tissues are wounded by surgery. An abscess forms around the puncture site. The systemic inflammatory response is weaker than in CASP. The method does not work in newborn mice
Colon ascendens stent peritonitis (CASP)	<ul style="list-style-type: none"> Acute diffuse polymicrobial peritonitis is mimicked better than with CLP. Sepsis development is regulated by changing the stent diameter or removing the stent. An abscess does not form, unlike with CLP. Sample preparation is avoided (microbiota diversity is preserved to a maximum extent) 	<ul style="list-style-type: none"> The model is the most complex. Hemodynamic, immunological, and metabolic changes are less investigated than for CLP. A biphasic immune response is poorly reproduced. Tissues are wounded by surgery. The method does not work in newborn mice

Table 4 – Advantages and limitations of the most utilized sepsis animal models. Adapted from: Korneev (2019) (Rights obtained for use)

1.3.2 Lipopolysaccharide, a model for endotoxemia

An injection of lipopolysaccharide (LPS) was found to replicate much of the physiology of severe sepsis nearly 100 years ago and has continued to serve as a pillar for murine endotoxemia models in experimental studies (Rittirsch, Hoesel et al. 2007). The model consists of an injection of purified LPS, usually intra-peritoneally or intravenously, into mice and leads to a systemic activation of the innate immune system (Fink 2014). It is considered great for its ease of use, the ability to standardize dosage, and is less ethically concerning compared to models like CLP or CASP. However, this model is full of inherent limitations. Namely, the fact that LPS is just a single component of the complex pathogen associated molecular patterns (PAMPs) released by gram negative organisms. Moreover, it completely neglects major aspects of sepsis like host-pathogen interactions of gram-positive organisms and polymicrobial sepsis. Therefore, this model has recently been described as more of an intoxication model rather than a true septic model (Korneev 2019). Although, the same can be said for most purified bacterial injection models since it has been shown bacteria tend to not colonize and replicate in the body when given as a bolus injection, no matter the route of administration (Dyson and Singer 2009). Additionally, even for commercially available products, it is critical to determine which LPS

preparation was utilized as products of lesser purity may contain other molecules, such as deoxyribonucleic acid (DNA) or ribonucleic acid (RNA), which are known to modulate the host immune response (Lewis, Seymour et al. 2016). Yet, LPS has been an instrumental tool for interrogating specific biological mechanisms and pathways, such as the immune response to prototypical stimuli of specific toll-like receptor (TLR) pathways. However, in relation to sepsis, great caution should be used when interpreting results utilizing this method, as many of the behaviors do not mimic a true septic state. This was highlighted by clinical trials of tumor necrosis factor α (TNF- α) inhibitors, which displayed impressive protection and was initially a great therapeutic promise when tested in murine LPS models. Unfortunately, the human clinical trials that followed failed to show any mortality rate benefit, which could have been predicted from CLP models that similarly demonstrated reduced survival (Remick, Manohar et al. 1995, Remick and Ward 2005, Rittirsch, Hoesel et al. 2007). Consequentially, it is now suggested to use LPS for preliminary investigative studies, followed by the use of a more representative septic model, such as CLP, for proof of concept (Rittirsch, Hoesel et al. 2007).

1.3.3 Cecal ligation and puncture and colon ascendens stent peritonitis

Clowes et al. (1968) introduced the first cecal ligation model, where they found sepsis can be induced in dogs, and later pigs (Wright, Duff et al. 1971, Imamura and Clowes 1975), by cecal ligation below the ileocecal valve. This procedure had quite positive results, and replicated hemodynamic changes, fever, and respiratory alkalosis, as seen in many human patients. However, at the time, the number of pigs and dogs that could be used for experimental study was limited due to the high costs involved. Therefore, Wichtermann et al. (1980) investigated if this model could be adapted to rats since they are inexpensive, available in large numbers, genetically identical, the same sex and age, on the same diet, and specific pathogen free. They found that cecal ligation alone produced a necrotic cecum and a localized intraperitoneal abscess which rats easily isolated off. However, puncturing the cecum, thus violating its integrity, led to a reproducible small animal model of sepsis resulting in septic shock. This method is known today as Cecal Ligation and Puncture (CLP) and has become the “Gold Standard” when modeling sepsis in animals for its simple experimental procedure, which is represented by polymicrobial infection of the peritoneum with a localized infectious focus (Schabbauer 2012), Figure 14(A). Nevertheless, in recent years much scrutiny has encircled this method. One main contributing factor stems from its lack of reproducibility (Dyson and Singer 2009). Even though Wichtermann et al. (1980) described a standardized protocol, many experimenters often alter the protocol, accidentally or on purpose, by using different ligation strengths and positions on the cecum as well as using different gauged needles and number of puncture holes. Proponents of CLP see this variation as a benefit since the severity of sepsis can be adjusted by varying these parameters (Buras, Holzmann et al. 2005). However, this has inevitably led to experimental variability in the time course of sepsis, making day to day measurements challenging to compare with previously published works. Moreover, as discovered by bacterial injection studies, every rat has a unique gut microbiome and, therefore, the type of bacteria leaked cannot be standardized, with the use of different rat strains as well as inter-animal differences compounding this issue (Schabbauer 2012). Recently, this lack of robustness, in combination with its seemingly lack of relevance to human sepsis, has caused increased scrutiny of this protocol in relation to animal ethics and animal welfare activists, with many institutions or states, such as Baden-Württemberg, banning or outright rejecting project proposals using the CLP method. However, CLP still stands as a crucial model for sepsis to inform novel pathways of sepsis physiology and its therapeutic direction (Alverdy, Keskey et al. 2020). In addition, its inability to mimic all elements of the human septic state is not unique to this model and is common for all mouse sepsis models.

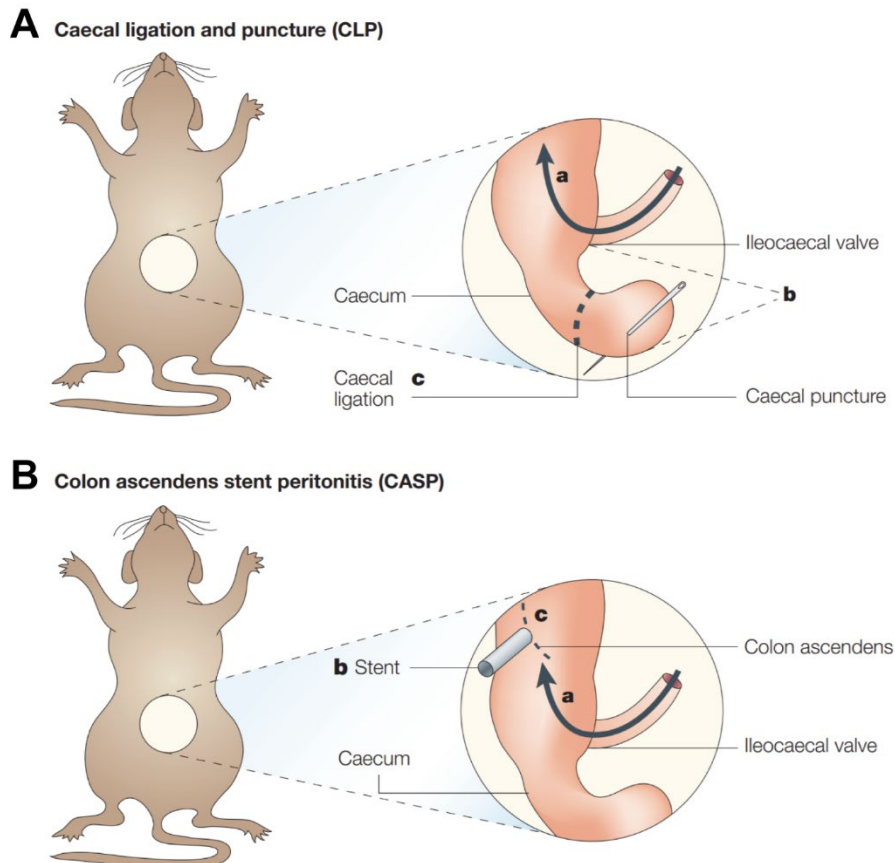


Figure 14 - Surgical methods for cecal ligation and puncture and colon ascendens stent peritonitis experimental sepsis models. Visual representation of (A) CLP and (B) CASP surgical techniques. Adapted from: Buras, Holzmann et al. (2005) (rights obtained for use)

Introduced by Zantl et al. (1998), colon ascendens stent peritonitis (CASP) is closely related to CLP for producing abdominal sepsis in rodents but could reflect different kinds of disease states (Lewis, Seymour et al. 2016). In recent years, this model has begun to replace, or in some cases complement, the CLP model. For the CASP model, mice are anesthetized, and a midline laparotomy is performed, followed by the insertion of a plastic stent into the ascending colon of the mouse, approximately 1 cm distal to the ileocecal junction. The stent is then fixed to the ascending colon with two sutures, allowing for a continuous flow of fecal matter into the abdominal cavity, Figure 14(B). CASP seems to reproduce generalized peritonitis, as well as changes in lung, kidney, and bone marrow dysfunction as observed in human sepsis, with the magnitude of the septic insult titratable by altering the size of the stent (Lewis, Seymour et al. 2016). Moreover, unlike CLP, this method was initially described and created for mice, rather than adopting the model from large to small animals (Wichterman, Baue et al. 1980). As opposed to CLP, CASP can also be reversed at different time points in order to mimic surgical intervention, as demonstrated by Zantl et al. (1998) who revealed that early intervention, at three hours, could revive mice but late intervention, at nine hours, resulted in a 100% mortality rate. Additionally, this model resulted in a steadily increasing and more pronounced amounts of systemic bacterial dissemination, which yielded greater inflammatory cytokine concentrations at all time points measured. In particular, CASP survival was found to be independent of TNF- α in contrast to CLP, however, the exact mechanism for this is still unclear. CASP also displayed the ability to maintain a constant flow of fecal matter into the abdominal cavity since the stent did not seal over time, whereas with CLP the ligated cecum was rapidly covered by adhesive small bowel loops, which is more than likely one of the main cause of the differences between these models (Lewis, Seymour et al. 2016). Nevertheless, CASP is considered the most complex model to date, making implementation into a lab setting difficult.

Additionally, the hemodynamic and metabolic changes in the model have not been characterized as completely when compared to CLP, and the biphasic immune response in sepsis is not reproduced since the anti-inflammatory cytokine response arises almost parallel to the pro-inflammatory response (Korneev 2019). Both models also share the common disadvantage of not being applicable to newborn mice (van der Poll 2012).

1.3.4 Cecal slurry

Although the cecal slurry model of sepsis is a relatively new protocol (Gonnert, Recknagel et al. 2011), it had many roots before becoming what it is today. Indeed, models for intraperitoneal sepsis date back to the 1960s and 70s where they injected purified *E. coli* bacteria cultures, either intravenously or interperitoneally. However, this resulted in either too high of a mortality rate in small animal models or no systemic effect in larger animals. This effect was highlighted by Wicherman et al. (1980) where he noted that most patients are not challenged with a massive bacterial load at once, but a persistent showering of the body with bacteria. Even today, many authors still question the relevancy of animal models utilizing a “bolus” infusion of viable bacteria. To mitigate this effect, Ahrenholz and Simmons (1980) intraperitoneally implanted a bovine fibrin clot impregnated with the same number of injected bacteria and found that this prevented early mortality rates. Although rats developed abscesses and the 10-day mortality rate was 90 %. Another noteworthy method was described by Alexander et al. (1989) who was able to control the flow and type of infecting organisms. In this model, Alzet osmotic minipumps containing viable *E. coli* and *S. aureus* are implanted intraperitoneally into guinea pigs, which allowed full control over leakage over time and amount. Here, they established a well-working chronic model of sepsis with a mortality rate of 50 % at day 18, often accompanied by pneumonia, and reproduced key features of chronic sepsis in humans. Though, it was not until 2004 when Brealey et al. (2004) introduced the first fecal slurry model of sepsis in rats. Here, a fresh fecal slurry solution was prepared from the bowel contents of a rat from the same batch, suspended in n-saline, and filtered to remove fibrous material. This slurry was then intraperitoneally injected into rats at 0.625 ml/100 g body weight. Fluid resuscitation was commenced two hours later via the femoral venous cannula and rats were sacrificed at 4, 24, 48, and 72 hours after the septic insult. Brealey et al. (2004) found a progressive mitochondrial dysfunction related to disease severity and nitric oxide (NO) production, with improvement on resolution of the illness, were reflected in both vital (liver) and nonvital (hind limb skeletal muscle) tissues. This finding was considered extremely pertinent to translational studies in human patients since skeletal muscle is more readily and safely accessible for biopsies. Moreover, they found severely septic rats had hepatic and muscle complex I activities that were 20 – 22 % lower at 24 hours, corroborating with the differences seen between septic and control human patients. Interestingly, despite evidence of inflammation and biochemical multiorgan dysfunction, they found a lack of histological damage and cell death in myocardium, lung, liver, and kidney samples. Though, Hotchkiss et al. (1999) reported similar results on postmortem samples taken from septic patients who died from multiorgan failure. They postulate that when organs are met with a prolonged and systemic inflammatory insult, they respond by switching off their energy-consuming biophysiological processes in a last-ditch attempt to prevent irreversible cell damage, which has been well documented in ischemic heart disease (Hearse 1997). However, it is important to note only 26 out of 143 septic rats survived to the 72 hour mark, with none being classified as a severe case and 11 showing signs of improvement in their clinical condition. In addition, this model produced a spectrum of the disease from mild to severe, despite their efforts using a standardized protocol on a seemingly homogeneous population of similar size and age. They also note a marked variation in the clinical response despite using the same slurry in up to six rats from the same litter at the same time (Brealey, Karyampudi et al. 2004). In accordance with many critics of this method, these findings

highlight the protocols inability to quantify the amount and type of bacteria injected for freshly prepared fecal slurries, unlike other live pathogen methods at the time (Buras, Holzmann et al. 2005). Thus, further exacerbating the variability in an already seemingly unpredictable protocol. To alleviate this, Gonnert et al. (2011) introduced the idea of large batch preparation for fecal slurries. Pooled stool samples from three healthy, non-vegetarian, human donors were diluted 1:1 with a pre-reduced thioglycolate suspension and a catalase added for optimal bacterial growth and inactivation of reactive oxygen species. 10% glycerol was then added for cryo-preservation and the suspension homogenized under anaerobic conditions. Lastly, the suspension was aliquoted and stored at -80°C until use. To induce sepsis, 1.75 ml/kg body weight of stool suspension was injected into the abdominal cavity of rats. They found this caused a 100% mortality rate by 40 hours post induction, as opposed to the 50% mortality rate observed when treatment with antibiotics starting two hours post-insult was employed (Gonnert, Recknagel et al. 2011). However, as recently emphasized by Steele et al. (2017), early intervention, initiated before the development of bacteremia, could halt the progression from local to systemic infection and block downstream pathology otherwise characteristic of severe sepsis. Steele et al. (2017) found that only 25% of animals were positive for circulating bacteria one hour after cecal slurry (CS) injection, and 50% of animals were still negative for circulating bacteria at six hours. Thus, raising the question if starting intervention as early as two hours post-insult produces an intoxication model rather than a true septic model. Unfortunately, Gonnert et al. (2011) did not include any information concerning the bacterial load of the blood or any organs. Even though they did include initial information concerning the microbiological composition of the stool, they failed to demonstrate how the storage conditions effected the fecal slurry solution over time, only stating the analysis was repeated three years after the initial analysis and the number of colony forming units (CFUs) was substantially lower. Gonnert et al. (2011) does point out that rats were chosen for this study as they allow for repeated blood collection and major instrumentation but, in principle, the procedure could also be feasible in mice. Indeed, many authors used this method for mice but continued to use freshly prepared fecal slurries in lieu of batch processing and storage (Nowak, Harmon et al. 2012, Zolfaghari, Pinto et al. 2013, Shrum, Anantha et al. 2014). However, this trend started to shift in 2014 when Starr et al. (2014) quantified and established a new CS preparation protocol for use in mouse models. Interestingly, Starr et al. (2014) decided to use cecum contents, rather than fecal matter, in an attempt to create a method more comparable to that of CLP. Here, cecal contents were collected from donor mice, combined, weighed, and mixed with sterile water in a 0.5 ml water for every 100 mg of cecal content ratio. This solution was then strained through three mesh filters to remove debris and mixed with an equal volume of 30% glycerol in phosphate buffered saline (PBS), resulting in a final stock solution in 15% glycerol. Lastly, the stock CS solution was aliquoted and stored at $+4$, -20 , or -80°C for later comparison. They found CS stored at -80°C had no significant drop in bioactivity for up to six months when compared to one month storage bioactivity levels, while $+4$ and -20°C storage conditions exhibited over a 50% decrease after only six weeks of storage. Thus, quantitatively alleviating concerns of how long-term storage could impact CS solutions over time. As alluded to previously, they also found levels of circulating bacteria exceeding the amount of bacteria administered, providing evidence of replication. Thus, supporting the notion the CS method is, in fact, an infectious model and not an intoxication model, despite contrary reports (Cross, Opal et al. 1993). However, they did fail to fully characterize the bacterial content of the CS stocks, which would have given evidence to what proportion of aerobic and anaerobic bacteria can survive cryopreservation, as well as making their method simpler to replicate. Moreover, unlike many previous studies (Gonnert, Recknagel et al. 2011, Shrum, Anantha et al. 2014), they did not employ any type of sepsis scoring or classification system and, rather, relied heavily on mortality rate as an indicator of a successful model, which was also the case in their follow-up article published by Steele et al. (2017). Taken at face value, this would seem fairly irrelevant.

Yet, this information is crucial for such a time sensitive disease as sepsis and would have served the purpose of determining the time course of their model, i.e. the length of time mice are in a septic state as well as their recovery period. However, Steele et al. (2017) did go on to further optimize the CS model of sepsis. They found that the addition of 10% glycerol, rather than 15%, for cryopreservation lessened possible physiological stress upon injection, while still maintaining bacteria viability during storage. Additionally, they increased the number of straining steps from two, or optionally three, to four which better prevented clogging of the needle during injection. They went on to evaluate the differences between early (1 – 6 hours post insult) and late (≥ 12 hours) therapeutic intervention with fluid and/or antibiotics. Here, they found that the late therapeutic intervention, i.e. after bacteria was confirmed in circulation, resulted in elevated IL-6, IL-1 β , and TNF- α levels 24 hours after CS insult, compared to early intervention. Additionally, lung injury as well as liver dysfunction was characteristic only in the case of late therapeutic intervention. Thus, reiterating the importance of timing for CS and other live pathogen models of sepsis.

1.3.5 Less common models of sepsis

Other noteworthy models of sepsis include pneumonia induced sepsis and urosepsis. Unlike many sepsis models which mimic extreme abdominal sepsis, akin to a ruptured diverticulum in a patient suffering from diverticulitis, these models represent a slower onset, secondary infection, type of sepsis. Thus, allowing more time to study the progression of the disease. Moreover, pneumonia induced sepsis is the most common cause in humans, being responsible for almost 50% of all sources of infection (Angus, Linde-Zwirble et al. 2001, Alberti, Brun-Buisson et al. 2002, Sordi, Menezes-de-Lima et al. 2013, Lewis, Seymour et al. 2016) and can be induced in mice by intra-nasal or intra-tracheal delivery of bacteria or via inhalation of aerosolized mist (Lewis, Seymour et al. 2016). This model also makes it possible to mimic community-acquired pneumonia by administering *P. pneumoniae* and *S. pyogenes* pathogenic strains or hospital-acquired pneumonia by administering *P. aeruginosa*, *K. pneumoniae*, *S. aureus*, and *A. baumannii* strains. However, the most interesting aspect of this model stems from its use in “two hit” models of sepsis. An initial insult, usually as abdominal sepsis via CLP, is delivered, followed by later administering bacteria to the respiratory system. This mimics the development of hospital-acquired pneumonia in human patients after trauma or abdominal sepsis (Muenzer, Davis et al. 2006). Urosepsis, on the other hand, accounts for approximately 25% of all septic patients and may develop from a community or nosocomial-acquired urinary tract infection (UTI) (Brun-Buisson 2000). This method involves a bacterial injection, usually *Escherichia coli*, into the bladder of mice and produces an ascending UTI (Hagberg, Engberg et al. 1983). Even though this method has been used for several decades to study UTIs, there are only a handful of publications that have utilized this model in mice to study sepsis, with most available data on urosepsis coming from randomized clinical trials and case studies (Wagenlehner, Pilatz et al. 2011).

1.4 Muscle anatomy and sepsis induced myopathies and neuropathies

1.4.1 General muscle anatomy

Skeletal muscle is a highly malleable, multinucleated tissue which plays a central role for locomotion, thermoregulation, oxygen consumption, energy metabolism, substrate turnover and storage, as well as overall energy homeostasis. In humans, it accounts for 45 – 50 % of total body mass and is under voluntary control of the somatic nervous system, although some functions, such as shivering to address hypothermia are autonomous (Nakamura and Morrison

2011, Liu, Saul et al. 2018). Depending on a muscle's size and anatomical location, it can wildly vary in length as well as diameter and are attached to bones by bundles of collagen fibers known as tendons. The general organizational structure of skeletal muscle begins with an outermost fibrous elastic layer referred to as the epimysium. Within this layer blood vessels and nerves run alongside fascicles. Each fascicle is surrounded by a connective tissue layer, the perimysium, and contains many muscle fibers that are individually ensheathed by another fine connective tissue layer, the endomysium. Each muscle fiber is considered a single muscle cell and is enclosed by the muscle plasma membrane, made up of a phospholipid bilayer with embedded proteins, glycoproteins, and glycolipids, called the sarcolemma. Inside, a bundle of myofibrils is surrounded by the sarcoplasm which contains several nuclei, sarcoplasmic reticulum, golgi apparatus, mitochondria, lysosomes, glycogen granules, enzymes, and other soluble constituents vital for muscle function, Figure 15 (Tortora and Derrickson 2012). Moreover, skeletal muscle can be composed of muscle fiber type I, IIA, IIX, or IIB, which are characterized by their contraction speed and preferred metabolic pathway for glycogen degradation. Here, Type I fibers represent slow-twitch, red pigmented fibers, and use oxidative metabolism; Type IIA fibers are fast-twitch, red, with intermediate oxidative or glycolytic metabolism; and Type IIB and IIX fibers are fast-twitch, white, with glycolytic metabolism (Schiaffino and Reggiani 2011).

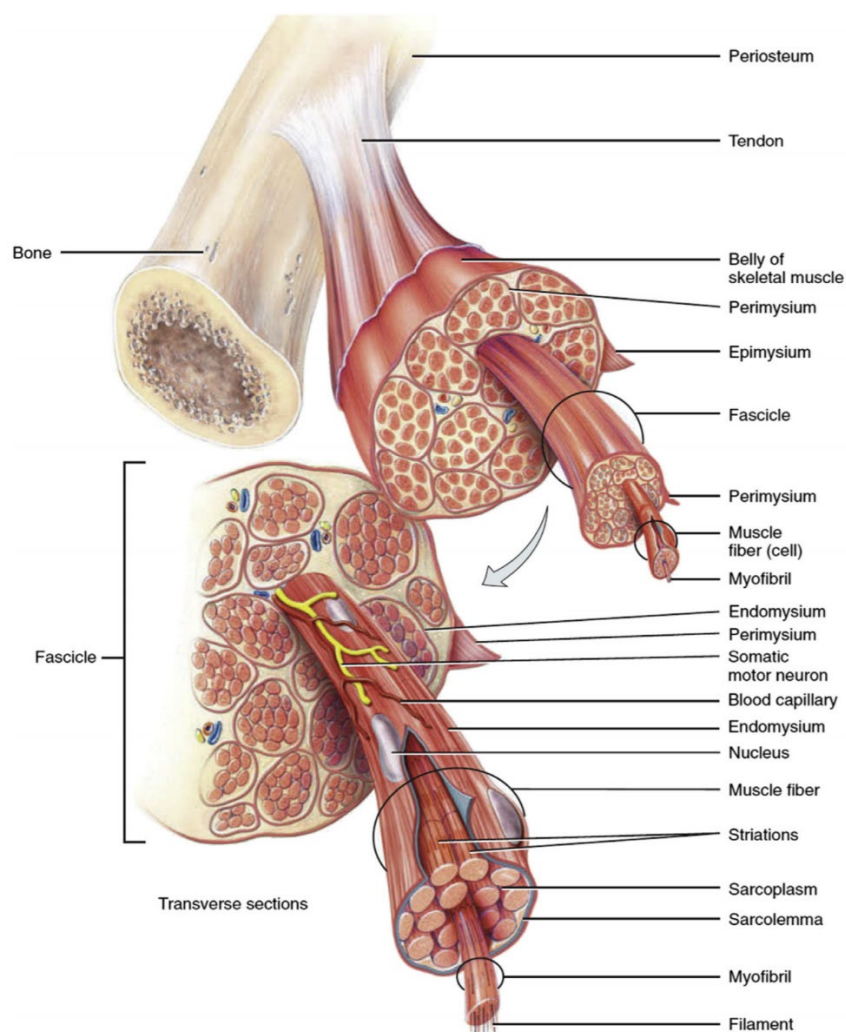


Figure 15 – Overview of skeletal muscle anatomy. Adapted from: Tortora and Derrickson (2012) (Rights obtained for use)

However, regardless of fiber type, the enclosed individual myofibrils all consist of a strand of repeating units between Z-plates, the sarcomere, which represents the basic functional unit of

muscle, Figure 16(A). Within the sarcomere, the filamentous contractile protein myosin forms the thick filaments of muscle cells and is the principal component of the A-band. Myosin itself, has a quaternary structure consisting of six subunits, including: two myosin heavy chains (MHC), two essential myosin light chains (MLC1) and two regulatory myosin light chains (MLC2), with molecular weights (MW) of approximately 220 kDa, 23 kDa, and 20 kDa, respectively. Regarding MHC, four primary isoforms can be found in skeletal muscle and consist of MHC I, IIa, IIb, and IIx, which purely exist in either slow-twitch fiber type I, fast-twitch fiber type IIa, IIb, or IIx, respectively. Although, it is important to note that hybrid fiber types containing different myosin isoforms do exist (Clark, McElhinny et al. 2002, Schiaffino and Reggiani 2011). The other main contractile protein found in the sarcomere is actin, which has a MW of 42 kDa and is the building block of thin filaments and is denoted visually by the I band, Figure 16. It is present as globular actin (G-actin) as well as filamentous actin (F-actin) that is formed by the polymerization of G-actin into double-stranded, coiled filaments (Clark, McElhinny et al. 2002). For a muscle to contract, myosin and actin undergo a sequence of molecular events known as crossbridge cycling. When a muscle is in a relaxed state, myosin heads are bound to actin filaments. The crossbridge cycling begins when ATP binds to the myosin head, releasing myosin from the actin filament. ATP is then split into ADP, a phosphate group, and releases energy. The released energy moves the myosin head into a high energy “cocked” position. Next the myosin head attaches itself to the next site on the actin filament and releases the inorganic phosphate group. This initiates the “power stroke” and moves the actin filament inwards, thereby shortening the sarcomere. At the end of the power stroke, ADP is released from the myosin head, leaving myosin tightly bound to actin in a rigor state until another ATP binds to myosin. During this process, the thick filament containing A band stays the same length. However, as the actin filaments are moved inwards towards the m-line and overlap the myosin filaments, the I band and H zone become shortened, Figure 16 (Tortora and Derrickson 2012).

There are two main proteins, tropomyosin and troponin, responsible for regulating muscle contraction and relaxation as they prevent the activation of actomyosin ATPase in the absence of calcium ions by interacting with actin filaments to block the myosin binding site. Tropomyosin is a long, coiled protein with a MW of 65 kDa that binds head-to-tail along the F-actin filament. Moreover, each tropomyosin protein is attached to a troponin complex which is made up of troponin C, troponin I, and troponin T, with MWs of 18, 21, and 31 kDa, respectively (Boland, Kaur et al. 2018). Here, troponin C acts as the calcium binding site, troponin T connects the troponin complex to tropomyosin, and troponin I inhibits actomyosin ATPase activity when it is bound to actin. When a muscle is stimulated to contract, the sarcoplasmic reticulum releases calcium ions which bind to troponin C and induces a conformational change of troponin. This results in tropomyosin sliding out of the way and allows crossbridge cycling to begin. When relaxed, calcium ions are actively pumped back into the sarcoplasmic reticulum, causing troponin to revert to its original conformation and, thus, covering the binding sites on the actin filament again (Krans 2010).

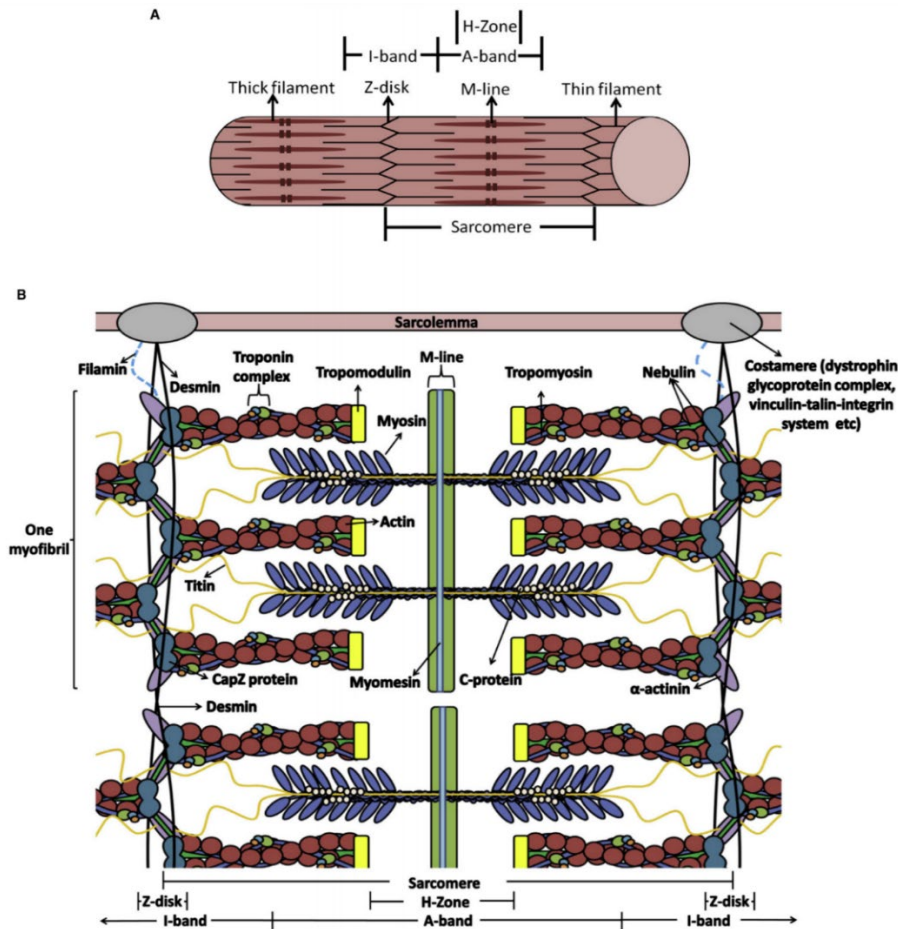


Figure 16 - Structural proteins and the organization of the sarcomere. Adapted from: Boland, Kaur et al. (2018) (Rights obtained for use)

In addition to contractile and regulatory proteins, many structural proteins are also present within each sarcomere and control the filamentous structure and integrity of myofibrils, Figure 16. For clarity, Table 5 lists many of these structural proteins, their molecular weight, and their specific function within the sarcomere (Clark, McElhinny et al. 2002).

Protein	Molecular weight (kDa)	Function	Location
Titin	4200	backbone of thick filaments in the A-band molecular spring in the I-band provides elasticity to the sarcomere during muscle contraction	throughout the entire length of the sarcomere
Nebulin	800	regulates the length of the thin filaments	spans from the sarcomeres Z - disk to near the tip of the thin filament
α - Actinin	95	supporting and attaching actin to the Z-disk	principal constituent of the Z-disk
β - Actinin	α - subunit 37 β - subunit 34	binds α - actinin in the Z-disk Prevents network formation between actin filaments	end of thin filaments and the Z - disk
Tropomodulin	40	binds tropomyosin and actin control the length of thin filaments by maintaining the number of G - actin monomers	near the m - line
Desmin	55	major role in linking myofibrils to the sarcolemma	at the Z - disk
Filamin	300	stabilizing muscle structure	
C - protein	140	believed to contribute to the alignment and stabilization of thick filaments	A - band of thick filaments
H - protein	58		
Myomesin	185	binding titin and myosin maintaining the structure of thick filaments	major protein in the M-line

Table 5 - structural proteins molecular weight, function, and location in the sarcomere. Information compiled from: Clark, McElhinny (2002)

1.4.2 Muscle innervation and the neuromuscular junction

For a muscle to contract, it must receive a neuronal signal from the brain. This is accomplished by myelinated motor neurons which individually innervate each muscle fiber within a muscle and are joined to approximately 0.1% of the muscle fiber's cell surface. Acetylcholine receptors (AChRs), a ligand gated ion channel, are localized to this small spot of the muscle fiber membrane and is known as the neuromuscular junction (NMJ). Synaptic transmission at the NMJ begins when an action potential reaches the presynaptic terminal of the motor neuron. In

turn, this activates voltage-dependent calcium channels and allows calcium to enter the neuron. Calcium ions then bind to sensor proteins on synaptic vesicles carrying acetylcholine (ACh), triggering their fusion with the presynaptic cell membrane, and ACh is then released into the synaptic cleft. ACh then binds to nicotinic acetylcholine receptors located on the postsynaptic cleft, where sodium (Na) is released, and the action potential is perpetuated through the muscle fiber, Figure 17 (Tortora and Derrickson 2012).

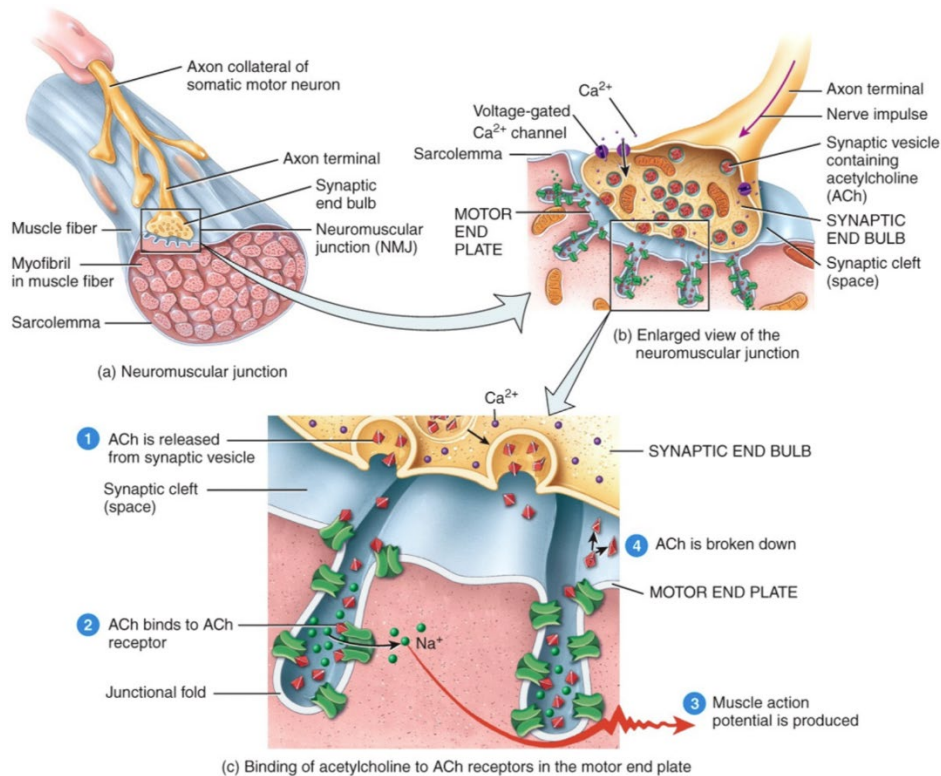


Figure 17 – Synaptic transmission at the neuromuscular junction. After calcium binds to synaptic vesicles due to an action potential, (1) acetylcholine (ACh) is released into the synaptic cleft and (2) binds to acetylcholine receptors (AChRs) located on the postsynaptic cleft. (3) Sodium is then released and an action potential is produced. (4) ACh is then broken down by acetylcholinesterase (AChE) and sent back into the presynaptic neuron where it is recycled for future use. Adapted from: Tortora and Derrickson (2012) (Rights obtained for use)

1.4.3 Sepsis, muscle, and the intensive care unit

Although skeletal muscle displays highly adaptive and regenerative properties and is able to compensate for up to a 20% loss of muscle mass, many factors including disuse, aging, starvation, genetic, and a number of disease states can induce atrophy (Liu, Saul et al. 2018). However, regardless of the inciting cause, skeletal muscle atrophy is characterized by a decrease in protein content, fiber diameter, force production, and fatigue resistance (Jackman and Kandarian 2004). While severe sepsis has been associated with the involuntary loss of muscle mass, referred to as muscle wasting, as far back as 1892 by William Osler, this phenomenon remains a frequent complication of critical illness (Osler 1892). Moreover, with the many advancements in modern intensive care medicine, more patients survive the initial stages of systemic inflammation/sepsis. Consequently, an increasingly number of patients are confronted with profound muscle weakness, often accompanied by difficulties weaning from a ventilator, and sepsis-associated long-term complications. One such complication includes long-term peripheral muscle weakness, which results in functional impairment, exercise limitation, and lower than normal health-related quality of life which can persist for years after discharge from the intensive care unit (ICU). Additionally, such impairment could induce a vicious cycle of secondary complications which need repeated or intensified medical therapy,

resulting in increased morbidity and mortality (Friedrich, Reid et al. 2015, Schefold, Wollersheim et al. 2020).

1.4.4 The imbalance between muscle regeneration and degradation in septic induced muscle wasting

Muscle wasting is a distinct disease entity which results in a loss of muscle mass due to semi-unspecific fiber type muscle atrophy. However, muscle force capacity may remain stable in muscle wasting syndromes (Callahan and Supinski 2009). It can be triggered by sepsis, as well as other conditions including disuse, denervation, fasting, cancer, cardiac failure, and renal dysfunction (Schefold, Bierbrauer et al. 2010). The main mechanism of muscle atrophy in muscle wasting is thought to be caused by an imbalance between muscle protein synthesis and muscle protein degradation and results from decreased protein synthesis and/or increased protein degradation (Callahan and Supinski 2009). Unfortunately, conditions other than sepsis frequently coincide within the ICU setting, and, as such, can be extremely difficult to determine the underlying cause. However, animal models, where sepsis can be separated as its own entity, have clearly indicated a decrease in protein synthesis in skeletal and respiratory muscles (Orellana, O'Connor et al. 2002, Lang, Frost et al. 2007), as well as preferentially inhibiting myofibrillar and sarcoplasmic protein synthesis within fast twitch muscles (Vary and Kimball 1992). One major pathway involved in muscle protein synthesis is the IGF1-PI3K-Akt/PKB-mTOR pathway. However, during critical illness, components of this pathway are considerably down regulated. Moreover, mTOR activation presents an important downstream target of anabolic insulin/insulin like growth factor 1 (IGF-1), and since decreased insulin sensitivity is a frequently observed complication of sepsis, this pathway could be impaired (Schefold, Wollersheim et al. 2020). In addition, proinflammatory cytokines IL-6 and TNF- α have both been linked to insulin resistance and muscle atrophy. One study found that local IGF-1 application prevents sepsis induced muscle atrophy, possibly by inhibiting sepsis induced increases of muscle atrogen-1 and IL-6. IL-1 may also lead to decreased protein synthesis as an animal model has shown cytokine dependent decreases of phosphorylated eukaryotic initiation factor 4E (eIF4E), another important translation initiation factor for protein synthesis (Friedrich, Reid et al. 2015). Furthermore, nutritional aspects may also contribute to decreased muscle protein synthesis, as administration of the essential branched chain amino acid leucine has been shown to increase protein synthesis in rat skeletal muscles during ageing, exercise, or food deprivation. Moreover, a nutritional deficit rapidly develops during critical illness due to a dysfunction of the gastrointestinal track. While it could be postulated that this deficit could be reversed by feeding patients the required nutritional supplements in order to improve muscle protein synthesis and decrease the need for muscle degradation to obtain these essential molecules, randomized clinical trials have given inconclusive results with reports of both beneficial and detrimental results when comparing non-fed and fed patients (Schefold, Bierbrauer et al. 2010, Friedrich, Reid et al. 2015).

Marked increases in sepsis-associated muscle protein degradation starts early during the course of the disease, with patients presenting a shift in protein homeostasis towards breakdown on the first day after ICU admission. Muscle protein degradation is mediated by two key systems, the ubiquitin-proteasome pathway (UPS) and autophagy (Schefold, Wollersheim et al. 2020). Muscle RING-finger protein-1 (MuRF1) and atrogen-1 are E3-ligases that are considered to play key roles during muscle atrophy as they represent substrate specific enzymes involved in the UPS that prevent unselective degradation by the proteasome and have been shown to be increased during experimental trophic conditions (Ebert, Al-Zougbi et al. 2019). Moreover, myosin heavy chain and other myofibrillar proteins including myosin binding proteins have been identified as MuRF1 substrates, while atrogen-1 is associated with MyoD and eIF3-f

substrates, both of which are known to regulate protein synthesis. Therefore, it could be possible that atrogin-1 leads to muscle atrophy by selective breakdown of key regulators of protein synthesis. FoxO1 and FoxO3 expression is induced during the early stages of critical illness and are relevant for the development of muscle atrophy. FoxO3 has been shown to directly induce atrogin-1 and the induction of both members of the FoxO transcription factor family reflects an upregulation of MuRF1, atrogin-1 mRNA expression, and respective proteins. Additionally, MuRF1-mediated muscle protein degradation can also be activated by NF κ B, which is disinhibited through TNF- α via IKK β , Figure 18 (Khalil 2018).

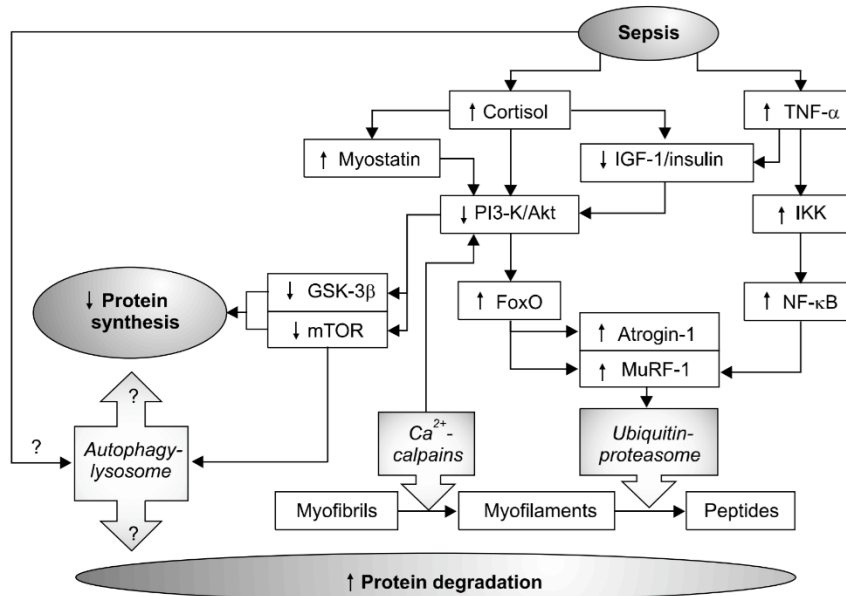


Figure 18 - Proposed mechanisms of muscle wasting in sepsis. Adapted from: Lee and Kim (2010) (Free to use under CC license)

1.4.5 Risk factors contributing to muscle atrophy within the intensive care unit

However, sepsis is not only associated with muscle wasting but also severe neuromuscular dysfunction resulting in an acquired weakness. Unfortunately, a confusing number of terminologies have been used in the past to describe similar or identical clinical presentations of this neuromuscular dysfunction. Though, in 2009, the umbrella term ICU acquired weakness (ICUAW) was established (Stevens, Marshall et al. 2009). However, it is important to note that while ICUAW is usually accompanied by muscle wasting, muscle wasting does not necessarily lead to neuromuscular dysfunction, since overall muscle strength depends on both total muscle mass and force generating capacity, which is affected in ICUAW but not always in muscle wasting (Scheffold, Wollersheim et al. 2020). ICUAW represents a bedside diagnosis of symmetric muscular weakness and decreased muscular tone, typically of the lower limbs, in patients with critical illness, with an extremely high occurrence affecting 70 % to 100 % of these patients. This weakness appears to be caused by critical illness in combination with the ICU course and can either affect the peripheral nerves (critical illness polyneuropathy, CIP) or skeletal muscle (critical illness myopathy, CIM) (Friedrich, Reid et al. 2015). However, while the classical descriptions of these syndromes have been largely based on electrophysiologic testing and defined by the presence of either a primary neuropathic process or a primary myopathic process, it is now apparent that the acquired weakness seen in many septic patients manifests from both a neuropathy and myopathy (critical illness polyneuromyopathy, CIPM). Nonetheless, the distinction between CIM and CIP in patients is of utmost importance as adjustments to, or different treatment regimens are needed depending on the underlying cause and must be addressed in a case-by-case manner (Scheffold, Wollersheim et al. 2020).

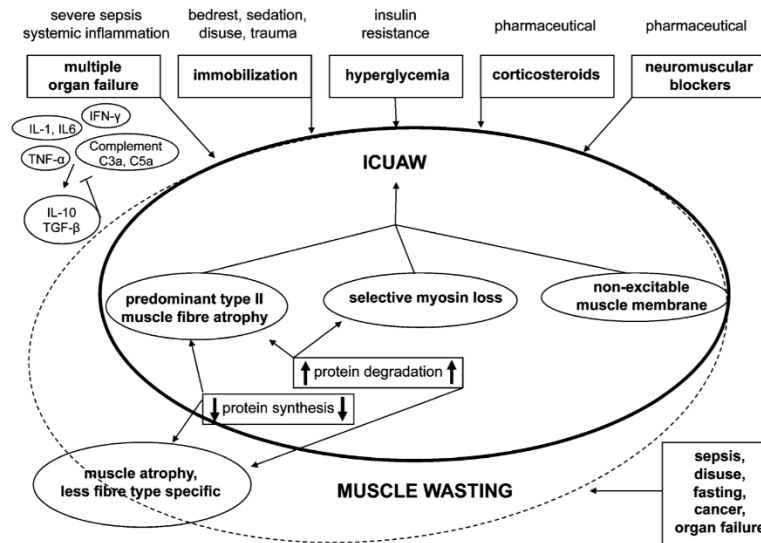


Figure 19 - Risk factors involved in muscle wasting and ICUAW. Adapted from: Schefold, Bierbrauer et al. (2010) (Rights obtained for use)

Many critically ill patients diagnosed with CIM exhibit several symptoms and alterations at the organ, cellular, and subcellular level of affected muscles, which may not all be detectible in each patient or at a given stage. These alterations include electrical hypoexcitability of muscles, severe and predominant type II muscle fiber atrophy, disorganized sarcomeres, ultrastructural abnormalities, impaired autophagy, and altered protein turnover. Moreover, the preferential and significant loss of myosin while the expression of thin filament proteins is maintained is a hallmark of CIM in ICU patients (Friedrich, Reid et al. 2015). While many risk factors including neuromuscular blockade, systemic administration of corticosteroids, hyperglycemia, and sepsis, Figure 19, have been accredited as important triggers for this type of acquired myopathy, instances have been reported in the absence of all these triggers, with mechanical ventilation almost always found in these patients and is therefore thought to be the major cause of CIM in ICU patients. Moreover, it is not known whether severe sepsis and sepsis induced organ failure are sufficient to create the full-blown manifestations of CIM, with sepsis animal models hinting towards a differential pathophysiological process in pure sepsis as the preferential loss of myosin has not been observed in these models (Schefold, Bierbrauer et al. 2010). On the other hand, CIP can be described by more distal than proximal weakness, sensory changes, and atrophy with preferential myosin loss. Histologically, the main distinguishing factors of CIP from CIM include axonal degeneration and the loss of myelinated fibers in peripheral motor and sensory nerves (Schefold, Wollersheim et al. 2020), Table 6.

Clinical Signs	Critical illness polyneuropathy	Histological Findings
<ul style="list-style-type: none"> -Flaccid, symmetrical atrophy, and weakness of the limbs -Distal > proximal -Lower limb > upper limbs -Facial muscles mostly spared -Deep tendon reflexes mostly reduced to absent but may be preserved -Variable distal sensory loss to pain, temperature, and vibration -Weaning failure 	<p>Critical illness polyneuropathy</p> <p><i>Nerve:</i></p> <ul style="list-style-type: none"> -Normal -Mildly reduced myelin fiber density with sporadic axonal degeneration -Marked fiber loss with abundant degenerative changes -Variable fiber regeneration -no evidence of primary demyelination or inflammatory infiltrates <p><i>Muscle:</i></p> <ul style="list-style-type: none"> -Denervation atrophy 	
<ul style="list-style-type: none"> -Flaccid, symmetrical atrophy and weakness of the limbs and neck flexors -Proximal > distal -Facial muscles mostly spared -Deep tendon reflexes mostly reduced to absent but may be preserved -No sensory loss -Weaning failure 	<p>Critical illness myopathy</p> <p><i>Nerve:</i></p> <ul style="list-style-type: none"> -Normal <p><i>Muscle:</i></p> <ul style="list-style-type: none"> -Fiber atrophy with abnormal variation in size of muscle fibers, angulated fibers, fatty degeneration, fibrosis; mostly affecting both fiber types, may be limited to type II fibers -Focal or diffuse loss of thick myosin filaments -Scattered to more prominent myonecrosis, vacuolization, and phagocytosis of muscle fibers 	

Table 6 - Signs and histological differences between CIM and CIP. Information compiled from: Friedrich, Reid et al. (2015)

Although, as previously stated, it is now established that septic patients more frequently suffer from both CIM and CIP, CIPM, than previously thought. CIPM presents itself as a combination of proximal greater than distal weakness, distal sensory loss, and variable atrophy. Less frequent histological signs of CIM/CIPM include acute necrosis, regeneration, and loss of myofibrillar ATPase staining affecting both type I and type II muscle fibers (Schefold, Bierbrauer et al. 2010). Additionally, CIM has been shown to precede CIP in patients with CIPM and occurs more frequently, whereas the additional CIP develops later and less frequently (Friedrich, Reid et al. 2015). Unfortunately, the subclassification of ICUAW in the ICU setting is a complicated task. Patients typically have co-morbidities and many tests rely on awake and willing patient participation which is usually hindered by impaired communication or sedation. Moreover, histology and electrophysiology tests are usually not obtained during the clinical routine (Schefold, Wollersheim et al. 2020). In relation to animal models, this makes it extremely difficult as many of the tests requiring patient participation cannot be completed on animals. Therefore, comparative studies must rely on different techniques to subclassify ICUAW, such as histology, electron microscopy, and western blotting which require the sacrifice of the animal (Owen, Patel et al. 2019).

1.4.6 Animal models outside of sepsis to investigate specific mechanisms which contribute to muscle dysfunction and atrophy

While studying muscle wasting in patients or sepsis animal models does give rise to important data relating to the unique way in which sepsis induces muscle wasting, it can be extremely difficult to separate the underlying cause due to the many variables at play in the ICU and a person or animals response to a septic insult. Therefore, researchers have employed a sundry of injury, ICU, and genetic animal models to understand the actual cause of muscle dysfunction (Friedrich, Reid et al. 2015). One popular and well characterized genetic model is the Duchenne muscular dystrophy (DMD) mouse (MDX). Due to a point mutation at the DMD gene, MDX mice produce small non-functional dystrophin proteins, which results in the classical appearance of fragmented NMJs and a large increase in fibrosis (McGreevy, Hakim et al. 2015). Another model using partial sciatic nerve removal with/without systemic administration of corticosteroids was established to mimic the situation in patients given systemic neuromuscular blocking agents in conjunction with high-dose corticosteroids to treat asthma and chronic obstructive pulmonary disease (COPD) as these patients developed classical CIM. Here, they

found that stimulation of the denervated muscle prevented the upregulation of extra-junctional AChRs and prevented depolarization of the resting potential, suggesting that some properties of muscle are primarily regulated by action potentials rather than chemical trophic influences (Friedrich, Reid et al. 2015). Although, it is important to note that denervation does not identically mimic immobilized patients, as the nerve is still attached in these patients. Additionally, Khan et al. (2016) points out, sympathetic input to skeletal muscle travels via the sciatic nerve, therefore, sciatic denervation atrophy models, as this one, may also have a sympathetic contribution. This idea is reinforced by the fact ganglionic or chemical sympathectomy increases proteolysis in rat muscles, upregulates MuRF1, and downregulates postsynaptic AChR (Khan, Lustrino et al. 2016, Rodrigues, Messi et al. 2019). While treatment with norepinephrine reduced mRNA levels of atrogenes MAFbx (atrogin-1), MuRF1, and myogenin (Silveira, Gonçalves et al. 2014). Moreover, Straka et al. (2021) found that chemical sympathectomy caused an increase in Rab5, a key regulator of endosome fusion and trafficking, and Cdk5, shown to regulate Rab5, thus reflecting an upregulation of endocytic and lysosomal pathways. In addition, it was also found that neural cell adhesion molecule (NCAM) was upregulated, which is a solid indication of denervation.

Although sympathetic innervation has been shown to be crucial for the function and maintenance of NMJs (Khan, Lustrino et al. 2016) as well as having a roll in modulating the immune system (Ferreira and Bissell 2018), there is a scarce amount of research up to this point regarding sepsis. However, a few studies have pointed towards the benefits of addressing the sympathetic nervous system (SNS) during a septic state, with increasing evidence that there is a systemic degradation of the SNS. Indeed, Hoover et al. (2017) demonstrates that end stage septic patients lacked tyrosine hydroxylase (TH), a specific noradrenergic marker, positive nerve fibers in the spleen, with an average abundance of only 16% compared to the controls. They also show evidence for direct sympathetic innervation of leukocytes and hypothesize that this nerve loss may not be limited to the spleen and could impair neuroimmunomodulation. Fittingly, Latronico et al. (2013) and Skorna et al. (2015) have both demonstrated that skin biopsies from critically ill patients indicate that small sympathetic and C-fibers also undergo degradation throughout the course of the disease and may explain why patients with CIP sometimes show typical symptoms of small fibre neuropathy in the subacute and chronic phase following critical illness (Schefold, Wollersheim et al. 2020). Thus, solidifying the notion that sympathetic innervation loss is not confined to any specific compartment and is most likely a systemic loss, including skeletal muscle. While there is no direct evidence of SNS degradation in muscle tissue, indirect evidence does allude to the notion that this, in fact, the case. Using the CLP model of sepsis, Piriz et al. (2008) and Ito et al. (2006) demonstrated that treating septic mice with salbutamol or terbutaline, β_2 adrenergic receptor agonists, respectively, improved diaphragm force generation and decreased dysfunction after sepsis. Although unfortunately they do not give any rationale why this may be the case and only included data regarding force output. Though, this could point toward a loss of sympathetic tone in the diaphragm which is alleviated with the treatment of a sympathetic agonist. Moreover, their results closely mimic the case of a chemical sympathectomy which is also reversed using clenbuterol, another β_2 agonist (Khan, Lustrino et al. 2016). Furthermore, sympathectomy is associated with increased mRNA expression levels of pro-inflammatory cytokines while mRNA expression of anti-inflammatory cytokine IL-10 is decreased, suggesting that the SNS can play a role in both pro-inflammatory inhibition and anti-inflammatory expression. Moreover, high concentrations of norepinephrine, via β adrenoceptors, has been shown to inhibit phagocytosis, NK cell activity, MHC class II expression, and secretion of TNF, IL-12, and IFN- γ from macrophages or lymphocytes (Wei, Liang et al. 2020). Thus, indicating that the loss of SNS innervation during sepsis could not only be detrimental to muscle but may also

be partially responsible for the lack of anti-inflammatory mediators late into the illness and sustained increases in pro-inflammatory cytokines

2. Aims of the study

The overall aims of this research can be broken down into three main goals:

- i) Due to the general absence of applicable TOC methods for the evaluation of muscle tissue in a whole mount context, the first goal of this project was to establish and validate a TOC protocol which allows for this type of analysis in a septic context as well as being compatible with our available microscopes and BGT, the most widely used post-synaptic NMJ marker. Moreover, the established method should be optimized for compatibility with newer and faster imaging techniques, such as LSM, and permit the analysis of multi-stained tissue. Lastly, this protocol should be evaluated for its clearing capacity in relation to tissues other than muscle for whole mount analysis.
- ii) The second goal of this project was to establish a septic mouse model based on the cecal slurry model of sepsis which would be severe enough to investigate sepsis induced muscular alterations. After successful establishment, the model should be characterized to determine if risk factors associated with sepsis, such as hyperglycaemia, increases in specific cytokines, and CIM are manifested. Further evaluation should then be completed to ascertain if our model reflected the classical alterations to muscle and of specific pathways due to sepsis, including a reduction in diaphragm width, fiber diameter, and any upregulation of the UPS pathway.
- iii) The third and final goal of this project was to determine if CIP manifests in our model and its effects on the SNS innervation of muscle. Since we initially assumed sepsis causes a loss of this SNS innervation, this in turn, could have detrimental implications in the loss of muscle mass in a muscle atrophy and wasting context. Thereby, drastically impacting patient's quality of life after sepsis.

3. Material and Methods

Animals

For the current study, male C57/BL6, C57BL/10J, and BL10/JMDX were used. For all cecal slurry experiments (C57/BL6), mice were purchased from Janvier at 10 weeks of age and were allowed to acclimate for no less than 14 days at the Universitätsklinikum Mannheim animal facility. All mice were maintained in PIV cages, with a maximum of 5 mice per cage, in a controlled environment, and given free access to drinking water and chow. Mice were then moved to an isolated S2 lab no less than 24 hours prior to the start of each experimental run, placed on a lab bench for camera monitoring, and given additional wet food throughout. For tissue clearing experiments (C57BL/10J and BL10/JMDX), mice were maintained at Karlsruher Institut für Technologie animal facility, with either whole hind limbs or just EDL muscles as well as diaphragm muscles freshly dissected, immediately immersed in 4% PFA/1x PBS, or various concentrations of acrylamide, bis-acrylamide, and VA-044 and incubated for a minimum of 24 hours or 5 days, respectively, on a roller mixer at 4°C. All procedures were approved by the animal ethics committee (authorization #: 35-9185.81/G-132/17) at Universitätsklinikum Mannheim as well as Karlsruher Institut für Technologie and in accordance with the German authorities EC directive 2010/63.

Cecal slurry stock preparation

The cecal slurry stock solution was prepared as previously described by Starr et al. (2014). Briefly, 4 month old C57/BL6 donor mice were anesthetized with isoflurane and sacrificed by cervical dislocation. The whole cecum was then dissected from each mouse and the entire cecal contents collected using sterile forceps. The collected contents were combined, weighed, and thoroughly mixed with sterile water at a ratio of 0.5 ml water per 100 mg cecal matter. This solution was filtered through an 860 µm (Bellco Glass, 1985-00020), 190 µm (Bellco Glass, 1985-00080), and 70 µm (Bellco Glass, 1985-00200) sterile mesh screen using an 85 ml homogenizer pan (Bellco Glass, 1985-85000). An equal volume of 30 % glycerol (Kraft, 07091.3000) in phosphate buffered saline (PBS) (Gibco, 10010056) was added to the filtered CS stock solution for a final concentration of 15 % glycerol. The final CS stock solution was then continuously stirred, aliquoted in cryovials (Greiner Bio-One 122278), and stored at -80 °C.

Induction of sepsis

Frozen CS stock solutions were thawed for 30 minutes prior to injection at 37 °C. After mixing thoroughly, mice were briefly anesthetized with isoflurane (Abbott B506) and the CS stock solution injected intraperitoneally (i.p.) with the use of a 30-gauge (G) needle. A subcutaneous injection of 0.1 mg/kg Temgesic® buprenorphine was also given at this time and every 8 hours thereafter, as well as 0.3 mg/ml added to the drinking water for pain management. Mice were then monitored for up to 7 days and the severity of sepsis assessed via body weight, body temperature (IR camera), movement, and MSS. A lethal dose for the CS stock used in this study was found to be 200 µl, with a 90% mortality rate after 48 hours and 100% at 53 hours (n=10). Therefore, unless specified to be different, 200 µl was administered for the initial induction of sepsis for all groups.

Antibiotics and fluids treatment

This study closely followed Steele et al. (2017) antibiotics and fluids regimen with some modifications depending on group. Briefly, imipenem (IPM) was reconstituted in sterile physiological saline (Braun 9511711) and mixed until no visible particles were found, for a final concentration of 0.005 mg/ml. IPM was then aliquoted and stored at -20 °C for up to 1 week as Steele et al. (2017) found IPM maintained a 95% efficacy under these storage conditions. For injections, aliquots were fully thawed, mixed well, and 1.5 mg (300 µl) given subcutaneously (s.c.), in addition to 700 µl of sterile physiological saline. Injections were administered starting 10 hours post induction of sepsis and every 12 or 16 hours thereafter, depending on the group. Intervention with antibiotics and fluids were then stopped when mice received a score of 5 or lower on the MSS scale, which usually occurred around day 5.

Bacterial load

To assess blood bacterial load, mice were anesthetized with isoflurane and blood samples taken from the retrobulbar venous plexus. 10 µl of the collected whole blood was diluted in 90 µl of sterile saline and mixed well. Then, 10 µl of the diluted solution was plated onto blood agar plates containing 3.7% w/v brain-heart infusion broth and 1.5% w/v agar in duplicates. After blood sampling, mice were promptly sacrificed and their spleen and liver collected. For organ bacterial load assessment, a portion of each spleen and liver was taken, weighed, pushed through a 70 µm cell strainer (Falcon 352350) for homogenization, and diluted in a ratio of 1 ml sterile saline per 100 mg of tissue. After mixing, 10 µl of this solution was further diluted into 90 µl of sterile saline. 10 µl of the final solution was then plated in the same manner as the blood, with all steps completed under a sterile environment. All plates were incubated at 37 °C for 24 ± 2 hours, the bacterial colonies counted, and CFU calculated.

Plasma values

Lactate, glucose, alanine aminotransferase (ALT), aspartate aminotransferase (AST), urea, creatinine, and bilirubin plasma levels were measured following Zentrum für Medizinische Forschung (ZMF), Medical Faculty Mannheim, guidelines. Briefly, blood was collected from the retroorbital venous plexus of anesthetized mice and placed directly into Lithium-Heparin vials (Sarstedt 20.1345) and kept on ice throughout the procedure. These vials were mixed and then centrifuged for five minutes at 4000 RPM. After, serum was collected in 0.5 ml eppies, stored at -20 °C and measured according to the manufacturer's instructions within two weeks of the collection date.

Cytokine measurements

Fresh blood was collected from the retrobulbar venous plexus of anesthetized mice and placed into EDTA collection tubes (Sarstedt 20.1341), centrifuged at 1000 relative central force (x g) for 10 minutes, the serum collected, and stored at -80 °C. Next, IFN-γ, IL-1α, IL-1β, IL-6, IL-10, and TNF-α were measured using a MILLIPLEX map Mouse Cytokine/Chemokine Magnetic Bead Panel (Cat# MCYTMAG-70K-PX32) on a MAGPIX® system, using xPONENT software version 4.2.1324.0, according to the manufacturer's instructions.

Infrared tracking

Mouse temperature and movement were monitored using a Flir A655sc infrared camera equipped with a 45° lens at a rate of 3 frames per second. For this, mouse cages were placed on the bench top of an S2 lab and the top cover removed from their PIV cages, leaving only the wire top. The camera was then mounted with a custom-built mount, Figure 24, directly over the top of the cage. Wet and pellet chow was added and moved to the bottom of the cage in order to not block the camera's field of view. Control data were collected for 48 - 24 hours prior to the start of each experimental group. After this period, the camera was left on and data were collected from the induction of sepsis until sacrifice for each group. Temperature data were collected, hand segmented every 16 hours, and analyzed using Flir ReaserchIR Max software version 4.40.9. Auto-tracking for mouse activity was based on Tungtur et al. (2017), with minor changes. Briefly, videos were exported from Flir ResearchIR Max as individual Tiff images and then opened in Fiji (ImageJ). Here, videos were converted to 8-bit, cropped, and cut into one hour segments. Next, a "Z project" for the average intensity was made and subtracted from the corresponding video to remove the background. After, a Gaussian Blur (size 4) was applied to remove the metal cage lines from the mice and a Yen threshold applied. Each video was then run through the wrMTrck plugin for auto-tracking with the following settings: minSize: 1500, maxSize: 8533, maxVelocity: 514, maxAreaChange: 100, minTrackLength: 3, bendThreshold: 0, binSize: 0, rawData: 0, bendDetect: 0, FPS: 3, backSub: 0, threshMode: Otsu, and fontSize: 16. Nightly activity levels were then calculated based on the first eight hours of nighttime activity.

Sepsis scoring

Mice were scored according to the murine sepsis score (MSS) system previously described by Shrum et al. (2014). Briefly, mice were scored 2, 4, 6, 8, and 10 hours post-insult and then every 8 hours based on their appearance, level of consciousness, activity, response to stimulus, eyes, respiration rate, and respiration quality on a 0 – 4 scale for each category, Table 7. If a mouse received a combined score of 21 or greater, or a four in any category, they were monitored closely for 24 hours. If no improvement was achieved during this time, they were removed from the experiment and euthanized via cervical dislocation due to animal ethics.

Variable	Score and description
Appearance	0- Coat is smooth
	1- Patches of hair piloerected
	2- Majority of back is piloerected
	3- Piloerection may or may not be present, mouse appears "puffy"
	4- Piloerection may or may not be present, mouse appears emaciated
Level of consciousness	0- Mouse is active
	1- Mouse is active but avoids standing upright
	2- Mouse activity is noticeably slowed. The mouse is still ambulant.
	3- Activity is impaired. Mouse only moves when provoked, movements have a tremor
	4- Activity severely impaired. Mouse remains stationary when provoked, with possible tremor
Activity	0- Normal amount of activity. Mouse is any of: eating, drinking, climbing, running, fighting
	1- Slightly suppressed activity. Mouse is moving around bottom of cage
	2- Suppressed activity. Mouse is stationary with occasional investigative movements
	3- No activity. Mouse is stationary
	4- No activity. Mouse experiencing tremors, particularly in the hind legs
Response to stimulus	0- Mouse responds immediately to auditory stimulus or touch
	1- Slow or no response to auditory stimulus; strong response to touch (moves to escape)
	2- No response to auditory stimulus; moderate response to touch (moves a few steps)
	3- No response to auditory stimulus; mild response to touch (no locomotion)
	4- No response to auditory stimulus. Little or no response to touch. Cannot right itself if pushed over
Eyes	0- Open
	1- Eyes not fully open, possibly with secretions
	2- Eyes at least half closed, possibly with secretions
	3- Eyes half closed or more, possibly with secretions
	4- Eyes closed or milky
Respiration rate	0- Normal, rapid mouse respiration
	1- Slightly decreased respiration (rate not quantifiable by eye)
	2- Moderately reduced respiration (rate at the upper range of quantifying by eye)
	3- Severely reduced respiration (rate easily countable by eye, 0.5 s between breaths)
	4- Extremely reduced respiration (> 1 s between breaths)
Respiration quality	0- Normal
	1- Brief periods of laboured breathing
	2- Laboured, no gasping
	3- Laboured with intermittent gasps
	4- Gasping

Table 7 - Assessing the septic state of mice based on the Murine Sepsis Score. A combined score of 0 – 8 = no or light impairment, 9 – 21 = moderate to severe impairment, and 22 – 28 = heavy impairment. Adapted from: Shrum et al. (2014)

Western Blot

Mice diaphragms were dissected immediately after sacrifice, placed in cryotubes (Greiner Bio-One 122278), flash frozen in liquid nitrogen, and stored at -80 °C. 500 µl of lysis buffer (840 µl of Tris-HCL [pH 7.4] 10 mM, NaCl [150 mM], EDTA [5 mM], TritonX-100 [1%], Sodium deoxycholate [0.5%], 150 µl protease inhibitor, 10 µl phosphatase inhibitor, and 1 µl DTT) were added to each diaphragm and lysed for 3 minutes at 30 Hz on a Qiagen TissueLyser. After, samples were centrifuged at 12 g for 10 minutes, the supernatant collected, aliquoted, and stored at -80 °C until needed. Protein concentration was then measured using a Millipore Direct Detect[®] spectrometer as well as a Bradford protein assay. Equal amounts of each sample, based on their protein concentration, were then placed in 2 ml Eppendorf tubes and 6 µl Ripa buffer (Thermo Scientific, 89901), 6 µl sample buffer (Invitrogen, NP0008), and 2 µl reducing agent (Invitrogen, NP0009) added. After, samples were mixed well, incubated at 65 °C for 10 minutes on a thermomixer, and then directly placed on ice to cool. Samples were then loaded into precast gels (Invitrogen, NP0321) and allowed to run for ~2 hours at 155 V. The gel was then removed and blotted using the Invitrogen iBlot[®] dry blotting system. After blotting, the membrane was blocked for 1 hour with freshly prepared 5% milk (Roth T145.3) and then rinsed 3x with 1x PBS (Gibco, 10010056). The membrane was then incubated with primary antibody overnight

in 1x PBS at 4 °C on a plate mixer. After incubation, the membrane was washed 3x with 1x PBS for 10 minutes per wash. Secondary antibody in 1x PBS was then added and allowed to incubate for two hours at room temperature (RT) on a roller mixer. After, the membrane was washed 3x with 1x PBS for 10 minutes per wash and imaged using a Vilber Lourmat Peqlab FUSION SL chemiluminescence imaging system. For Coomassie blue staining, gels were collected after blotting and incubated in Coomassie blue overnight on a plate mixer at 4 °C. Gels were then washed with de-staining buffer (40% ddH₂O, 50% Ethanol (70% Roth T913.3), and 10% Glacial acetic acid (Merk 1.00062.2500) and scans of each gel collected. For a detailed list of all primary and secondary antibodies used and their concentrations, see Table 8.

Western blotting primary and secondary antibodies			
Name	Dilution factor	Company	Cat. Number
Mouse anti-GAPDH	1:5000	GeneTex	GTX627408
Rabbit anti-MyBP-C	1:1000	Myomedix	MYBPC3
Mouse anti- α -Actinin	1:1000	Sigma-Aldrich	A7811
Chicken anti-MuRF1	1:1000	Myomedix	MuRF1-1y
Mouse anti-Multi Ubiquitin	1:2000	ENZO	BML-PW8810-100
Rabbit anti-ANKRD1	1:1000	Myomedix	Ankrd1
Rabbit anti-ANKRD2	1:1000	Myomedix	Ankrd2
Rabbit anti-Tyrosine hydroxylase	1:1000	Millipore	AB152
Rabbit anti-ADRB2	1:1000	Abcam	AB182136
Rabbit anti-Rab5	1:1000	Cell Signaling	3547
Rabbit anti-CDK5	1:1000	Santa Cruz	SC-173
Rabbit anti-NCAM1	1:1000	Cell Signaling	99746
β -actin (directly coupled HRP)	1:1000	Invitrogen	MA5-15739-HRP
Mouse anti- α -Tubulin	1:1000	GeneTex	GTX628802
Rabbit anti- α / β -Tubulin	1:1000	Cell Signaling	2148S
Rabbit anti-SMAD 2/3	1:1000	Cell Signaling	8685S
Rabbit anti-YAP	1:1000	Cell Signaling	14074S
Goat anti-rabbit-HRP	1:1000	Dako	P0448
Goat anti-mouse-HRP	1:1000	Dako	P0447
anti-chicken-HRP	1:500	Invitrogen	A16054

Table 8 - List of antibodies used for western blotting. HRP = horseradish peroxidase

Diaphragm width and fiber analysis

Diaphragms were freshly dissected and fixed in freshly prepared 4 % PFA for 30 minutes and washed overnight in 1x PTwH (1x PBS/0.5 % Tween-20 with 10 μ g/ml heparin) on a roller mixer at RT. Diaphragms were then cut into hemidiaphragms and blocked in Blocking and Permeabilization solution (BnP) (1x PBS/1x PTwH/0.5 % TritonX-100/10 % DMSO/6 % BSA) for 2 days at RT on a roller mixer. After 2 days, BnP was replaced with fresh solution and primary anti-neurofilament (SYSY, CAT#171002) was added at a dilution of 1:50 and mixed for 5 days at 37 °C. Hemidiaphragms were then washed for 2 days with solution changes every 2 hours for the first 6 hours and then every 5 hours thereafter using 1x PTwH at RT on a roller mixer. Next, samples were placed in fresh BnP solution, secondary anti-rabbit-Alex Fluor (AF)488 (Invitrogen, A32790) and α BGT-AF647 (Life Technologies, B35450) were added at a dilution of 1:200 and mixed for 5 days at 37 °C. Samples were then washed for 2 days in 1x PTwH with frequent solution changes as before at RT on a roller mixer. Lastly, samples were placed in 88 % Glycerol (RI 1.45) for a minimum of 24 hours and incubated at RT for refractive index matching. Diaphragms were then imaged in tile scan mode as detailed in the material and methods section “Microscopy”. After, tile scans of each hemidiaphragm were stitched in LAS-X and imported into FIJI (ImageJ). Each tile scan was then resliced and turned vertically to

visualize the depth (Z). Ten diaphragm width measurements were then taken by hand for each sample inside of the NMJ band region ($n = 3$) using the autofluorescence of the 488 or 555 channels, with the measurement collected using the Analyze > Measure tool within ImageJ. Using this same process, 100 hand segmented muscle fibers were also measured per mouse ($n = 3$).

MYOCLEAR

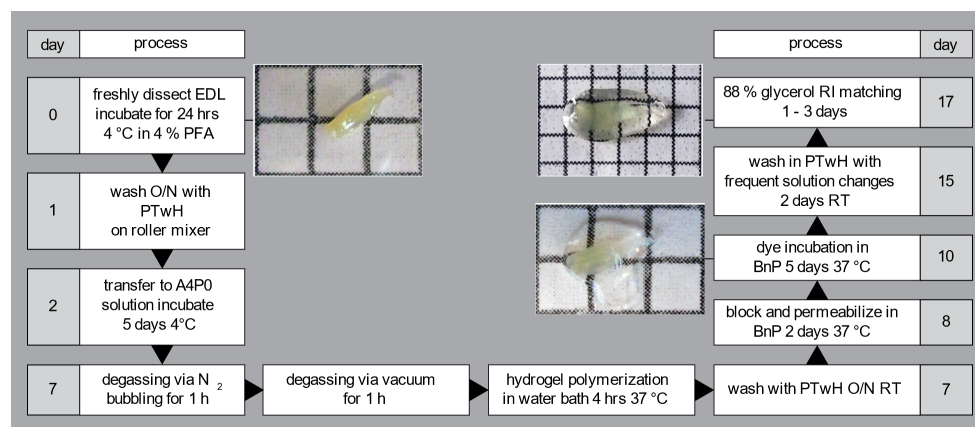


Figure 20 – Workflow of the MYOCLEAR protocol. This panel gives a graphical overview of the MYOCLEAR protocol, with the images next to processing days 0, 10, and 17 depicting representative EDL muscles at their respective time points.

Muscles were prepared following the MYOCLEAR protocol as shown in Figure 20. Briefly, samples were either freshly dissected or taken from 4 % PFA fixed mouse hind limbs. However, we recommend dissecting muscles from PFA fixed specimens since this tends to drastically reduce accidental damage to the tissue. Then, 100 mg of VA-044 (Wako 011-19365) initiator (final concentration 0.25 %) and 40 ml of freshly prepared hydrogel monomer solution (A4P0 (BIO-RAD 161-0140)) were added to 50 ml light resistant Falcon tubes, briefly hand mixed, and kept on ice to prevent premature polymerization. One muscle was then placed in each falcon tube and incubated on a roller mixer for 5 days at 4 °C. After, muscles were degassed for 1 hour via a custom-built degassing apparatus which allowed nitrogen to bubble over the samples, Figure 21(A). The caps of the Falcon tubes were then loosely placed back on and the tubes transferred to an airtight desiccator where they were vacuumed under a 90 kPa negative pressure for an additional hour in order to purge any remaining oxygen from the sample. The desiccator was then flushed with nitrogen, Falcon tube caps tightened, and placed in a hot water bath at 37 °C for 4 hours with shaking for polymerization. Samples were then removed from the Falcon tube and excess hydrogel removed by washing samples with 1x PTwH overnight on a roller mixer at RT. It is important to note that in lieu of using a desiccator and hot water bath, we found that using Life Canvas's EasyGel system resulted in comparable results and made sample handling simpler and easier. However, the custom-built nitrogen bubbling apparatus was still needed to ensure uniform hydrogel polymerization.

For NMJ plus nuclei labeling, samples were stained using a staining protocol inspired by iDISCO (Renier, Wu et al. 2014). For this, samples were washed in 1x PTwH with solution changes every hour for 2 h. After washing, samples were incubated in BnP with shaking at 37 °C for 48 hours. Then, the BnP solution was replaced with 1 ml of fresh BnP solution, the dyes added, and allowed to incubate for 5 days at 37 °C with shaking. After, samples were thoroughly washed in 1x PTwH with solution changes every 10, 15, 30 minutes, 1 hour, and then every 2 hours for a minimum of 2 days. The detergent was then removed by washing samples in distilled water for 4–8 h with frequent solution changes. Lastly, samples were incubated in 88% glycerol at room temperature for a minimum of 24 hours for RI matching and long-term storage.

Additionally, it was found that samples were stable for many months when stored in this manner. For indirect immunofluorescence staining, samples were processed as above, with additional washing and incubation steps for secondary antibody labeling. Here, after incubating in primary antibody for five days, samples were washed for two days in 1x PTwH on a roller mixer at RT, with frequent solution changes. Samples were then placed in fresh BnP, secondary antibody added, and incubated at 37 °C on a roller mixer for five days. Samples were then washed and prepared for imaging as described above. For a detailed list of all dyes, toxins, primary, and secondary antibodies, and their dilutions used for all microscopy experiments, see Table 9.

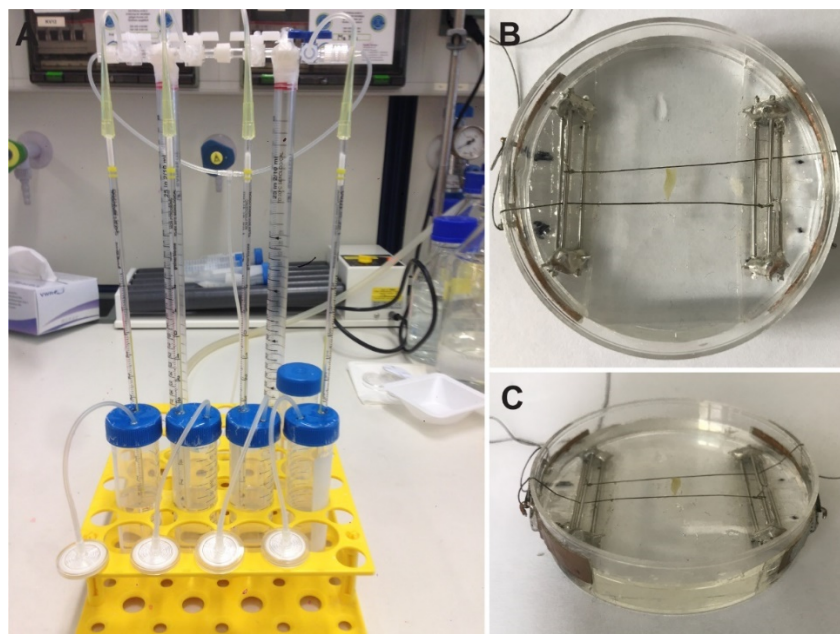


Figure 21 – Custom nitrogen bubbling chamber and mounting dish. (A) nitrogen bubbling chamber for degassing samples prior to polymerization, as well as a (B) top and (C) side view of the mounting dish used for MYOCLEAR processed EDLs.

X-Clarity

For all samples stained after active clearing, a Biozym X-CLARITY protocol was followed, excluding the perfusion step. This is available for download from their website, <https://www.biozym.com/>. Briefly, extensor digitorum longus (EDL) muscles were dissected from PFA fixed hind limbs and washed for 3 h in 1x PBS at 4 °C. Samples were then transferred to 50 ml light resistant falcon tubes containing 40 ml of freshly prepared 4 % PFA/A4P0 monomer solution and 100 mg of VA-044 initiator, followed by a 5-day incubation on a roller mixer at 4 °C. Then, samples were degassed via partial vacuum for 1 h, flushed with nitrogen, and incubated at 37 °C for 3 h in a hot water bath to induce polymerization. Afterwards, samples were washed for 1–2 hours in 1x PBS on a roller mixer at RT to remove excess hydrogel, transferred to an X-Clarity brain slice tissue holder, and lowered into the X-Clarity ETC chamber, where they were cleared for 3 hours with 4 % SDS buffer at a flow rate of 30 rpm; temperature: 37 °C; current: 1.5 A. After, samples were thoroughly washed in 1x PBST at 37 °C for 24 hours, then stored at 4 °C in 1x PBS. For staining, samples were processed following the immunostaining section described in the Biozym protocol, with a dilution factor of 1:200 and 1:500 for BGT-AF647 and Wheat Germ Agglutinin CF488 conjugate, respectively. Lastly, prepared samples were kept in 88% glycerol for storage and imaging.

Antibodies and dyes used for microscopy			
Name	Dilution factor	Company	Cat. Number
α -Bungarotoxin-AF647	1:200	Invitrogen	B35450
α -Bungarotoxin-AF555	1:200	Invitrogen	B35451
α -Bungarotoxin-AF488	1:200	Invitrogen	B13422
DRAQ5	1:300	Thermo Scientific	62251
WGA-CF488	1:500	Biotium	29022
Rabbit anti-collagen I	1:50	Rockland	600-401-103-0.5
Rabbit anti-vAChT	1:50	Synaptic Systems	139 103
Rabbit anti-troponin I	1:25	Cell Signaling	4002
Rabbit anti-dystrophin	1:50	MBL Int. Corp.	SM-3586-100
Rabbit anti-Neurofilament L	1:50	SYSY	171002
Goat anti-CD31	1:50	Bio-Techne	AF3628
CD169-AF647 (directly coupled)	1:100	BioLegend	142408
Rabbit anti-eMHC	1:50	Biorbyt	orb385438
Donkey anti-rabbit-AF647	1:200	Invitrogen	A21206
Donkey anti-mouse-AF488	1:200	Invitrogen	A21202
Mouse anti-rabbit PE-Cy7	1:200	Santa Cruz	SC-516721
Donkey anti-goat-AF546	1:200	Invitrogen	A11056

Table 9 - List of antibodies, toxins, and dyes used for microscopy. AF = Alexa Fluor, PE = Phycoerythrin, CF = Cyanine-based fluorescent dyes

3D Modeling and Printing

To avoid sample floating during the MYOCLEAR+ polymerization step, a mesh screen with a small hole to allow the nitrogen bubbling tube to reach the bottom of the falcon tube was modeled using Autodesk Inventor Professional 2019 and printed on an Ender 3 3D printer using polylactic acid (PLA) filament, Figure 23. In addition, we also printed a few sample holders using a resin printer. While this did increase the quality and ease of the print, we found the resin sample holders significantly more brittle when attempting to reuse them as done with PLA sample holders. Therefore, we recommend avoiding resin for printing. Though, other commonly used filaments for fused deposition modeling (FDM), such as polyethylene terephthalate glycol (PETG), could perform better than PLA, given its higher chemical and temperature resistance, durability, and flexibility.

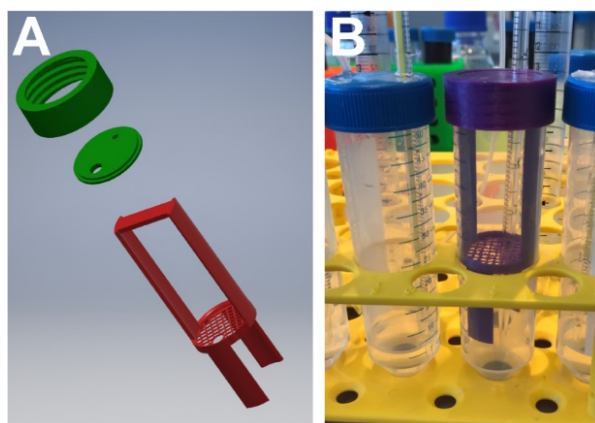


Figure 23 - 3D print model of sample holder. In order to keep sample from floating, a custom sample holder was modeled using Inventor professional and printed on an Ender 3. (A) depicts a 3D render of the sample holder, with (B) displaying the printed holder in PLA.

As no commercially available options were suitable for mounting the Flir A655sc infrared camera over the top of the mouse cages, a custom mount was modeled and printed in PLA in the same manner as before. Though, it is important to note that PLA is not the best option for

printing such structural parts, as the plastic threads were prone to breaking and were replaced with M6 x 50 bolts and locking nuts. Moreover, we would recommend using a stronger printing material for this type of print, such as PETG or Acrylonitrile butadiene styrene (ABS). Lastly, all .stl or the original .ipt files are freely available upon request.

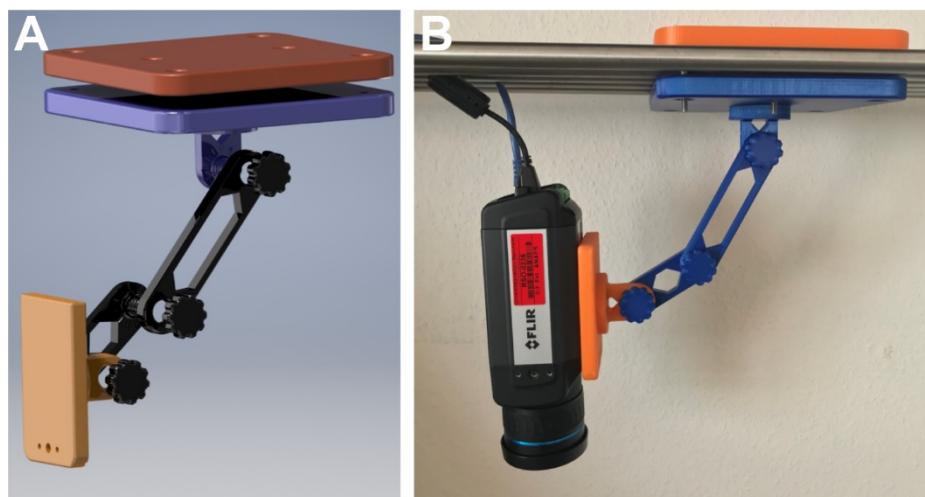


Figure 24 – 3D model and print of Infrared camera mounting system. (A) represents a 3D render of the (B) printed camera mount used to track temperature and activity variations of septic mice.

Microscopy

Single stack acquisitions were imaged using a Leica Microsystems TCS SP2 equipped with a Leica Microsystems HC PL AP0 20x/0.75 IMM CORE CS2 objective, Leica confocal software version 2.61, a KrAr laser (488 nm, 514 nm), a diode-pumped laser (561 nm), and a HeNe laser (633 nm). For mouse EDL tile scans, an upright Leica Microsystems TCS SP8 equipped with LAS-X software, a 488 nm laser, 561 nm laser, 633 nm laser, and Leica Microsystems clarity objective HC FLUOTAR L 25x/1.00 IMM ($n = 1.457$) was used. For diaphragm tile scans and light sheet acquired data, an inverted Leica Microsystems TCS SP8 DLS, equipped with LAS-X software (Version 3.5.2.18963), a 488 nm laser, 552 nm laser, 638 nm laser, and a Leica Microsystems HC PL AP0 20x/0.75 IMM CORE CS2 objective was used for all diaphragm imaging and an illumination 1.6x/0.05 DLS objective, detection HC APO L 10x/0.30 W DLS objective, and 7.8 mm TwinFlect mirrors were used for all light sheet acquired data. Depending on the experiment, refractive index matching and the imaging of whole mount muscle samples was performed in either 88% glycerol or DIMM (with and without the addition of urea). MYOCLEAR processed samples were mounted and imaged using a custom build imaging dish, Figure 21. For light sheet acquired data, muscles were mounted on thin strips of silicon by surgical thread knotted around the distal and proximal tendons. The silicon strip was then fixed to the bottom of a 6 cm glass bottom dish with a small amount of poster putty. Samples were then allowed to sit in the microscopy room for at least 24 hours in order to stabilize the temperature and prevent swirling in the mounting solution.

Image analysis, figure preparation, and statistics

After acquisition, all images were electronically processed using either Leica Microsystems LAS X core or ImageJ software. Signal-to-Noise-Ratio (SNR) and diaphragm width and fiber diameter measurements were done in ImageJ. For SNR, NMJs were segmented and mean intensities of the NMJs and standard deviation (SD) of adjacent fiber background regions were measured. The ratio of NMJ intensities vs. background SD was determined as SNR for each synapse. Numbers displayed in the text indicate the average of several SNR values per sample.

For diaphragm width and fiber analysis, tile scans of each hemidiaphragm were stitched in LAS-X and imported into FIJI (ImageJ). Each tile scan was then resliced and turned vertically to visualize the depth (Z). Ten diaphragm width measurements were then taken by hand for each sample inside of the NMJ band region ($n = 3$) using the autofluorescence of the 488 or 555 channels, with the measurement collected using the Analyze > Measure tool within ImageJ. Using this same process, 100 hand segmented muscle fibers were also measured per mouse ($n = 3$). For western blot data, the relative fluorescent intensity was measured using Vilber Lourmat Fusion software. Each intensity was then normalized to GAPDH and their ratio difference calculated based on their respective control levels. Bacterial load, plasma, cytokines, and activity levels were all analyzed using GraphPad Prism 8.0.1. For quantitative analysis of NMJ and fiber numbers, position of all observed NMJs / fibers was completed using the multi-point tool of ImageJ. This determined the xyz-position of the center of each NMJ / fiber. For analysis of critical morphological parameters of NMJs according to Jones et al. (2016), five square ROIs, each $500 \times 500 \mu\text{m}$, were selected per muscle. Then, all en face NMJs per ROI were manually thresholded and segmented using the magic wand tool in ImageJ. Then, area, perimeter and bounding rectangle diagonal were measured for every segmented NMJ. The number of AChR clusters per NMJs was counted manually. The diagonal of the bounding rectangle was calculated from the bounding rectangle sides while the fragmentation index was determined using the term: fragmentation index = $1 - [1/(\text{number of AChR clusters})]$. Spectral un-mixing (Zimmermann, Rietdorf et al. 2002) used the ImageJ plugin SpectralUnmixing (<https://imagej.nih.gov/ij/plugins/spectral-unmixing.html>). All figures were assembled using Adobe Illustrator. Mean values and standard deviations were calculated in Microsoft Excel and imported into GraphPad Prism 8.0.1 for statistical analysis. Normal distribution and homo/heteroscedasticity of data were probed using Kolmogorov-Smirnov test and F -test, respectively. According to these results and the type of data, statistical significance was evaluated using either one-way Analysis of Variance (ANOVA) with Tukey's *post-hoc* test, unpaired two-tailed t -test, or Kruskal-Wallis test. When appropriate, Turkey's multiple comparison test was added. Bar graphs are presented as mean \pm SD or ratio difference for western blot data. P -values were indicated as $*(p < 0.05)$, $** (p \leq 0.01)$, $*** (p \leq 0.001)$, or $**** (p \leq 0.0001)$. $P \geq 0.05$ was considered not significant.

4. Results

4.1 MYOCLEAR, a reliable SDS-free hydrogel-based clearing protocol which retains NMJ staining

Previous use of CLARITY based hydrogel embedding protocols for clearing whole skeletal muscles yielded decent tissue transparency, however, resulted in a quantitative loss of BGT fluorescence. To evaluate the possible causes for this, we tested several variations of the procedure that was previously described by Milgroom and Ralston (2016). Samples were PFA fixed, hydrogel embedded, and stained with BGT-AF647 for NMJ labeling. After, muscles were washed for two days, incubated in 88% glycerol overnight, and imaged to ensure a positive BGT-AF647 fluorescent signal, which all samples exhibited as shown in Figure 25(A). After imaging, samples were washed in PTwH for 24 hours at room temperature to remove glycerol and then actively cleared using Logos biosystems X-CLARITY tissue clearing system. Here, different electrophoresis strengths, the addition of PFA fixation after BGT-AF647 staining, as well as a passive CLARITY protocol using a constant flow of SDS with no current were tested. However, as depicted in Figure 25(A), these modifications resulted in a reduced Signal-to-Noise Ratio (SNR) of NMJ labeling in the cleared tissue. The PFA re-fixed samples were less affected but still exhibited a large decrease in fluorescence intensity of the BGT-AF647 staining and were still far from acceptable quality. Thus, supporting the findings of previous studies which state the incompatibility of CLARITY-based protocols with BGT-NMJ staining.

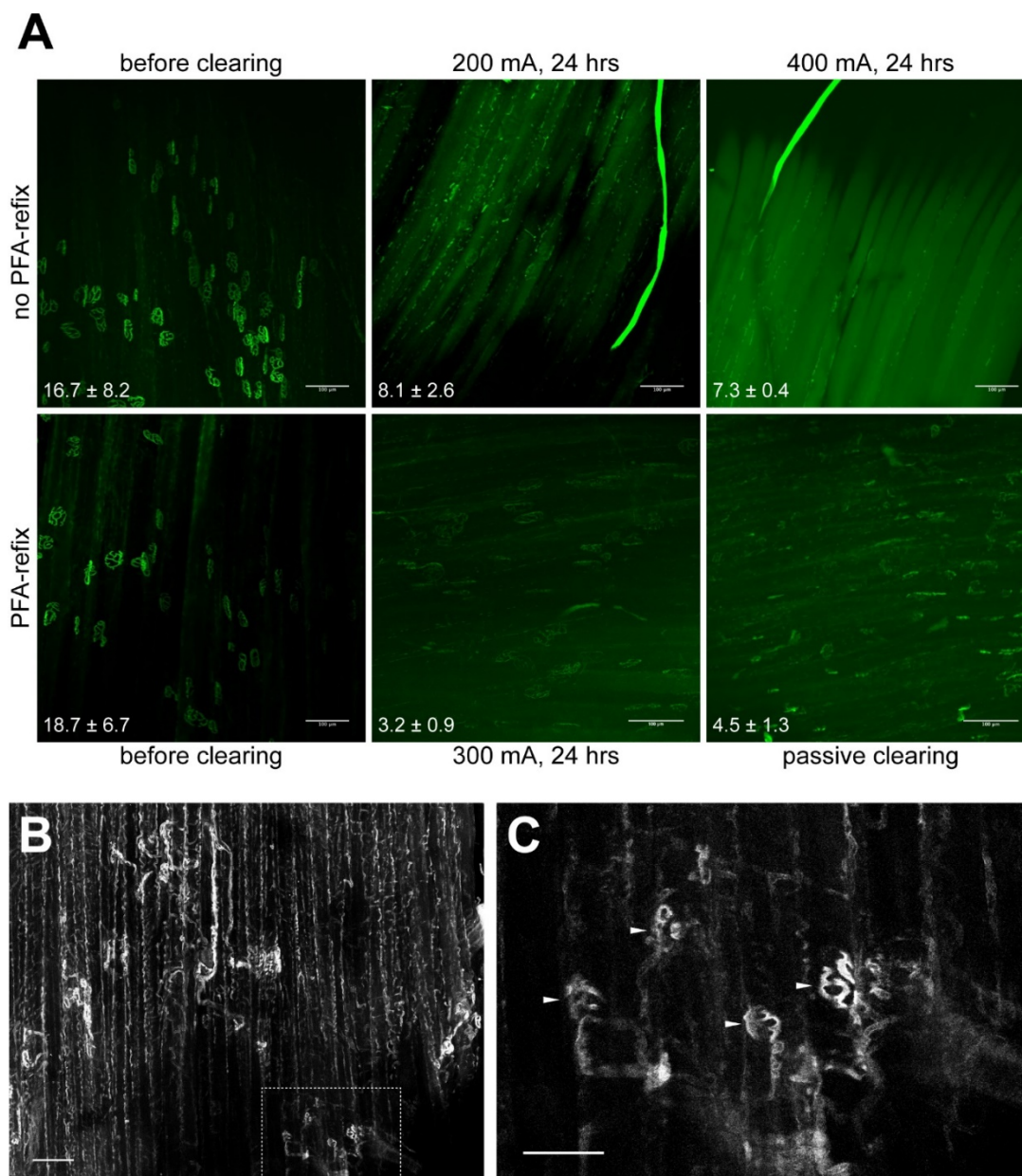


Figure 25 - Active and passive CLARITY-derived methods lead to a quantitative loss of BGT-AF647 staining but retain Lectin-mediated labelling of NMJ ECM. (A) EDL whole mounts were PFA fixed, embedded in hydrogel, and stained with BGT-AF647. After overnight incubation in 88 % glycerol, BGT-AF647 fluorescence was checked (before clearing). Then, glycerol was washed out via PTwH followed by different clearing procedures as indicated on the left. Finally, all samples were again equilibrated in 88 % glycerol and BGT-AF647 fluorescence was visualized (after clearing). Panels show maximum-z projections of confocal image stacks prepared on a Leica SP8. SNR \pm SD values are indicated on upper right angles of each panel. (B-C) EDL whole mounts were cleared using the X-CLARITY protocol and then stained with WGA-488. After overnight incubation in 88 % glycerol, WGA-488 fluorescence was measured. (A) Maximum-z projection of a representative confocal image stack prepared on a Leica SP8. Scale bar, 200 μ m. (B) Detail from the boxed region in A. Arrowheads, NMJs. Scale bar, 50 μ m. Source: Williams et al. (2019)

Next, we set out to determine the effects of SDS on BGT staining: whether it washed out the membrane bound AChRs, simply quenched the fluorophore, or denatured the AChRs to the point BGT would not be able to bind. Here, samples were processed following the X-CLARITY protocol. Briefly, samples were PFA fixed, hydrogel embedded, actively cleared using Logos biosystems X-CLARITY machine, stained with either WGA-488 or BGT-AF647, and incubated in 88% glycerol for imaging. Samples stained post-clearing with BGT-AF647 continued to result in an absence of NMJ signals, data not shown. However, shown in Figure 25(B and C), the proteoglycan-rich extracellular matrix (ECM) at the NMJs could be nicely identified alongside of other structures, such as blood vessels, in the samples stained with

WGA. Thus, indicating that NMJs in total were not destroyed by these techniques (see arrowheads in Figure 25(C)). Accordingly, it can be assumed that SDS either caused a quenching of the fluorophores or that it denatured the AChRs. The latter would, in turn, release BGT-AF647 from the AChR for samples stained before clearing or impede BGT-AF647 from binding altogether for samples stained post-clearing. With this in mind, SDS was excluded from all other experiments due to its role as a potential risk factor for the maintenance of BGT binding sites on NMJs.

With the recent introduction of a new free-of-acrylamide SDS based tissue clearing protocol (Xu, Tamadon et al. 2017), the necessity of the embedded hydrogel and its effect on tissue needed to be explored. In theory, the embedded hydrogel not only homogenizes the RI throughout the sample but also increases the porosity of it, resulting in better penetration and uniformity of the staining (Chung and Deisseroth 2013). To test the effects of the hydrogel, samples were PFA fixed and either embedded in hydrogel, then stained with BGT-AF647 or vice versa. Here, we found that samples stained after hydrogel embedding led to a better SNR and increased the overall imaging depth of the sample, as shown in Figure 26(A-G). This confirmed the need of embedding samples with hydrogel and resulted in the final protocol termed MYOCLEAR. This method represents a confocal microscopy compatible passive hydrogel-based clearing method for the visualization of NMJs in fixed mouse muscles and is summarized in Figure 20.

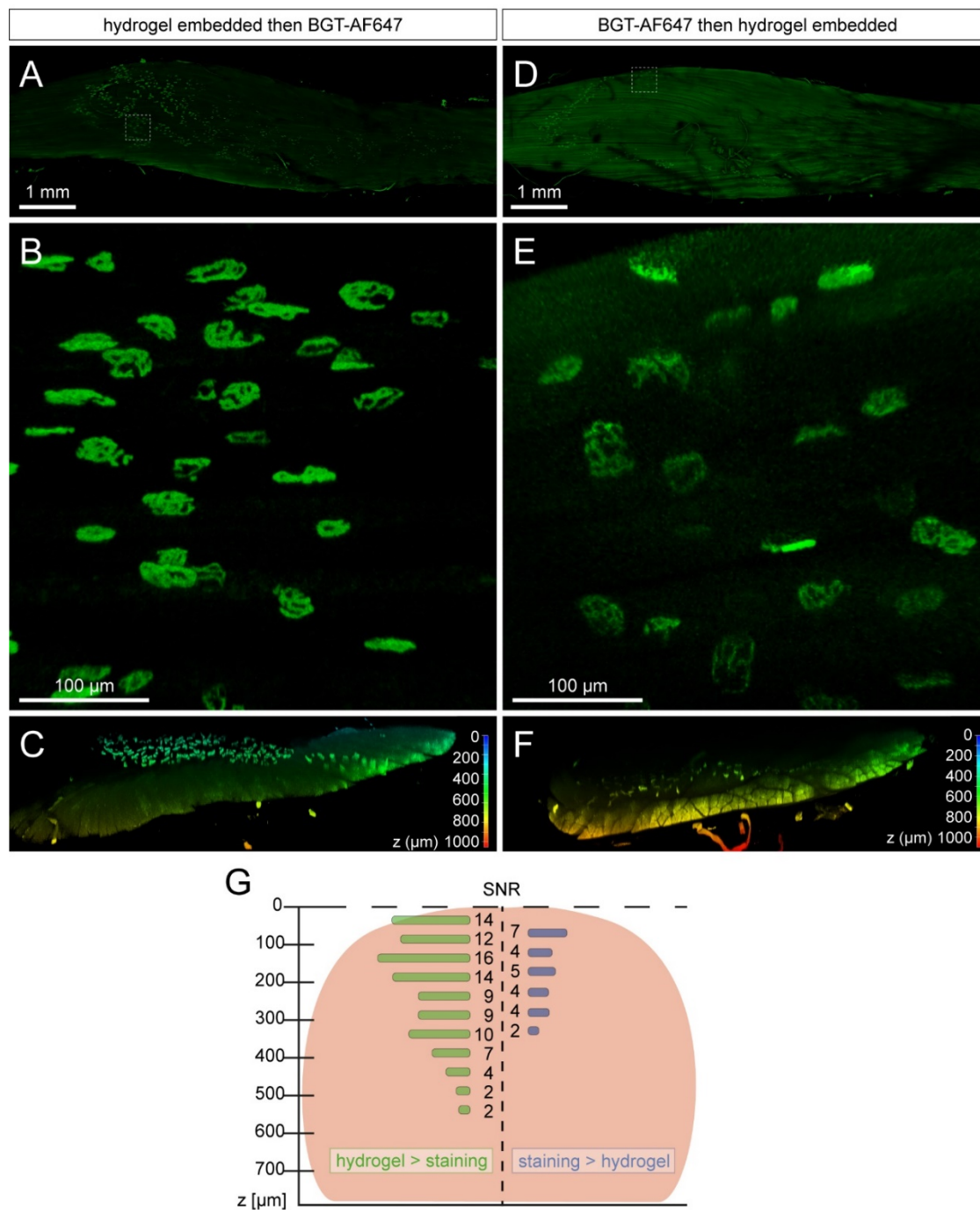


Figure 26 - Sequence of staining and hydrogel embedding affects overall imaging depth and quality of muscle samples. All samples were imaged in 3D using a Leica SP8 confocal microscope and images were processed with Leica LAS X software. (A–C) Mouse EDL muscle was PFA-fixed, hydrogel embedded, stained with BGT-AF647, and then RI matched in 88% glycerol before imaging. (D–F) Mouse EDL was PFA-fixed, stained with BGT-AF647, hydrogel embedded, and then RI matched in 88% glycerol before imaging. (A,D) depict overviews of the whole mouse EDL muscles with the boxed region representing zooms shown in (B,E). (C,F) portray cross sections cropped from the center of the EDL imaging data and depth-coded on the z-axis in order to visualize imaging depth and quality for both methods. (G) Graphical display of NMJ-signal SNRs in correspondence to muscle tissue depth and staining / clearing order. Muscle tissue extension in the central muscle region is depicted in the background as reddish round shape. Mean SNR values are shown as horizontal bars with corresponding numbers next to it. Left and right halves correspond to muscles shown in (C,F), respectively. Source: Williams et al. (2019)

4.1.1 Green/red autofluorescence and spectral unmixing of near-infrared fluorescence signals enable the visualization of muscle fibers, nuclei, and NMJs

Both detection of centro-nucleated fibers in diseased and regenerating muscle as well as analyzing the presence of fundamental subsynaptic nuclei at NMJs can be determined from the number and position of myonuclei and serve as relevant parameters in muscle research. Therefore, we set out to use Draq5, a near-infrared nuclear dye, in combination with a red-fluorescent BGT-AF555 conjugate on MYOCLEAR-treated EDL muscles. Depicted in Figure 27 in red, nuclei were well-stained and visible in the Draq5 channel. Conversely, NMJs, indicated by the arrowheads in Figure 27(B), were barely visible due to massive PFA-induced auto-fluorescence (both shown in green), thus rendering the quality of these results inadequate for analysis. Moreover, this intense level of auto-fluorescence was also observed in the 500-550 nm wavelength range when samples were stained with BGT-AF488, data not shown.

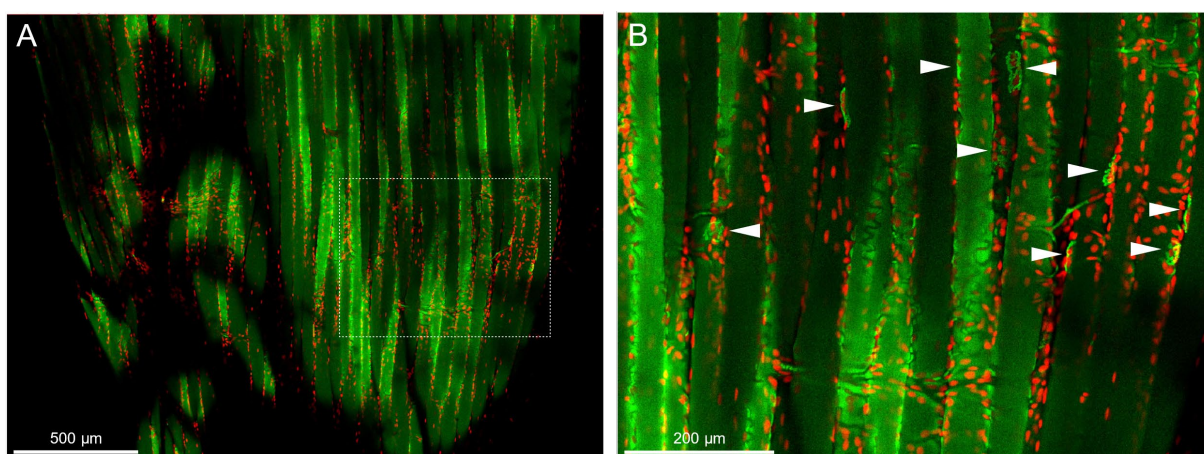


Figure 27 - MYOCLEAR enables imaging of muscle fibers and myonuclei by using red autofluorescence and far-red wavelengths dyes. Mouse EDL was processed via the MYOCLEAR protocol and stained with BGT-AF555 and Draq5. (A) depicts a confocal section of the EDL, with (B) representing a zoom of the boxed region. Strong autofluorescence of the tissue in the AF555 channel (green) resulted in a poor signal to noise ratio for NMJ detection (some NMJs are highlighted in B, arrowheads). In contrast, the near-infrared dye Draq5 displayed crisp and clear nuclei. Adapted from: Williams et al. (2019)

In order to help mitigate the auto-fluorescence induced limitation observed in the short wavelength fluorescence channels, we utilized two slightly spectrally separated near-infrared dyes, BGT-AF647 (maxima of excitation and emission, 650 and 665 nm, respectively) and Draq5 (maxima of excitation and emission, 646 and 681 nm, respectively). Muscles were PFA fixed, hydrogel embedded, co-stained with Draq5 and BGT-AF647, incubated in 88% glycerol, and imaged using a 633 nm wavelength excitation laser for both. Each dye was acquired separately, with their emission detection windows adjusted to 643-679 nm and 685-778 nm for BGT-AF647 and Draq5, respectively. Since the two dyes were only slightly separated, crosstalk between the channels had to be addressed by applying a spectral unmixing algorithm, with Figure 28(C and D) representing pre- and post-spectral unmixing, respectively. With this additional spectral unmixing step, nuclei as well as NMJs could be clearly distinguished and accurately segmented. A maximum Z-projection of a spectrally unmixed whole mount EDL with an overall imaging depth of 1.2 mm is shown in Figure 28(A), with Figure 28(B) representing a zoom-in of the boxed region in Figure 28(A). Depth-coded side views of BGT-AF647 and Draq5 can be seen in Figure 28(E and F) and reveal good signal penetration for both over a depth range around 1 mm. Figure 28(F) displays some elongated structures, which likely represent blood vessels traversing the muscle.

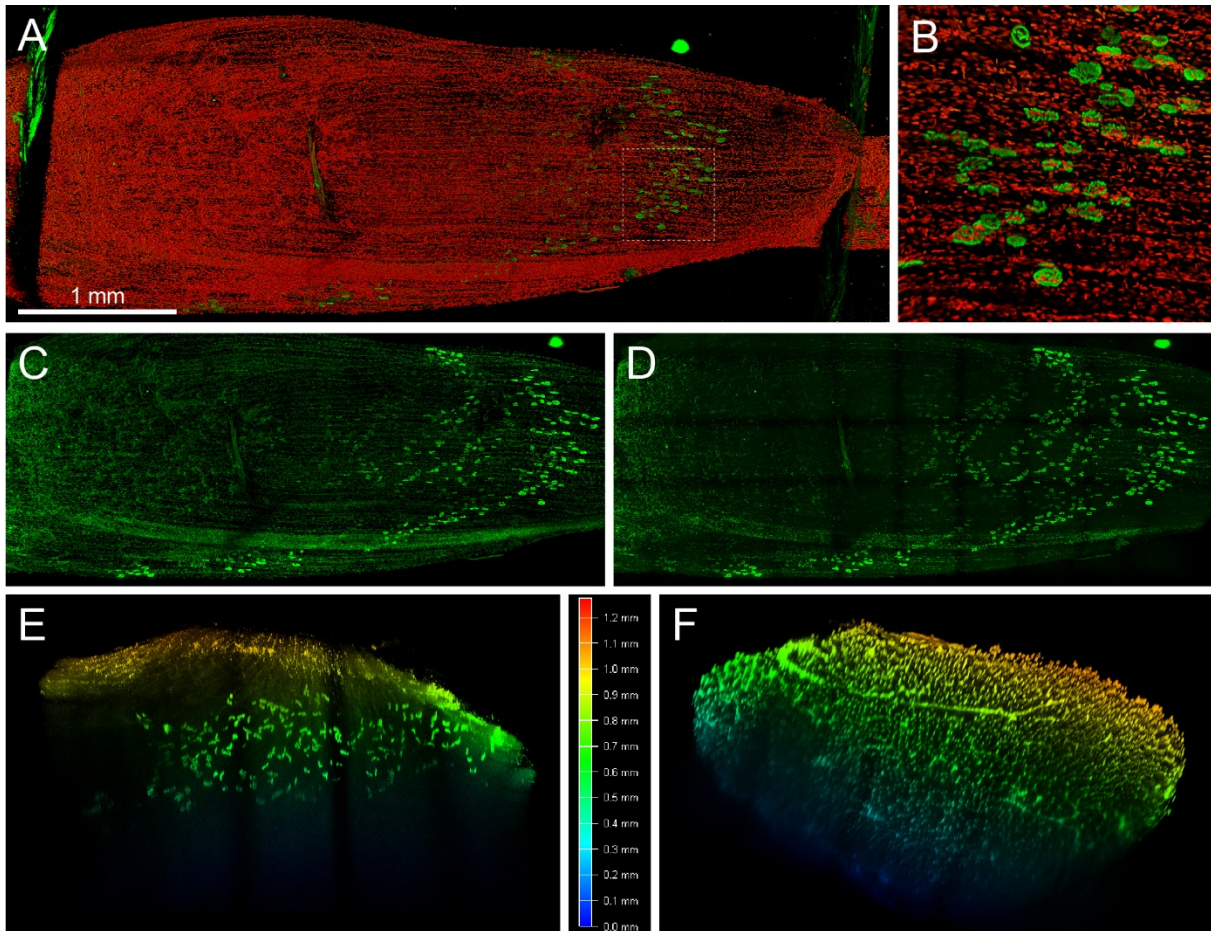


Figure 28 - Spectral un-mixing together with MYOCLEAR allows NMJ and nuclei whole-muscle imaging in near-infrared wavelengths. Mouse EDL muscle was processed via the MYOCLEAR protocol and stained with BGT-AF647 and Draqa5. In order to overcome the auto-fluorescence shown in Figure 27, the emission windows for each dye were adjusted according to their peak values and acquired separately using the same 633-nm excitation laser on a SP8 confocal microscope. The images were processed using Leica Las-X core software and spectrally un-mixed in ImageJ. (A) Maximum-z projection of the whole EDL before applying spectral un-mixing. Draqa5, red; BGT-AF647, green. Green autofluorescence of the thread keeping the muscle in place for imaging is visible at the proximal and distal ends of the muscle. (B) Zoom view of the boxed region in A. (C-D) BGT-647 channel data as shown in A before (C) and after (D) spectral un-mixing. (E-F) Z-axis depth coding for signals of BGT-AF647 (E) and Draqa5 (F) shown as cross sections after spectral un-mixing. Adapted from: Williams et al (2019)

To assess the compatibility of MYOCLEAR with muscles other than EDL, we applied the protocol to adult mouse diaphragm. As shown in Figure 29(A-D), confocal imaging revealed that the procedure was more than enough to achieve complete penetration of diaphragm muscle in Z. The insert in Figure 29(A) confirms that NMJs were well preserved in these samples, with any apparent fragmentation in the large overview due to nuclei partially covering many synapses.

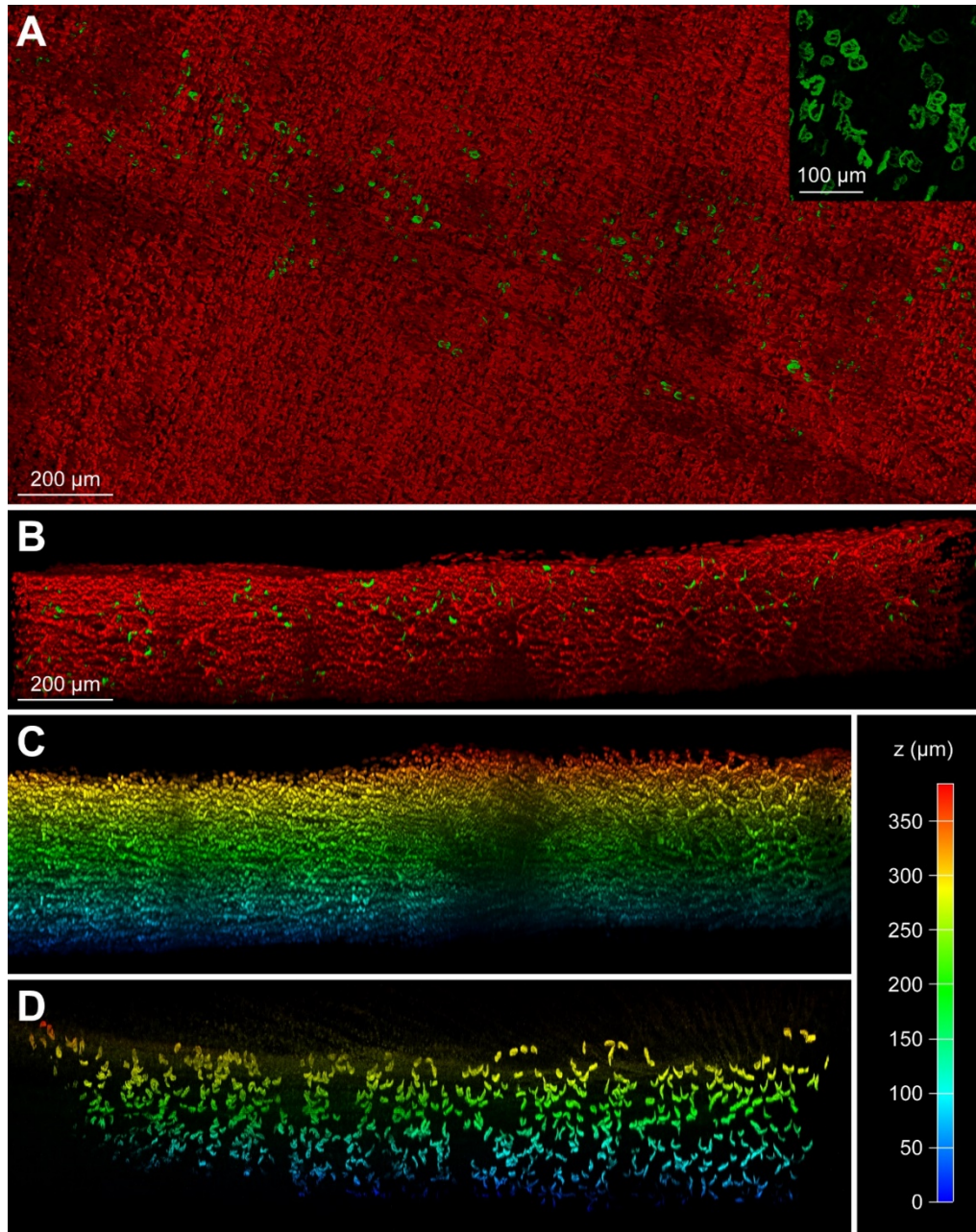


Figure 29 - MYOCLEAR is functional with adult mouse diaphragm muscle. Adult mouse diaphragm muscles were processed using the MYOCLEAR protocol and stained with Draq5 and BGT-AF647. (A) Maximum-z projection of a representative tile stack showing fluorescence signals of BGT and Draq5 in green and red, respectively. Note, that NMJs are not fragmented but partially covered by myonuclei. This is evident in the insert, which shows only BGT signals of a small region. (B) Side view to show depth extension of fluorescence signals. The entire depth of around 500 μm of the diaphragm became transparent. (C,D) Depth coded side views of nuclear (C) and NMJ signals (D). Pseudocolor code is explained on the right side. Source: Williams et al. (2019)

4.1.2 Whole mount analysis of MYOCLEAR processed MDX muscle allows for the detection of local NMJ fragmentation index heterogeneity

Wildtype skeletal muscle is characterized by an extremely homogeneous tissue composition. Opposed to this, diseased muscles can exhibit large amounts of fibrosis, fatty tissue, immune cell aggregates, or other changes that can affect the optical characteristics of muscle tissue and their transparency after clearing. Therefore, we examined muscles from wildtype as well as dystrophic Duchenne muscular dystrophy (MDX) mice, with the latter characterized by extensive fibrosis (Piñol-Jurado, Suárez-Calvet et al. 2018) and fragmented NMJs (Lyons and Slater 1991, Röder, Strack et al. 2012). After applying MYOCLEAR, we found that both

resulted in data of comparable quality, even with the extensive fibrosis found in MDX EDLs. Moreover, NMJ morphology was as expected and clearly different between the two; with wildtype NMJs displaying coherent pretzel-like structures and MDX NMJs demonstrating fragmented morphology. Therefore, additional whole mount imaging data were acquired for MYOCLEAR processed wildtype and MDX mouse EDLs stained with BGT-AF647. The number of visible NMJs were then quantified by hand using the multi-point tool in ImageJ. Figure 30(A and B) depicts representative muscles and illustrates the ability of this protocol to detect hundreds of NMJs. Quantitatively, 1082.3 ± 29.5 and 1019.5 ± 14.8 (mean \pm SD) NMJs were counted in wildtype and MDX muscles, respectively. A zoom-in of a few representative NMJs from each corresponding muscle can be seen in Figure 30(A' and B'). These panels demonstrate the normal, pretzel-like structure of wildtype NMJs (Figure 30(A')) in contrast to the fragmented appearance found in MDX muscle (Figure 30(B')).

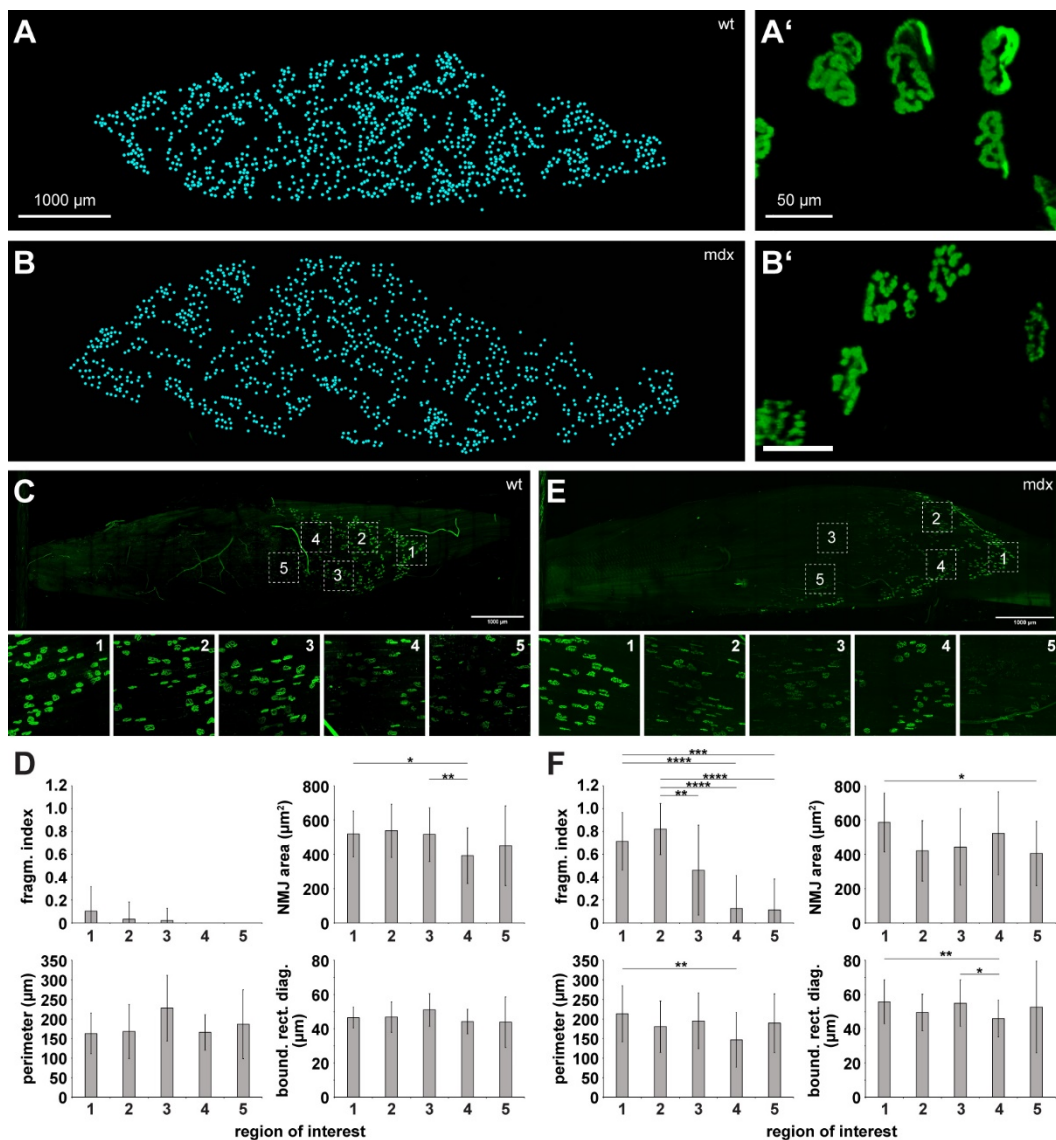


Figure 30 - Analysis of whole mount NMJ morphology and quantification of NMJ numbers is enabled in wildtype and MDX muscles upon clearing. EDL muscles from wildtype (A,A',C,D) and dystrophic MDX mice (B,B',E,F) were processed using the MYOCLEAR protocol and stained with BGT-AF647. (A,B) Maximum-z projections of all NMJs detected by hand segmentation. Each cyan spot represents a single NMJ. (A',B') High-power images of some representative NMJs from each muscle shown in (A,B). (C,E) Upper panels, maximum-z projections of representative muscles showing BGT-staining signals. Lower panels, high power display of ROIs 1–5 in corresponding upper panel. (D,F) Quantitative analysis of key morphological parameters: area, fragmentation index, perimeter, and bounding rectangle diagonal of NMJs. Depicted are mean \pm SD for all en face NMJs detected as a function of ROI number. * $p < 0.05$, ** $p \leq 0.01$, *** $p \leq 0.001$, **** $p \leq 0.0001$. Source: Williams et al. (2019)

When compared to individual tissue sections, one major advantage of whole mount imaging is the ability to better observe the overall heterogeneity of objects or effects of treatments within the entire organ. To evaluate if this held true for MYOCLEAR processed tissue, key morphological parameters of NMJs from different regions of interest (ROIs) of both wildtype and MDX muscles were determined and compared, based on a subset of criteria introduced by Jones et al. (2016). Shown in Figure 30(C-F), area, fragmentation index, perimeter, and bounding rectangle diagonal of NMJs from five different ROIs per muscle were analyzed. We found NMJ area, perimeter, and bounding rectangle diagonal were similar between all ROIs of a given muscle and apparently did not differ between wildtype and MDX. Conversely, NMJ fragmentation index was higher in MDX than wildtype and varied considerably within a given MDX EDL.

4.1.3 VACHT antibody staining confirms the integrity of the NMJ presynaptic apparatus upon MYOCLEAR

BGT-AF647 and lectin staining data suggested that the NMJ ECM and postsynaptic apparatus remained intact during MYOCLEAR processing. To address presynaptic integrity and the amenability of the clearing protocol for immunofluorescence staining, EDL muscles were processed with MYOCLEAR and stained with Draq5 for nuclei as well as an anti-vAChT antibody for the presynaptic NMJ marker protein vAChT. Shown in Figure 31(A), the obtained antibody staining was concentrated in NMJ regions, although considerable noisy signals were also observed outside the synaptic regions. Nevertheless, NMJ presynapses portrayed a normal coherent appearance. Thus, demonstrating this area was not affected by the clearing procedure. The general integrity of other major muscle compartments was also confirmed by additional immunostainings. As expected and depicted in Figure 31(B), dystrophin nicely outlined muscle fibers and was also enriched in NMJ regions. Further labeling with a collagen I antibody exhibited the distribution of large blood vessels, capillaries, and fascia cells (Figure 31(C)). Lastly, troponin I immunostaining displayed the regular pattern of sarcomeric striations, Figure 31(D).

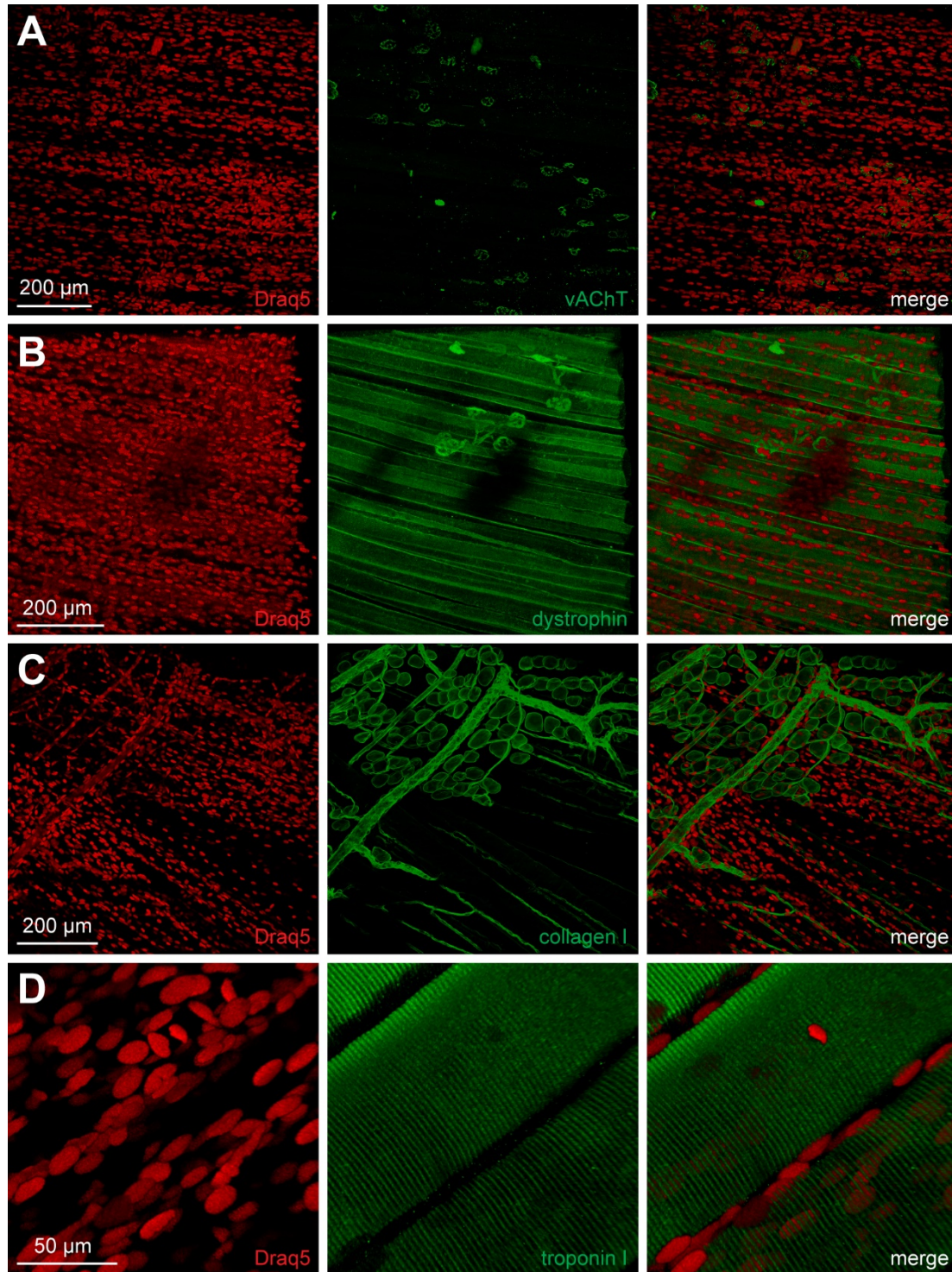


Figure 31 - Integrity of NMJ presynapse and other muscle structures is maintained upon clearing. Adult mouse EDL muscles were processed using the MYOCLEAR protocol and co-stained with Draq5 and antibodies against either NMJ presynapse (A, vAChT), sarcolemma (B, dystrophin), ECM (C, collagen I), or sarcomere (D, troponin I). Images show maximum-z projections of confocal z-stacks with an interplane interval of 2 μm and depths from muscle surface of 466, 665, 104, and 214 μm for (A–D), respectively. Source: Williams et al. (2019)

4.2 MYOCLEAR+ a PFA free hydrogel fixation protocol

It is well known various tissue fixation techniques, such as PFA and glutaraldehyde, introduce an increase in overall endogenous auto-fluorescence in tissue by the formation of Schiff's bases (Richardson and Lichtman 2015). This auto-fluorescence can be especially detrimental in the lower wavelength channels, 488 and 555, and indeed, was found to be one of the major pitfalls of the original MYOCLEAR protocol, Figure 27. Therefore, we opted to search for a PFA replacement to mitigate the induced auto-fluorescence seen in the lower wavelength channels, thereby recovering these channels for deep imaging, while simultaneously optimizing MYOCLEAR for light sheet microscopy.

Thus, we set out to determine if acrylamide or a combination of acrylamide and bis-acrylamide would be a suitable alternative to fix samples and not lead to tissue degradation. Mouse EDL muscles were incubated in either 4% acrylamide (A4P0B0) or 4% acrylamide/0.05% bis-acrylamide (A4P0B0.5) for five days. EDLs were then degassed, polymerized, washed overnight in 1x PTwH, and stained with an anti-mouse secondary antibody (488), BGT-AF555, and DRAQ5 to label blood vessels, NMJs, and nuclei, respectively. Depicted in Figure 32(A-F), it was found that fixing tissue with A4P0B0 led to sub-optimal tissue fixation, with nuclei displaying a blurry, smear like, appearance, as opposed to the crisp round shape found in normal PFA fixed tissue. However, samples that were fixed with A4P0B0.5 produced results comparable to PFA fixed tissue, resulting in crisp nuclei and structured blood vessels. Interestingly, BGT-AF647 was found to be comparable in both, with only a marginal improvement over fixing with just A4P0B0. In addition, fixing with just acrylamide mitigated the typical browning of tissue found in PFA fixed tissues, which is believed to be caused by mallard reactions (Frye, Degenhardt et al. 1998), Figure 32(G and H).

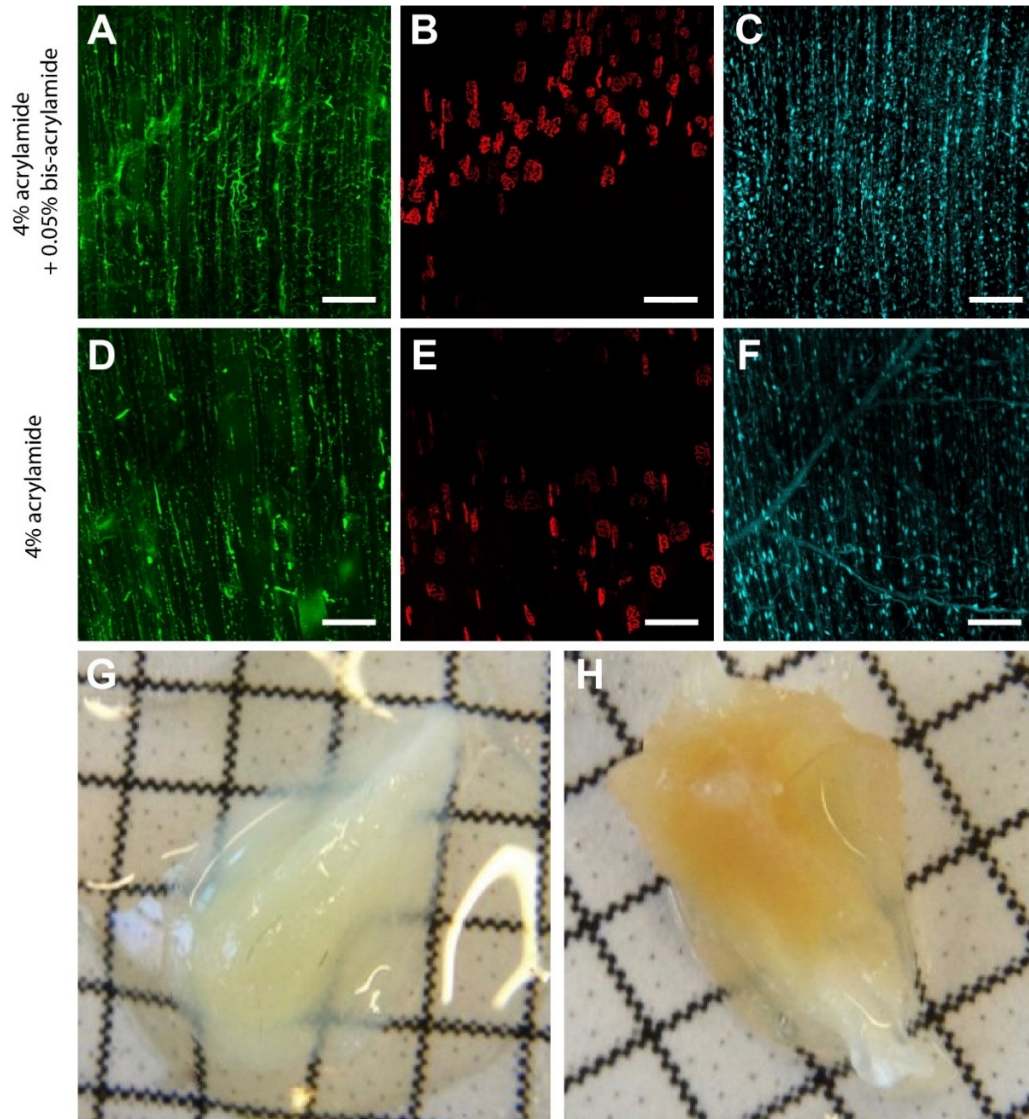


Figure 32 - Comparison of different acrylamide fixation techniques. A4P0B0.05 qualitatively displayed better retention of both blood vessels as well as nuclei when compared to A4P0B0 fixed samples. Freshly dissected adult mouse EDL muscles were incubated in either (A-C) 4% acrylamide, 0.05% bis-acrylamide, and 0.25% VA-044 activator (A4P0B0.05) or (D-F) 4% acrylamide and 0.25% VA-044 (A4P0B0) for five days at 4 °C on a roller mixer. Samples were then polymerized at 37 °C for four hours, washed overnight, blocked for two days with BnP, and stained with (A,D) mouse secondary antibody (488), (B,E) BGT-555, and (C,F) DRAQ5. n = 2, scale bar = 100 μm. In addition, mouse tibialis anterior muscles fixed with (G) A4P0B0.05 displayed considerably less fixation induced browning, when compared to (H) traditional PFA fixation.

Next, a more quantifiable approach needed to be performed to evaluate if A4P0B0.5 still presented protein degradation in compartments other than the ones analyzed with microscopy. This experiment also served to determine the optimal ratio of acrylamide/bis-acrylamide for tissue fixation. Mouse EDLs were incubated in various combinations of PFA, acrylamide, bis-acrylamide, and activator (as summarized in Figure 33) for five days. Samples were then degassed, polymerized, and washed overnight in 1x PTwH. After, the 1x PTwH was refreshed and the samples were placed on a roller mixer at room temperature. Aliquots of PTwH were taken from each sample on days 0, 1, 3, 5, 14, and 35 and a pierce 660 nm assay was used to detect any proteins that were present in the solution. However, as shown in Figure 33, even after 35 days, all samples were found to be under the limit of detection. Though, given the typical weight of an adult mouse EDL of roughly 15 mg and the limit of detection for the pierce 660 nm test is 125 μg/ml, it was calculated that over this time, samples presumably lost less than 0.83% of total protein content. Therefore, it was assumed that overall protein loss in

acrylamide/bis-acrylamide fixed samples was negligible and would, indeed, serve as a reliable alternative to PFA for tissue fixation.

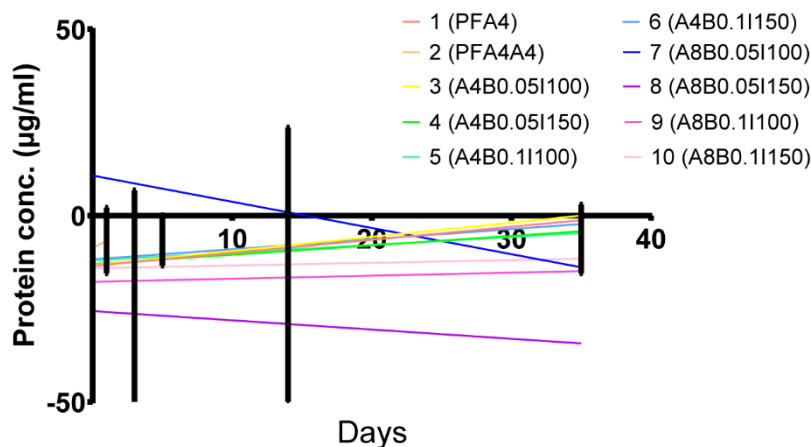


Figure 33 – Effects of various concentrations of PFA, acrylamide, bis-acrylamide, and activator on protein loss. Freshly dissected adult mouse EDL muscles were incubated for five days at 4 °C on a roller mixer in various concentrations of PFA, acrylamide, bis-acrylamide, and activator, as listed in the figure legend. Samples were then polymerized at 37 °C for four hours, washed overnight, and then placed in 2 ml eppies. 2 ml of 1x PtWH was then added to each and eppies put in light protected, brown falcon tubes. Samples were then kept on a roller mixer at room temperature. Aliquots were then taken at day 0, 1, 3, 5, 14, and 35 and analyzed using the pierce 660 nm protein assay. No matter the fixation conditions, no samples were above the LOD after 35 days. PFA = PFA (%), A = Acrylamide (%), B = Bis-acrylamide (%), and I = VA-044 (mg). n = 3 for all groups

In addition, it was found that increasing the amount of acrylamide/bis-acrylamide above the baseline concentration of 4% and 0.05% respectively, led to a stiff and brittle hydrogel. Whereas hydrogels using a concentration below this resulted in a very sticky and hard to handle hydrogel. Therefore, it was determined that A4P0B0.05 was the most optimal ratio and was used for all following experiments.

4.2.1 Optimization of acrylamide/bis-acrylamide tissue fixation

A major obstacle concerning fixing tissue with acrylamide is making sure each and every sample has been fully and homogeneously polymerized. If this is not obtained, tissue degradation, refractive index mismatches, and overall reproducibility become major concerns. Fortunately, it was found that the one hour of nitrogen bubbling and one hour of vacuum degassing before polymerization used by the original MYOCLEAR protocol was nearly sufficient to remove most of the oxygen from samples, with a few alterations. For MYOCLEAR+, samples were additionally placed on ice during the nitrogen bubbling step since it was observed to decrease the possibility of samples polymerizing earlier than desired. Moreover, instead of starting the polymerization process after one hour of vacuuming, polymerization was started 30 minutes into the vacuum step, then the vacuum left on for the remaining 30 minutes. This led to an overall reduction of the semi-polymerized top layer in the falcon tubes, contributing to a better and more robust polymerization when compared to the original protocol. Lastly, one highly unexpected observation was that freshly dissected samples which have undergone polymerization tend to float to the top of the falcon tube, unlike samples pre-fixed with PFA, which has the consequence of pushing samples into the aforementioned semi-polymerized top layer in the falcon tube. Therefore, sample holders were modeled using CAD software and 3D printed with polylactic acid (PLA), Figure 23, which greatly reduced the number of floating samples.

4.2.2 DIMM, a reliable glycerol replacement for refractive index matching and mounting

In regards to imaging, MOYCLEAR+ processed samples exhibited different characteristics when compared to PFA fixed, MYOCLEAR prepared samples. Unlike MYOCLEAR, acrylamide fixed samples exhibited an increase in light scattering, which was evident from its “milky” semi-translucent appearance in all wavelength channels for light sheet acquired images, Figure 34(A). Therefore, it was determined that using 88% glycerol was insufficient for homogenizing the light scatterers in acrylamide fixed samples. Initially, it was thought that this was due to the lipid content of the tissue. Therefore, the use of oil-based mounting solutions was investigated. MOYCLEAR+ processed mouse EDL muscles were placed in either standard confocal imaging oil, silicon oil, or mineral oil. Samples were then transferred to a roller mixer and checked daily for two weeks. However, it was found that acrylamide fixed samples did not mix well with any of the oils and, even after two weeks, resulted in a water/oil emulsion. Thus, making the imaging of these samples impossible. Though, samples were kept in the oil for an additional six months to determine if more time was needed for them to fully homogenize. However, after this time, the water and oil separated into two distinct layers and the size of the samples drastically decreased, presumably from dehydration. Therefore, it was determined oils would not be a suitable mounting solution replacement and a hyperhydrating solution should be investigated. Therefore, MYOCLEAR+ fixed samples were stained with DRAQ5 for nuclei and incubated in either 88% glycerol + 2 M urea or 88% glycerol alone for two days prior to imaging. Although it was found that the addition of 2 M urea did alleviate some of the light scattering, Figure 34, it was still not sufficient for deep imaging.

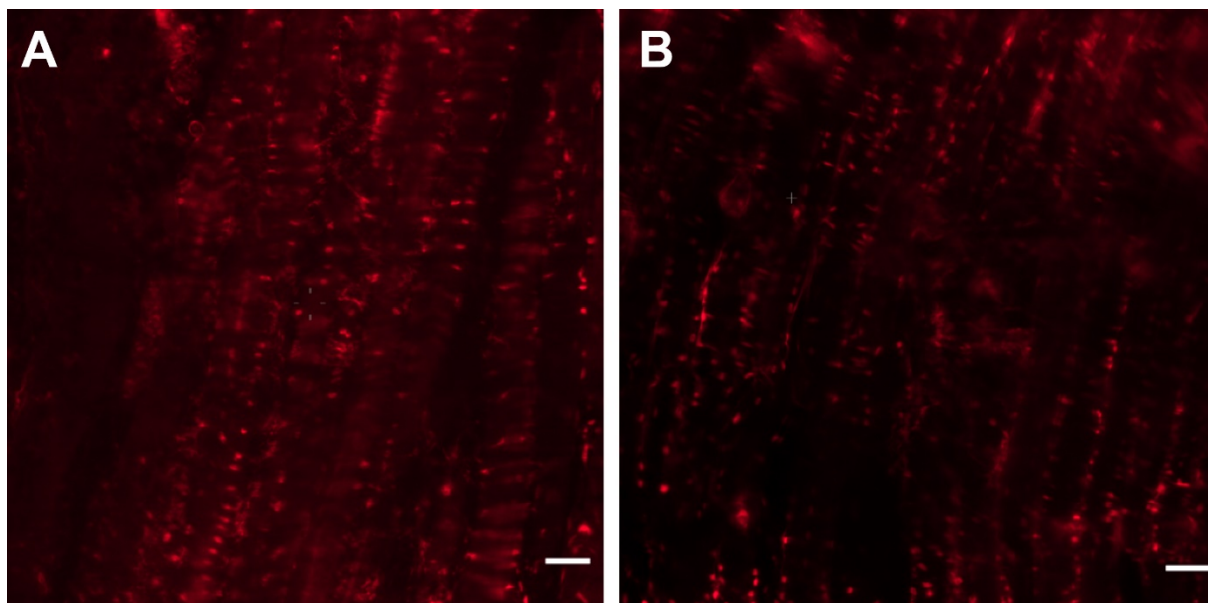


Figure 34 - Urea improves signal clarity in MYOCLEAR+ processed samples. Freshly dissected adult mouse EDL muscles were fixed and stained with DRAQ5 following the MYOCLEAR+ protocol. EDLs were then incubated in either (A) glycerol 88% or (B) 88% glycerol + 2 M urea for two days and imaged with light sheet using a Leica SP8 DLS microscope. (A,B) depict the quality and clarity differences muscles portrayed at an equal depth into the muscle. Scale bar = 50 μ m

After testing many other reagents in addition to urea, a revised, less viscous mounting solution termed Deep Imaging Mounting Media (DIMM) was created, which consisted of 3 M urea, 10% weight by volume (w/v) quadrol, 5% DMSO, 16% (w/v) sorbitol, and 40% glycerol ($n = 1.45$). To test this new solution, EDL mouse muscles were processed using MYOCLEAR+ and stained with neurofilament (NF-488), CD-31-AF546, and BGT-AF647 to label motor neurons, blood vessels, and NMJs, respectively. Samples were then allowed to incubate in DIMM for up to two weeks on a roller mixer at room temperature, with solution changes every third day, and imaged every other day to check for fluorescence. As shown in Figure 35, DIMM enabled light

sheet imaging depths of the lower wavelength channels comparable to near-infrared confocal acquired images processed using the original MYOCLEAR protocol. Though, it must be stated that while the imaging depth of CD-31-AF546 in the thinner section allowed for over 1 mm, the center of the thicker belly section only reached $\sim 600 \mu\text{m}$.

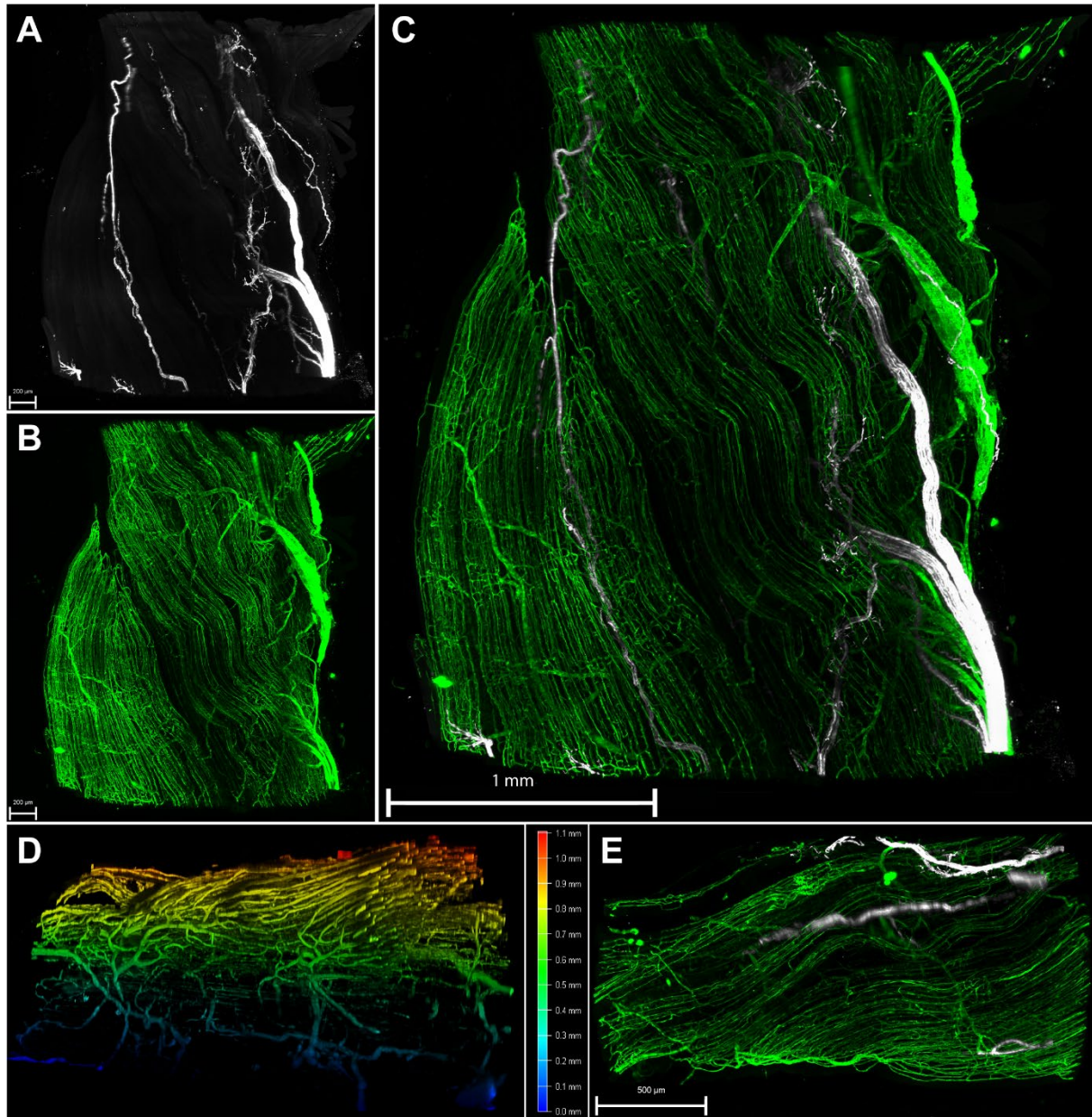


Figure 35 – MYOCLEAR+ with DIMM enable the use of the lower wavelength channels for light sheet acquisition. Freshly dissected adult mouse EDL muscles were fixed and stained with NF-488, CD-31-546, and BGT-647 following the MYOCLEAR+ protocol. EDLs were then incubated in DIMM for up to two weeks and imaged with light sheet using a Leica SP8 DLS microscope. (A-C) are representative images from the belly of the EDL, where (A) are motor neurons stained with NF-488, (B) are blood vessels stained with CD-31-546, and (C) is a merge of both channels. (D,E) are representative images of a distal, smaller section of the EDL with (D) depicting a depth view of NF-488 and CD-31-546 and (E) a merge of this section. Scale bar = (A,B) 200 μm , (C) 1 mm, (E) 500 μm

Moreover, as with SDS, DIMM resulted in a quantitative loss of BGT fluorescence in as little as 24 hours, no matter the conjugated fluorophore, data not shown. Though, pH as well as urea were identified as possible risk factors that could affect BGT binding (Momoji and Lennon 1984). Therefore, the pH of the original DIMM solution was adjusted using 37 % Hydrochloric Acid (HCL) to 7.4. Then, BGT-555 stained diaphragm samples were incubated for up to three days in either 88% glycerol, pH adjusted DIMM without urea, or with urea, and imaged, Figure

36(A-C, respectively). Here, we found that pH does, indeed, play a major role in the binding of BGT, with adjustments to pH able to retain BGT fluorescence. For testing urea, the pH adjusted DIMM solution was used and urea was either kept in or taken out of the final solution. Next, diaphragm samples were incubated in each solution overnight and imaged as before. Though, urea's role was found to not be as clear as the stark differences the pH data displayed. We found that BGT-555 signals were conserved in the absence and presence of urea, albeit at slightly diminished intensities with urea. Though, both solutions demonstrated the ability to image the complete depth of the diaphragm with little issue, Figure 36(D-E).

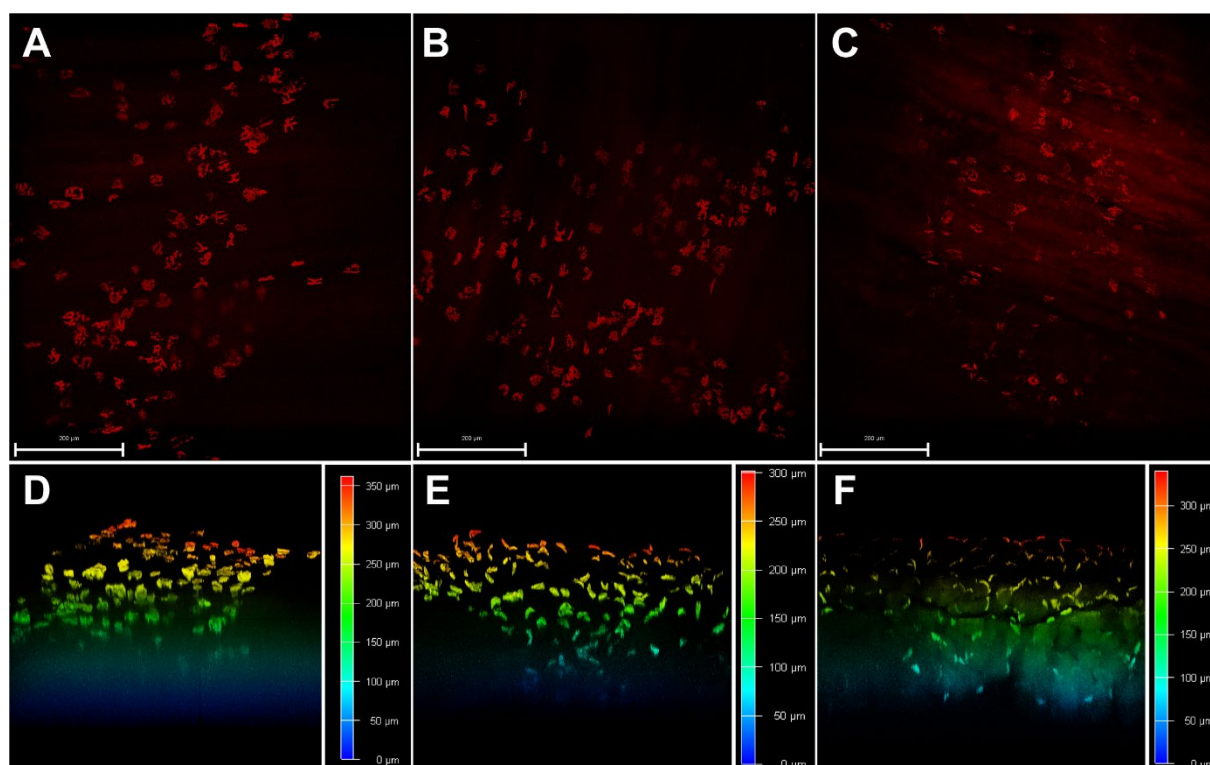


Figure 36 – Effects of pH and urea on the retention of BGT fluorescence. Adult mouse diaphragms were freshly dissected and fixed with 4% PFA for 5 minutes on a roller mixer at RT. Diaphragms were then cut into sections and stained with BGT-555 following the MYOCLEAR staining protocol. Each section was then incubated in either (A,D) 88% glycerol, (B,E) pH adjusted DIMM without urea, and (C,F) with urea. After 3 days, diaphragm sections were imaged with (A-C) depicting a top view as well as their corresponding depths (D-F). Scale bar = 200 µm

4.2.3 Application of MYOCLEAR+ to tissues other than muscle

In the past, many TOC methods were largely based on clearing more homogeneous tissues, such as the brain, when compared to the highly heterogeneous nature of skeletal muscle (Richardson and Lichtman 2015, Matryba, Kaczmarek et al. 2019). Therefore, we wanted to determine if MYOCLEAR+ was a viable alternative and compare its ability to render these more homogeneous tissues optically clear. For this, adult mouse brains were freshly dissected, fixed, and stained with NF-AF488 and CD-31-AF647 following the MYOCLEAR+ protocol. Samples were then incubated in the original DIMM solution for up to one week on a roller mixer at room temperature. After, the brain samples were cut down in order to fit between the TwinFlect mirrors and imaged using light sheet with a Leica SP8 DLS microscope. Here, we found that MYOCLEAR+ was more than able to clear brain tissues, with little issue imaging the full 1.5 mm Z depth range of our microscope, Figure 37. Though, we did find that the brain tissue was extremely fragile compared to other MYOCLEAR+ fixed tissues, which resulted in accidental damage with a pair of forceps, as indicated by the arrow heads in Figure 37. Yet, we

do believe MYOCLEAR+ to be a viable alternative to clear brain tissue if enough care is taken when mounting the sample to avoid accidental damage.

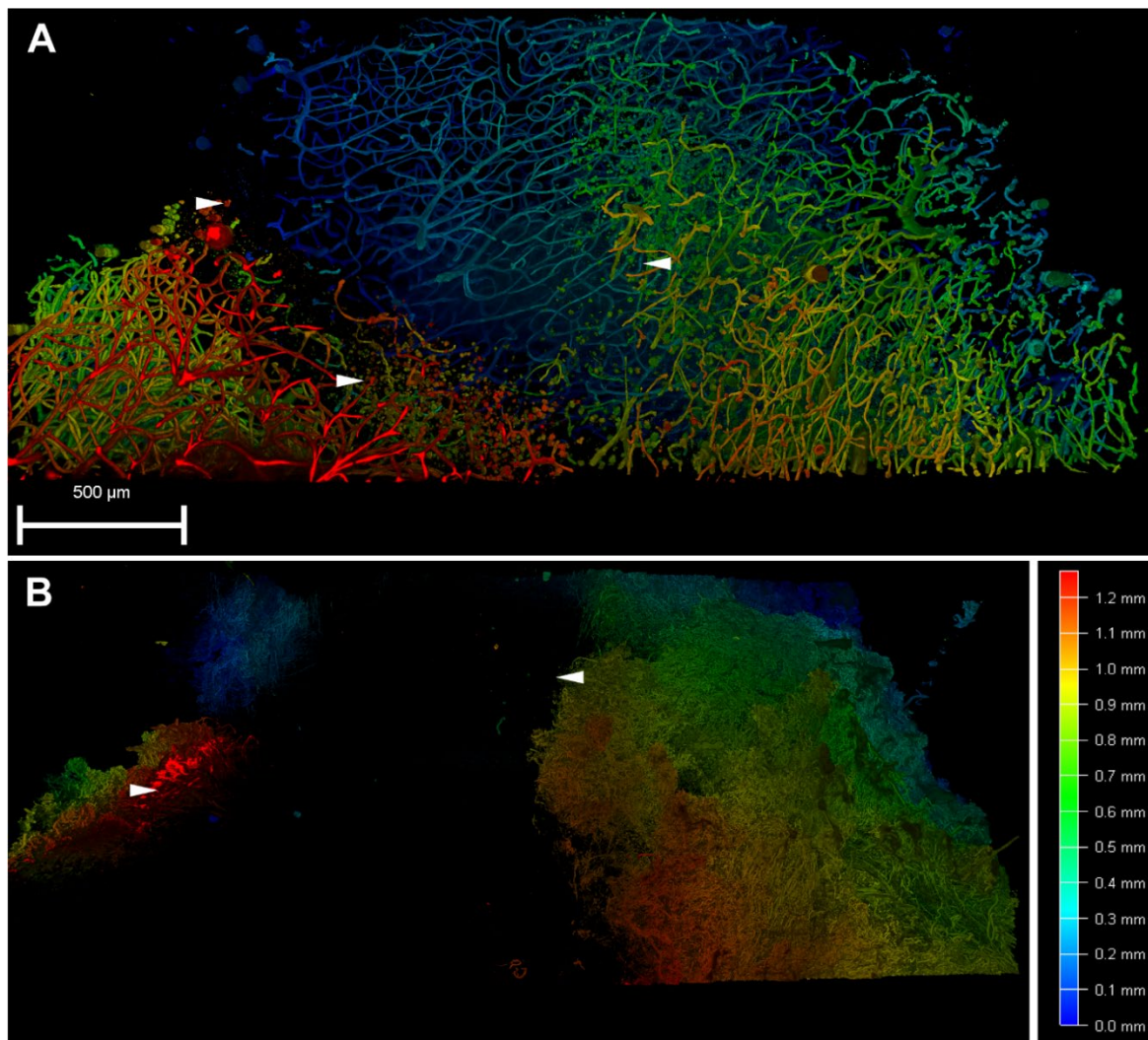


Figure 37 – MYOCLEAR+ with DIMM enables deep imaging of brain tissue. Freshly dissected adult mouse brain samples were fixed and stained with (A) CD-31-647 and (B) NF-488 following the MYOCLEAR+ protocol. Samples were then incubated in DIMM for up to one week, cut into smaller sections in order to fit between the mirrors, and imaged with light sheet using a Leica SP8 DLS. Although MYOCLEAR+ in combination with DIMM for RI matching impressively exhibited no issue imaging the full Z depth range of 1.5 mm, we found the samples more fragile and easier to damage compared to other tissues, with accidental damage caused by a pair of forceps while mounting the sample indicated by the arrow heads.

In addition to brain, we wanted to determine if MYOCLEAR+ would also be able to optically clear more homogeneous tissues which displayed a high amount of pigmentation. Therefore, freshly dissected adult mouse spleens were fixed and stained with CD-169-AF647 following the MYOCLEAR+ protocol. Samples were then incubated for up to one week in the original DIMM solution on a roller mixer at room temperature. After, spleens were cut down to fit between the TwinFlect mirrors and imaged using light sheet as before. As with the brain, we found that MYOCLEAR+ was highly applicable in clearing and imaging spleen samples for the entire 1.5 mm Z depth range of our microscope and resulted in a clear depiction of CD169 positive macrophages located in the splenic marginal zone, Figure 38. Thus, solidifying MYOCLEAR+ as a very promising alternative for imaging these types of tissues.

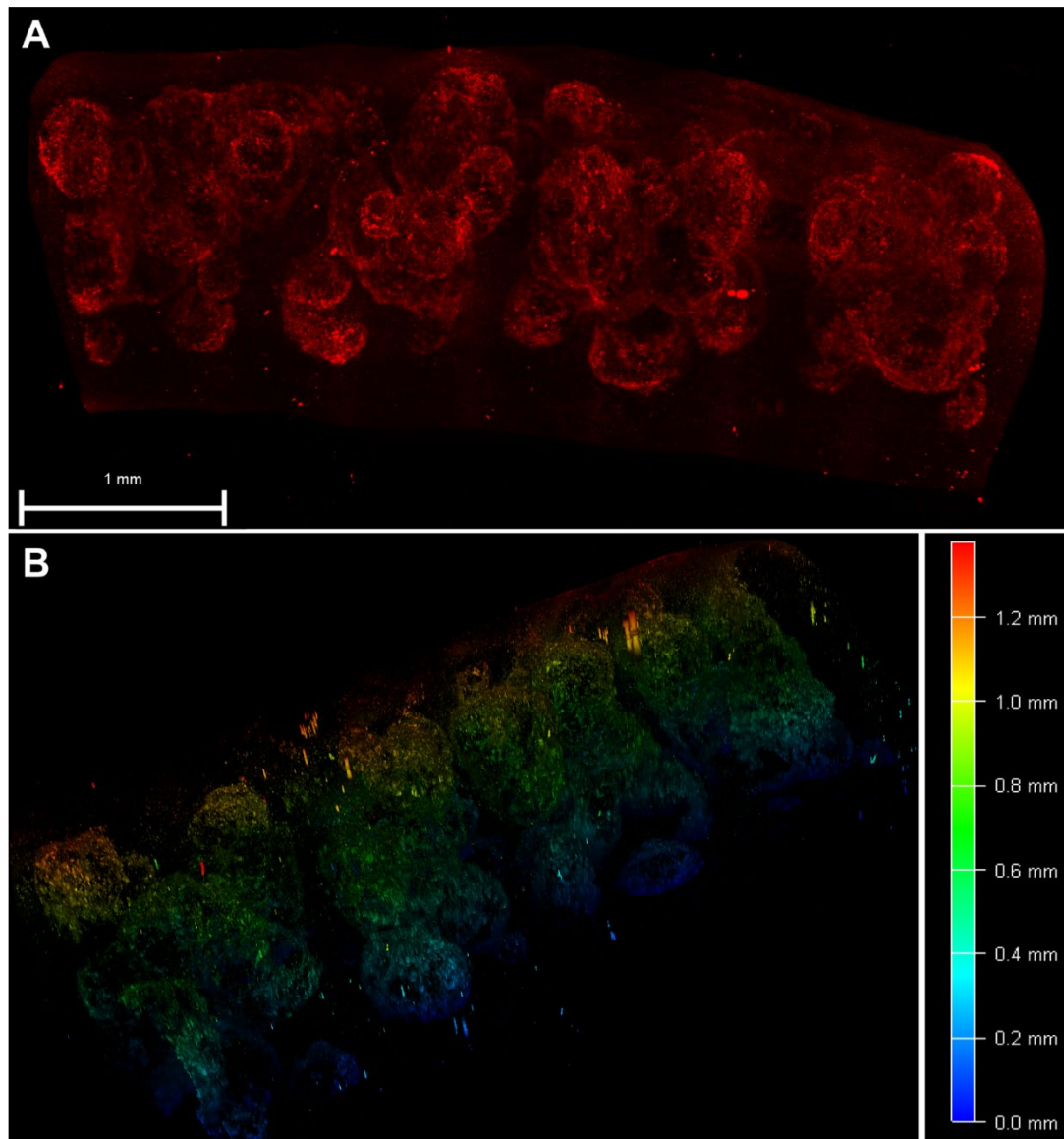


Figure 38 – MYOCLEAR+ with DIMM enables deep tissue imaging in the spleen. Freshly dissected adult mouse spleen samples were fixed and stained with CD-169-AF647, for visualizing CD169 positive macrophages located in the splenic marginal zone, following the MYOCLEAR+ protocol. Samples were then incubated in DIMM for up to one week, cut into smaller sections in order to fit between the mirrors, and imaged with light sheet using a Leica SP8 DLS. (A) depicts a top view with its (B) corresponding depth coded view.

4.3 Cecal slurry model of sepsis

The first hurdle that needed to be overcome to study muscle wasting in a septic model was to confirm that mice stay in a septic state long enough to induce sub-acute/chronic changes proximally and distally as it has been shown that sepsis effects muscles differently depending on location (Friedrich, Reid et al. 2015). This task was especially tricky as the cecal slurry model of sepsis attempts to mimic a ruptured intestinal lining, which is usually associated with models of acute and shock conditions. Nonetheless, after testing many variations of the cecal slurry dosage and treatment regimens, it was found that Starr et al.'s (2014) approach was the most promising. Here, mice were administered a lethal dose of CS intraperitoneally, found to be 200 μ l for our CS stock preparation, with treatment starting 10 hours post-CS injection, and every 12 hours thereafter with antibiotics and fluids. However, as shown in Figure 39, this treatment regimen was found to be too strong, resulting in mice recovering extremely quickly

from their septic state. Therefore, it was thought that this would be insufficient to induce the sub-acute/chronic changes which were needed for our investigations into muscle wasting. To lengthen this time, intervention was extended to every 16 hours instead of 12. This change led to the final optimized model, Figure 39, which was able to extend the septic state of mice by roughly 48 hours, based on the MSS.

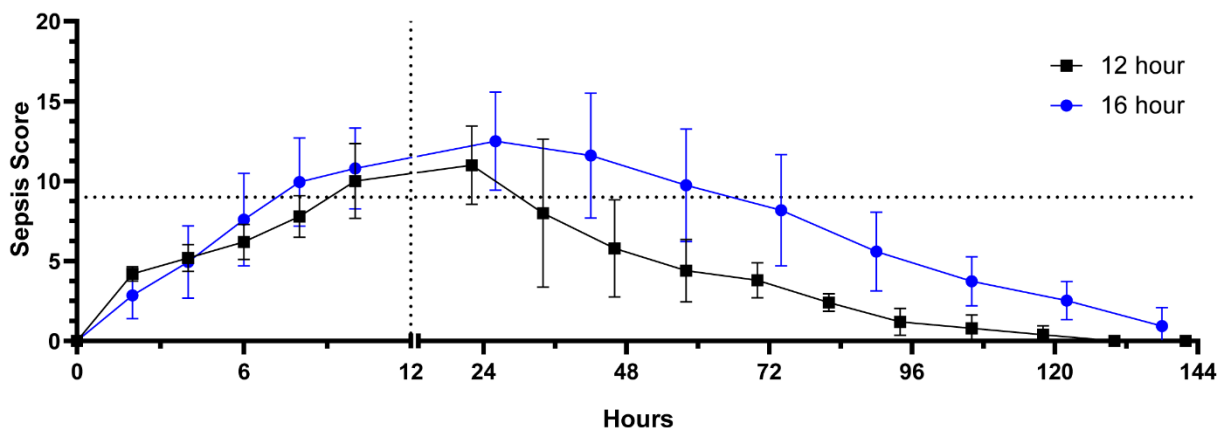


Figure 39 – Adjusting the treatment regimen from every 12 hours post-intervention to 16 hours led to an extension of the septic state in mice. Mice were administered a lethal, 200 μ l dose of CS IP for the induction of sepsis. 10 hours post-insult, intervention with 300 μ l IPM and 700 μ l saline was started and readministered SC every (black) 12 or (blue) 16 hours and the septic state of the mice evaluated at 2, 4, 6, 8, 10 and every 16 hours thereafter based on the MSS scoring system. We found that delaying treatment by 4 hours resulted in an extension of the septic state by roughly 48 hours, when compared to treatment every 12 hours, and an optimal mortality rate of 25%. The horizontal line indicates a sepsis score of 9, with the vertical line indicating the split x-axis (hours), where the first 12 hours spans a more spread-out timeline for visual clarity. $n = 5$ for the 12 hours group and $n = 20$ for the 16 hour group

4.3.1 Evaluation of the cecal slurry model of sepsis as a systemic model and the classification of risk factors associated with muscle wasting

With the optimal septic mouse model established based on the MSS scoring system, we set out to further validate our model and determine if the MSS scoring system is actually a reliable method which corresponds to the septic state of mice. Therefore, sepsis was induced in mice following our optimized CS protocol. Mice were then sacrificed, and samples harvested at 6 hour, 24 hour, and 7 days post-injection, with a duplicate run without intervention for the 24 hour group. For the quantification of bacterial load, blood was collected from the orbital sinus of anesthetized mice, diluted with sterile saline, and plated on blood agar plates. Mice were then sacrificed by cervical dislocation and the spleen and liver removed. Next, portions of each organ were weighed, homogenized, diluted in sterile saline, and plated on blood agar plates in duplicates. After collection, blood agar plates were incubated for 24 ± 2 hours at 37°C . As shown in Figure 40, we found that the bacterial load of blood (134.9 ± 123.1) (mean \pm SD), spleen (885.5 ± 1118), and liver (459.1 ± 505.8) were all significantly increased by the sixth hour post injection, with only the 24 hour group without intervention (1114 ± 1426) still exhibiting a significant amount of circulating bacteria in the blood after this point. Both liver (1880 ± 1537 with treatment, 2718 ± 846.7 without treatment) and spleen (1893 ± 1521 with treatment, 2749 ± 751.7 without treatment) were found to have a significant level of bacteria at 24 hours, regardless of treatment for the 24 hour groups. Interestingly, spleen exhibited a significant bacterial presence even after 7 days (1316 ± 1573), while bacterial levels in the liver (549.4 ± 803.0), though higher than the controls, were not significantly higher by the seventh day. However, since a significant amount of circulating bacteria was found as early as six hours and replicating bacteria could be found up to seven days post-CS injection, it was determined that our treatment regimen was, indeed, started after bacteria had the opportunity to colonize, begin replication, and start to migrate to different regions. Supporting the notion this model

corresponds to a true infectious model and not an intoxication model. Moreover, this provided evidence that distal skeletal muscle should also be affected since the bacteria was not confined to the abdominal cavity.

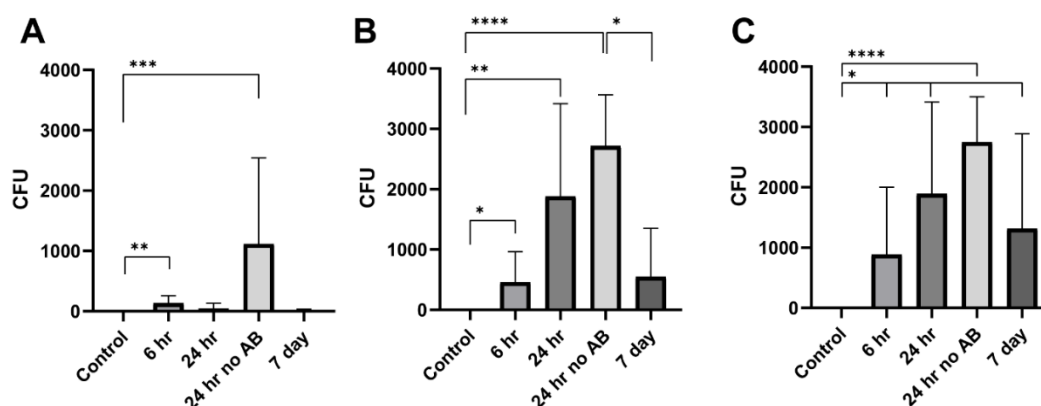


Figure 40 - Bacterial load assessment of septic mice. Bacterial load of the (A) blood, (B) liver, and (C) spleen at 6 hours, 24 hours (with and without treatment), and 7 days post-insult. Mice were administered a lethal, 200 μ l dose of CS IP for the induction of sepsis. 10 hours post-insult, intervention with 300 μ l IPM and 700 μ l saline was started and readministered every 16 hours for the 24 hour (with treatment) and 7 day groups, with no intervention administered in an additional 24 hour group (denoted as “24 hr no AB”). Mice were sacrificed at each time point and blood, liver, and spleen samples collected, homogenized, and plated on blood agar plates in duplicates. Plates were then incubated for 24 hours and CFU manually counted for each. $n = 10$ for control and 6 hour groups, $n = 5$ for 24 hour group, $n = 9$ for 24 hour group with no treatment, and $n = 8$ for 7 days group. * $p < 0.05$, ** $p \leq 0.01$, *** $p \leq 0.001$, **** $p \leq 0.0001$

For plasma analysis, blood was collected from the orbital sinus of anaesthetized mice, as before for all groups, and placed in Heparin collection tubes. Then, tubes were centrifuged, the supernatant collected, and transferred into 1.5 ml eppies. The plasma was then stored at -20°C and analyzed within two weeks from the collection date. Contrary to literature, we observed a decrease in lactate at 6 hr (26.25 ± 7.9) and both 24 hr groups (27.20 ± 8.244 with and 29.56 ± 17.41 without treatment) compared to the control (45.40 ± 8.13), with lactate levels returning to baseline by the seventh day (51.00 ± 8.79), Figure 41(A). For glucose, results were also atypical since hyperglycemia typically manifests in patients with sepsis (Schefold, Bierbrauer et al. 2010). Here, we found a significant drop in glucose levels at 6 hr (103.1 ± 9.37), 24 hr with (85.60 ± 28.23) and without treatment (113.8 ± 49.46), as well as day 7 (150.5 ± 24.70), Figure 41(B). There was no significant difference in ALT values compared to the control (48.11 ± 27.72). However, both 24 hour groups (62.90 ± 32.04 with and 57.44 ± 24.55 without treatment) were significantly higher than at 7 days (23.00 ± 9.49), Figure 41(D). Compared to the control (78.1 ± 38.57), AST values on the other hand, did significantly increase by 24 hours (244.0 ± 110.3 with intervention and 228.1 ± 202.2 without) regardless of treatment, and returned to baseline values by the seventh day (69.75 ± 37.96), Figure 41(E). Although, since AST increased more than ALT, it can be inferred that there was liver damage as well as an additional source for this enzyme, such as muscle (Giboney 2005). Lastly, creatinine (Figure 41(F)) as well as bilirubin (data not shown) were analyzed but showed no significant difference between any of the groups.

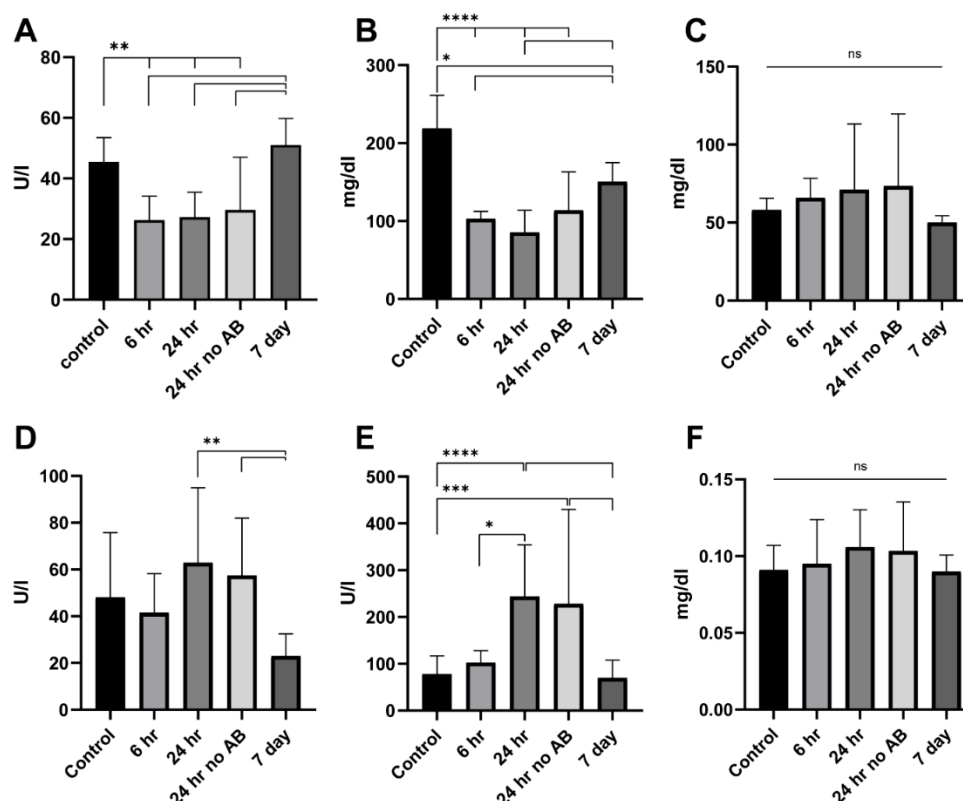


Figure 41 – Plasma analysis of control and septic mice. Plasma analysis of (A) Lactate, (B) Glucose, (C) Urea, (D) ALT, (E) AST, and (F) Creatinine. Mice were administered a lethal, 200 μ l dose of CS IP for the induction of sepsis. 10 hours post-insult, intervention with 300 μ l IPM and 700 μ l saline was started and readministered every 16 hours for the 24 hour (with treatment) and 7 day groups, with no intervention administered in an additional 24 hour group (denoted as “24 hr no AB”). Blood was then collected from the orbital sinus of anaesthetized mice and placed in Heparin collection tubes. Then, tubes were centrifuged, the supernatant collected, and transferred into 1.5 ml eppies. Plasma was then stored at -20 $^{\circ}$ C and analyzed within two weeks from the collection date. $n = 10$ for all control and 24 hour with treatment groups, $n = 9$ for all 24 hour without treatment groups, $n = 8$ for lactate and glucose 6 hour and 7 day groups; ALT, AST, urea, and creatinine 7 day groups, $n = 7$ for ALT, AST, and urea 6 hour groups, and $n = 6$ for creatinine 6 hour group. * $p < 0.05$, ** $p \leq 0.01$, *** $p \leq 0.001$, **** $p \leq 0.0001$

Sepsis has been characterized in literature by an initial intense inflammatory response, or cytokine storm, and is a hallmark of the onset of sepsis (Chaudhry, Zhou et al. 2013, Chousterman, Swirski et al. 2017). Moreover, TNF- α , IL-1 α and β , IL-6, IL-10, and IFN- γ have all been identified as having a role in muscle regeneration and degradation in critical illness (Friedrich, Reid et al. 2015). Therefore, we set out to determine if these cytokines become dysregulated in our model, which would have an impact on muscle function and homeostasis. For this, fresh EDTA blood was collected as before, centrifuged, the supernatant collected, and cytokines measured on a MILLIPLEX mouse cytokine/chemokine magnetic bead panel according to the manufacturer’s instructions. Here, we found that, compared to control levels, TNF- α (2.1 ± 4.6) (mean \pm SD), IL-1 α (26.5 ± 17.6), IL-10 (10.6 ± 5.8) and IL-6 (6.4 ± 11.5) were all significantly increased at six (172.9 ± 47.2 , 341.3 ± 109.7 , 6961 ± 3220 , and 48380 ± 14961 , respectively) and 24 hours post-CS injection, (with treatment 112.7 ± 85.5 , 259.1 ± 126.8 , 8200 ± 6716 , 13800 ± 18880), regardless if treatment was administered (without treatment 150.7 ± 142 , 260 ± 103.8 , 5963 ± 5441 , and 16256 ± 20710 , respectively), with a return to baseline by the seventh day. IL-1 β (0 ± 0) also exhibited an increase at six hours post-CS injection (55.8 ± 15.8) and, although serum concentrations increased to similar levels between the treated (25.4 ± 18.4) and non-treated group (38.4 ± 36.3) at 24 hours, only the non-treated group was found to be significant. Lastly, IFN- γ (0 ± 0) was only increased at six hours (40.3 ± 18.4) post-CS injection, Figure 42. Insinuating that by 24 hours, treatment with antibiotics and fluids did not significantly alter the production of these cytokines and that they

most likely play a role in muscle wasting in the context of our model given the exorbitantly higher levels post-insult.

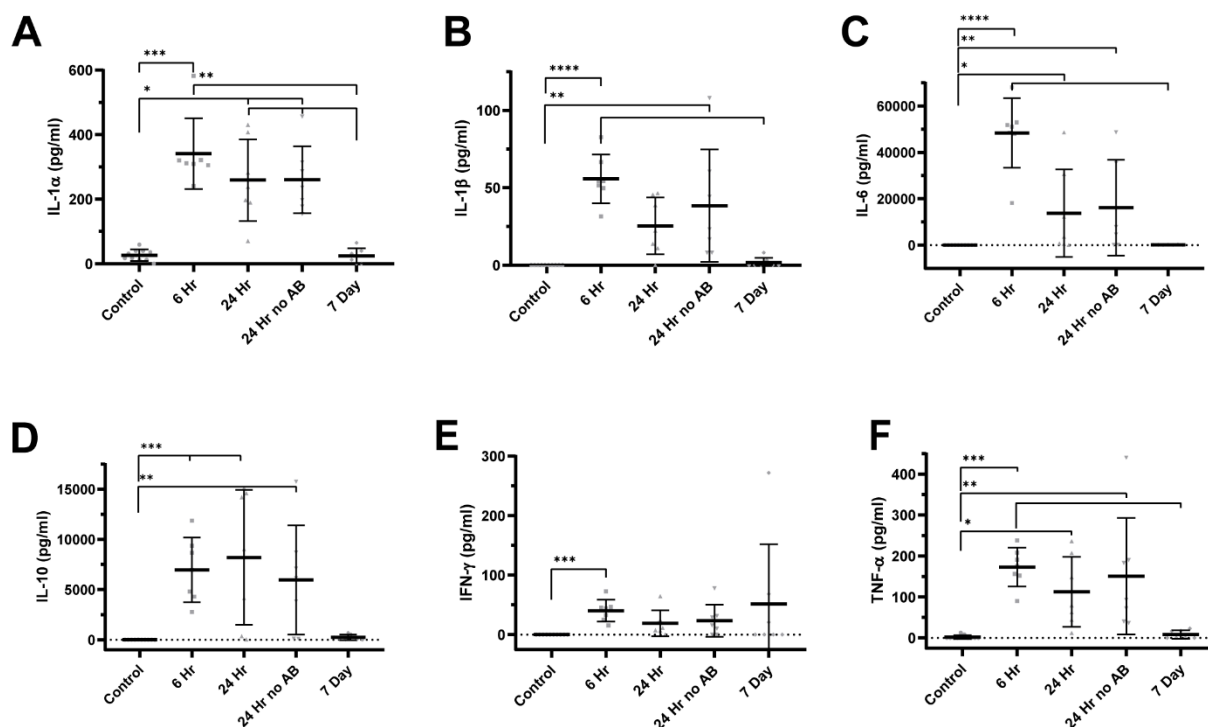


Figure 42 - Cytokine analysis reveals an exaggerated response to a cecal slurry sepsis insult. Mice were given 200 μ l IP injection of cecal slurry, with antibiotics and fluids administered 10 hours post-injection and every 16 hours thereafter. Then blood was collected, as before, in EDTA tubes, centrifuged, the supernatant collected, and cytokines quantified in duplicate on a MILLIPLEX map mouse cytokine/chemokine magnetic bead panel. $n = 10$ for the control group and $n = 7$ for both 24 hour groups, 6 hour group, as well as the 7 day group. * $p < 0.05$, ** $p \leq 0.01$, *** $p \leq 0.001$, **** $p \leq 0.0001$.

Overall activity levels of mice have been used as a marker for various disease models, such as Alzheimer's, dementia, anxiety, and depression (Dodart, Meziane et al. 1999, Holcomb, Gordon et al. 1999, Cryan and Mombereau 2004, Lopatina, Yoshihara et al. 2014). However, all of these studies put mice into special cages or mazes that do not contain housing or other obstructions that impede the view of the camera, which, due to animal ethics, can only be done for short periods of time. Moreover, although activity levels are not typically addressed in sepsis models, there is a clear need for this type of analysis so sepsis induced muscle wasting can be separated from CIM, where immobilization is a risk factor (Schefold, Wollersheim et al. 2020). Here, we were able to track mice in their home cages without this time constraint for seven days. Briefly, IR video recordings were collected starting 24 – 48 hours pre-CS injection and then continued for the duration of the experiment. Pre-CS injection data as well as separate video recordings were used for establishing baseline activity levels. After collection, recordings were broken into hours, post-processed and segmented using ImageJ, and then loaded into the WrTrk ImageJ plugin for automated tracking. Each hourly activity value was then divided by the number of mice left in the cage at the specified time point to reflect single mouse activity levels. Nightly activity levels were then calculated based on the first 8 hours of nighttime. As shown in Figure 43, mice became noticeably active again on the fourth night post-cecal slurry injection (78 hours post-injection). Interestingly, even by the seventh day (994.5 ± 733.2), overall mice activity levels were still significantly lower than control levels (3460 ± 1728). Moreover, there was a general trend towards increasing activity levels over time. This can be taken as a good classification of when mice start to recover from a septic state, which did exhibit a correlation to the MSS score of the mice. Lastly, this also demonstrates that within this model, mice are semi-immobilized by the course of the disease itself which could reflect some of CIM

associated muscle atrophy triggered by immobilization and should, therefore, be taken into account when interpreting downstream results.

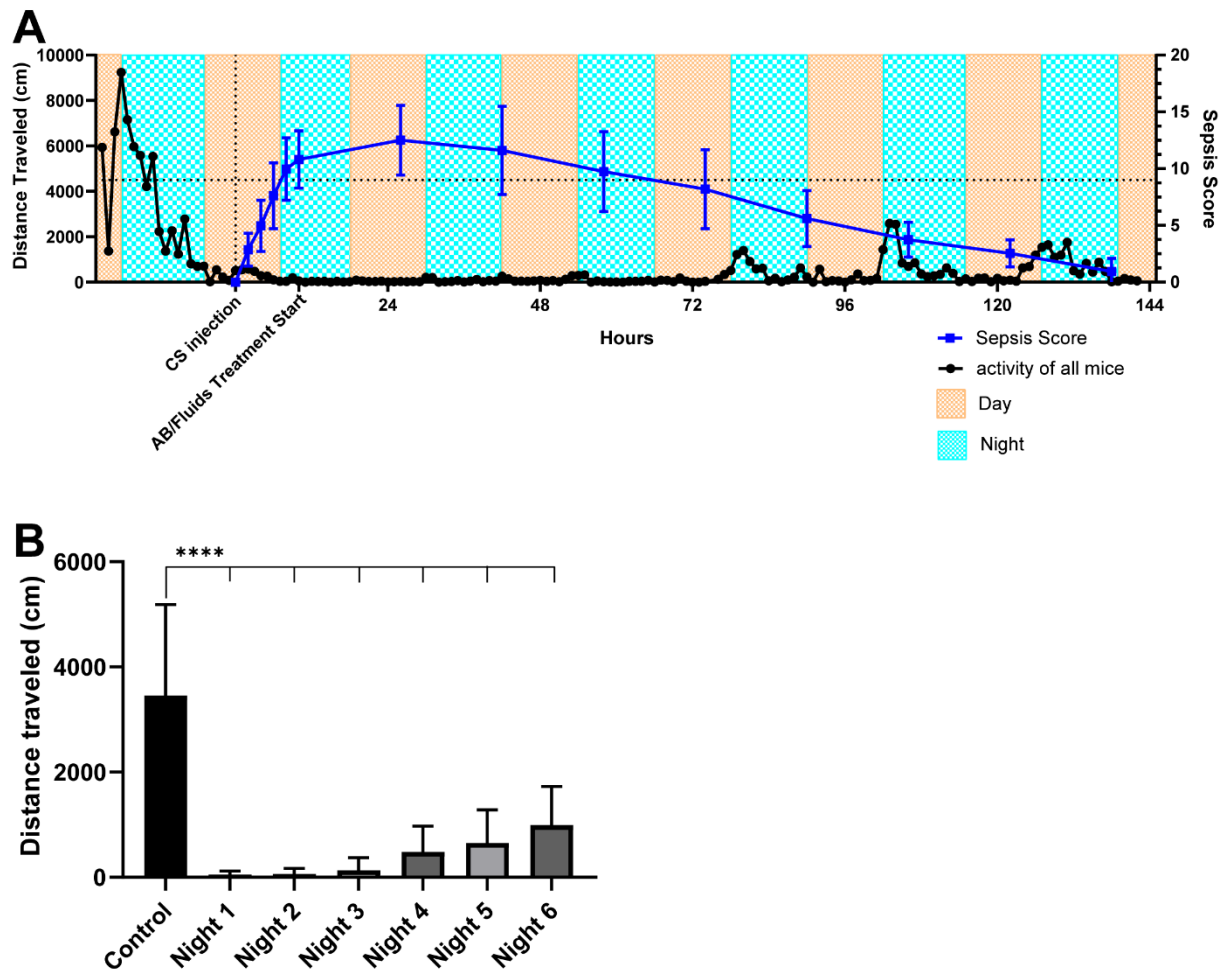


Figure 43 - Tracking of mouse activity levels over the course of sepsis. (A) represents the overall activity level of septic mice over a seven day period, while (B) depicts the nightly activity level of mice in relation to control levels. Video recordings of control and septic mice were collected using a Flir A655sc infrared camera. Then, videos were broken into hours, processed, and segmented using the WrTrk ImageJ plugin. After segmentation, hourly data was divided by the amount of mice left in the cage at that time point. Nightly activity levels were calculated using the first 8 hours of activity per night $n = 10$ for septic mice and $n = 15$ for control **** $p \leq 0.0001$

4.3.2 The cecal slurry model of sepsis, a reliable model for studying septic induced diaphragm dysfunction

After validating how long our mice stay in a septic state by the MSS scoring system as well as activity level tracking, the next step was to determine if this length of time was long enough to replicate the vast septic induced muscle wasting that many patients suffer (Callahan and Supinski 2009). From literature, we hypothesize that there should be a reduction in diaphragm width and fiber diameter. Therefore, mouse hemidiaphragms from septic and control mice were PFA fixed, stained with BGT, and imaged. After imaging, the individual stacks were stitched together and rotated 90° to show a width view of the diaphragm. Next, measurements were collected for both diaphragm width and fiber cross sectional area (CSA) within the NMJ band region using muscle autofluorescence. As shown in Figure 44, diaphragm width significantly decreased from $442.21 \pm 1.3 \mu\text{m}$ to $332.42 \pm 34.28 \mu\text{m}$ as well as fiber diameter from $44.3063 \pm 6.9 \mu\text{m}$ to $35.9 \pm 6.29 \mu\text{m}$, corresponding to a 28.3% and 20.9% loss of volume, respectively. Thus, closely matching the $27 \pm 12 \%$ loss in diaphragm volume in humans (Jung, Nougaret et al. 2014).

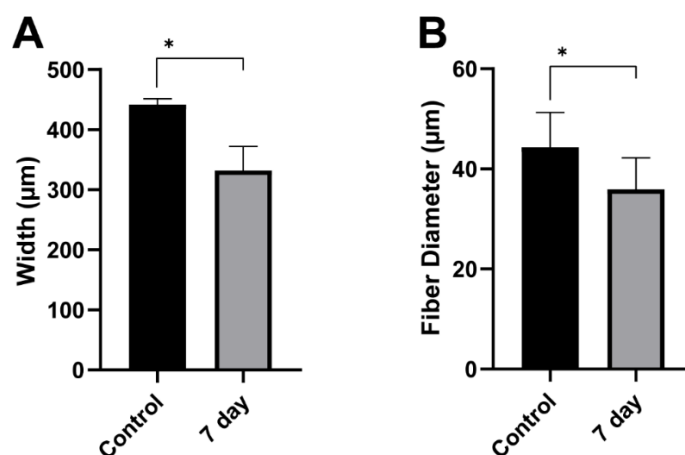


Figure 44 – Sepsis causes a reduction of both diaphragm width and fiber diameter. Sepsis contributed to a reduction in both (A) width and (B) fiber diameter of the diaphragm. Mouse hemidiaphragms from septic and control groups were PFA fixed, stained with BGT, and imaged on an inverted Leica SP8. The acquired images were then stitched, rotated 90°, and diaphragm width and fiber diameter analyzed by hand within the NMJ band region. N = 3 for both groups *p < 0.05

Next, we wanted to determine if the decrease in diaphragm width and fiber diameter was due to muscle atrophy with or without the complete loss of thin or thick filaments within sarcomeres. Therefore, mouse diaphragms from control, 24 hour post-CS injection with no intervention, and 7 days were freshly dissected, put into cryotubes, snap frozen in liquid nitrogen, and stored at -80°C. Samples were then transferred into 2 ml eppies, an equal amount of lysis buffer added to each, and lysed for 3 minutes at 30 Hz. Samples were then centrifuged and the supernatant collected, aliquoted, and stored at -80°C until needed. Lastly, to ensure an equal amount of protein was added, total protein content was quantitatively measured using the Millipore direct detect system as well as qualitatively using Coomassie blue, data not shown. Myosin binding protein-C (MyBP-C) and α -Actinin were chosen as both play key structural and functional roles, with any reduction implying a loss, or unraveling of thick or thin filaments, respectively as well as functional impairment (Boland, Kaur et al. 2018, McNamara and Sadayappan 2018). However, as shown in Figure 45, we found no significant difference in MyBP-C, nor α -Actinin. Although, protein degradation via UPS, a known upregulated pathway in critically ill patients (Hooijman, Beishuizen et al. 2015), was increased as indicated by a significant two-fold increase in both MuRF1 and multi Ubiquitin at 24 hours post CS injection, Figure 45. Moreover, ANKRD1, a stress-inducible myofibrillar protein which plays a key role in skeletal muscle structure, remodeling, and repair (Laure, Suel et al. 2009), was shown to be upregulated by three-fold at 24 hours and seven-fold by day 7, though not significantly.

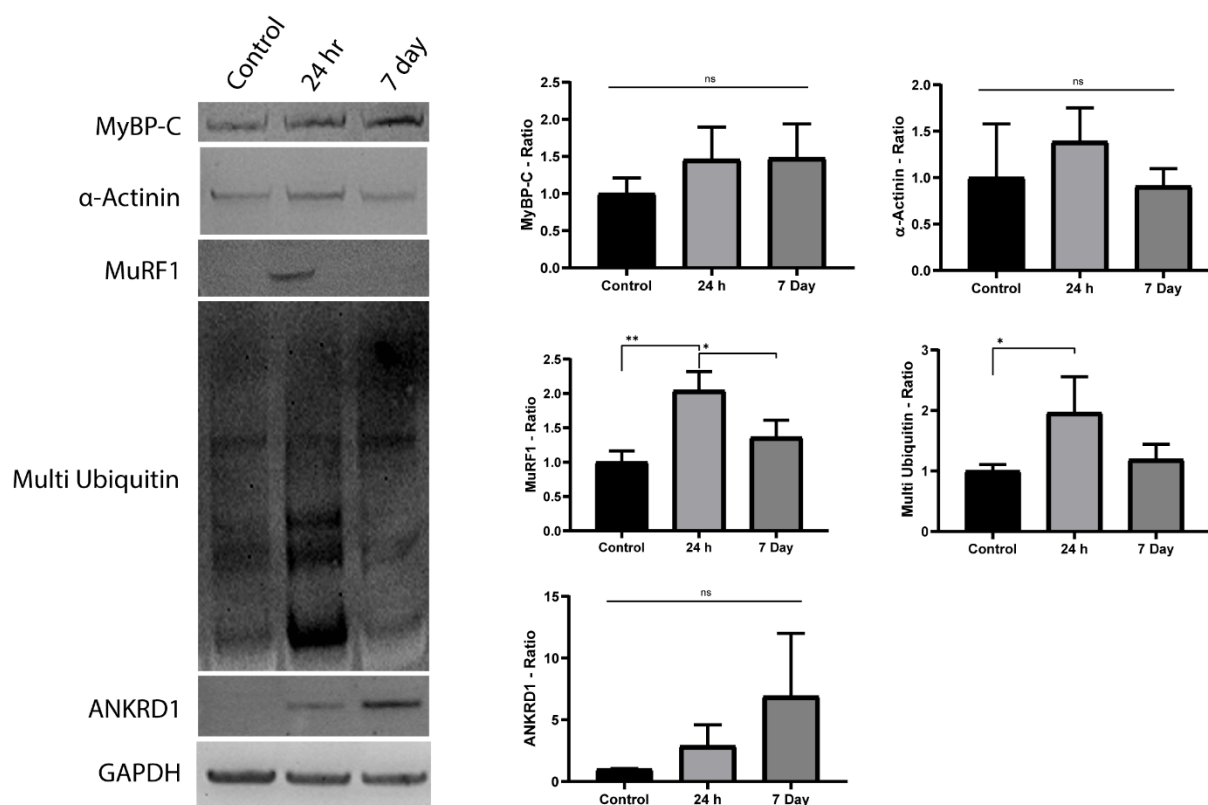


Figure 45 - Sepsis leads to a transient upregulation of MuRF1 and the UPS. (left) representative western blots of MyBP-C, α -Actinin, Murf1, Multi Ubiquitin, and ANKRD1, with (right) their relative ratios normalized to GAPDH. The UPS was found to be upregulated via increases in both Murf1 and multi-ubiquitin, though, key structural proteins (MyBP-C and α -actinin) seemed relatively unaffected. Whole mouse diaphragms from control, 24 hour post-insult with no intervention, and 7 days were freshly dissected, placed into cryotubes, snap frozen in liquid nitrogen, and stored at -80°C . Samples were then transferred into 2 ml eppies, an equal amount of lysis buffer added to each, and lysed for 3 minutes at 30 Hz. Samples were then centrifuged and the super natant collected, aliquoted, and stored at -80°C . $n = 3$ for all groups * $p < 0.05$, ** $p \leq 0.01$

4.3.3 Degradation of the sympathetic nervous system may contribute to NMJ instability and muscle dysfunction

As previously shown by Khan et al. (2016), innervation of the sympathetic nervous system plays an integral role in the function and homeostasis of the NMJ. The loss of SNS innervation has been associated with fragmented and degraded NMJs, increased motor neuron denervation, increased nAChR turnover, and selective myofiber atrophy (Rodrigues, Messi et al. 2019). Although not significant, we did observe a two-fold increase in tyrosine hydroxylase, an enzyme marker for sympathetic nerves (Lund, Knuepfer et al. 1978), at 24 hours, followed by a half-fold decrease by day 7 compared to control values, Figure 46. Indicating that there may be increased SNS activity by 24 hours post-CS injection, followed by a loss of innervation in the diaphragm by day 7. Fittingly, a significant six-fold and one-and-a-half-fold increase in Rab5 and CDK5, respectively, indicate an increase in nAChR endocytic vesicles and turnover (Rudolf and Straka 2019). Lastly, both NCAM, a marker for denervation, and Ankrd2, shown to be upregulated in denervated muscle and a marker for abnormal muscle function, are both significantly upregulated by two- and three-fold, respectively, at day 7. Interestingly, while some researchers indicate either no difference or an increase in ADRB2 expression (Rodrigues, Messi et al. 2019), we observed a decrease in its expression at 7 days, though not significant.

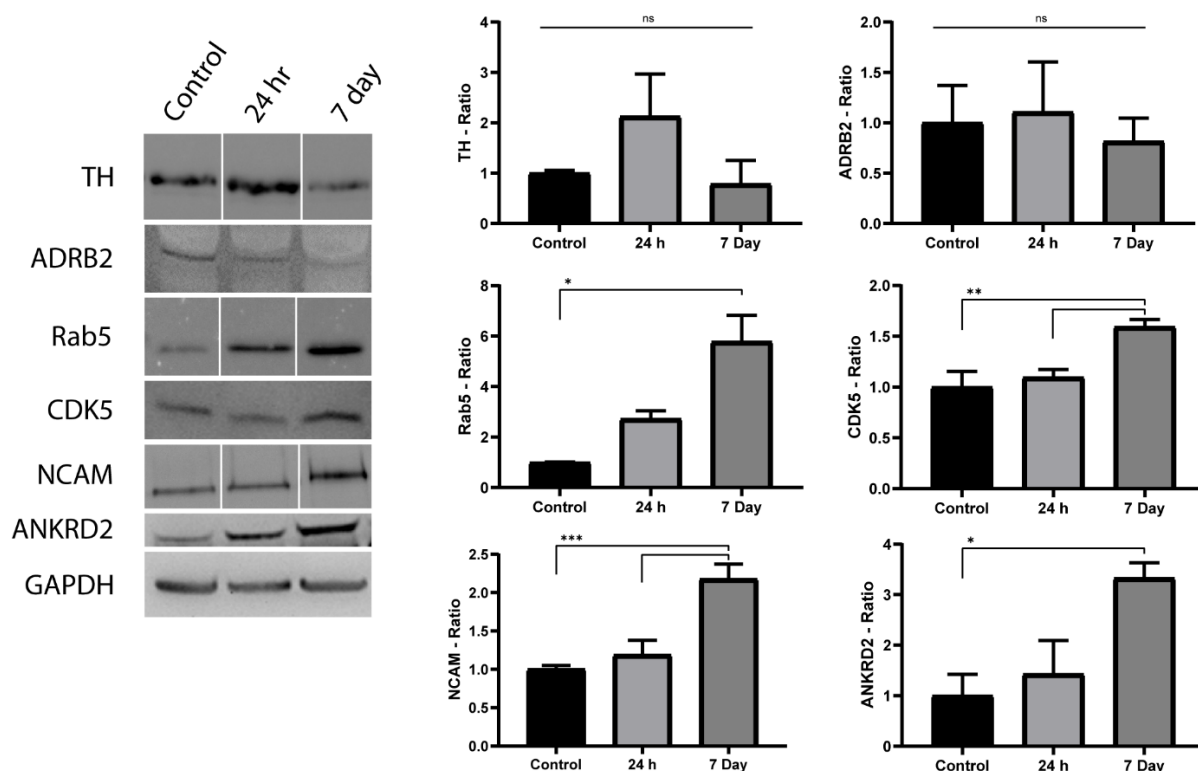


Figure 46 – Loss of SNS in the diaphragm may contribute to NMJ instability in sepsis. Sepsis resulted in a decreasing trend of SNS tone within the diaphragm, as well as significant denervation by the seventh day. (left) representative western blots of TH, ADRB2, Rab5, CDK5, NCAM, and ANKRD2 with (right) their relative ratios normalized to GAPDH. Whole mouse diaphragms from control, 24 hour post-insult with no intervention, and 7 days were freshly dissected, placed into cryotubes, snap frozen in liquid nitrogen, and stored at -80°C . Samples were then transferred into 2 ml eppies, an equal amount of lysis buffer added to each, and lysed for 3 minutes at 30 Hz. Samples were then centrifuged and the supernatant collected, aliquoted, and stored at -80°C . $n = 2$ for TH, ADRB2, Rab5, and NCAM control groups and $n = 3$ for all other groups * $p < 0.05$, ** $p \leq 0.01$, *** $p \leq 0.001$

4.3.4 Sepsis induces fibrosis in the diaphragm and an increase in typical western blotting “housekeeping” proteins

Western blotting is a technique used to quantitatively compare differences in protein expression levels. This technique uses highly expressed proteins, such as β -actin, GAPDH, and Tubulin, as “housekeeping” proteins, or proteins that are not usually altered throughout the time course of a disease or treatment and can be used to ensure an equal amount of protein was loaded from each sample into the gel. Unfortunately, sepsis has been shown to have broad effects on muscle and therefore could alter the expression of proteins not typically changed in other disease models (Friedrich, Reid et al. 2015). Indeed, after assuring the same amount of protein was added to each well by two different protein assays as well as comparing Coomassie blue gels, we found that levels of β -actin, α -tubulin, and α/β tubulin were altered and increased by 25-, two-, and three-fold by day seven, respectively. While GAPDH remained relatively unchanged and was therefore used as our housekeeping protein. Since both β -actin and Tubulin has been shown to be increased in fibrotic tissue (Martin, Lefaix et al. 1993, Randazzo, Khalique et al. 2019), levels of SMAD2/3 and YAP were examined to determine if there was an increase in activity of the fibrosis pathway. Indeed, we found a significant four- and seven-fold increase in SMAD2 and SMAD3 by day 7, respectively. Although not significantly, we also found a one-and-a-half-fold increase in YAP at day 7, Figure 47. Thus, suggesting that there is an increase in fibrosis and regeneration in the diaphragm at day 7, which could partially explain the increases observed in both β -actin and Tubulin.

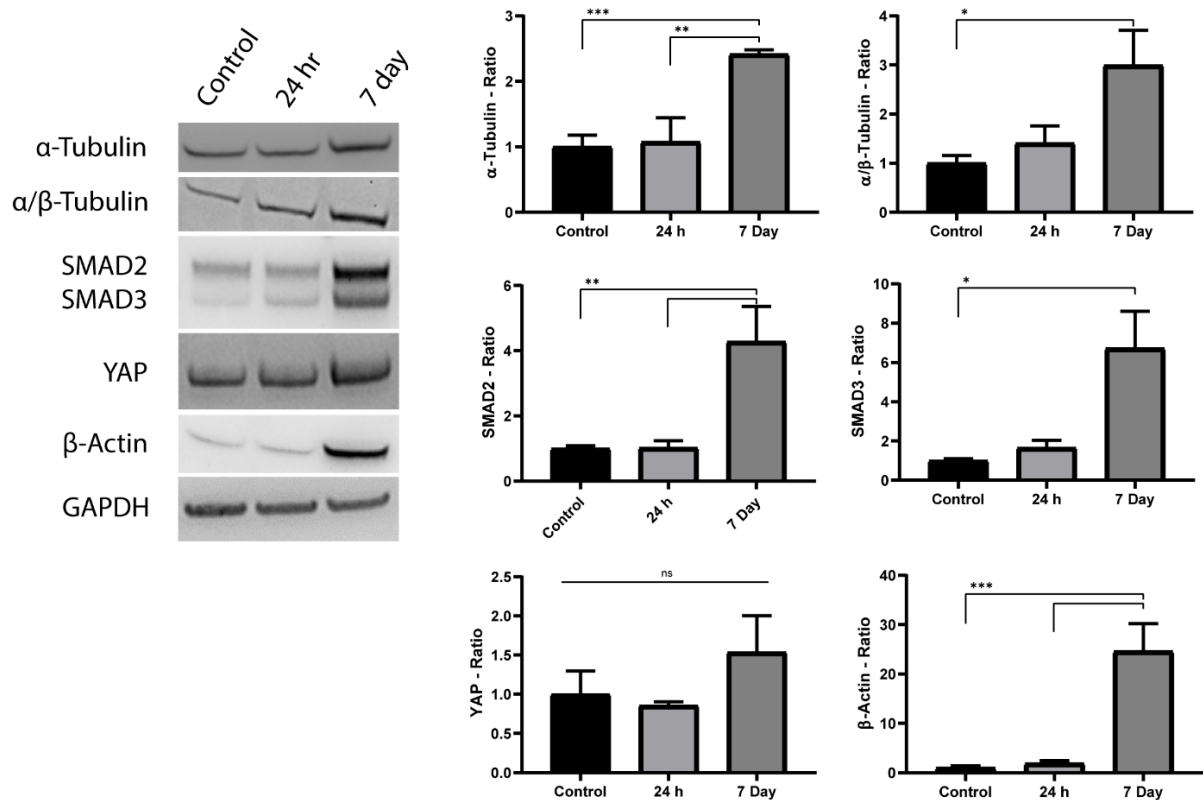


Figure 47 – Sepsis results in an upregulation of the fibrosis pathway. Sepsis resulted in a significant increase in key pro-fibrotic proteins, SMAD2 and SMAD3. (left) representative western blots of β-actin, α-Tubulin, SMAD2, SMAD3, and YAP with (right) their relative ratios normalized to GAPDH. Whole mouse diaphragms from control, 24 hour post-insult with no intervention, and 7 days were freshly dissected, placed into cryotubes, snap frozen in liquid nitrogen, and stored at -80°C. Samples were then transferred into 2 ml eppies, an equal amount of lysis buffer added to each, and lysed for 3 minutes at 30 Hz. Samples were then centrifuged and the super natant collected, aliquoted, and stored at -80°C. n = 3 for all groups *p < 0.05, **p ≤ 0.01, ***p ≤ 0.001

Lastly, to confirm that diaphragm muscle did exhibit signs of regeneration by the seventh day, thereby solidifying fibrosis could be occurring by this time post-insult, whole diaphragms were collected from control and 7 day groups and imaged as before, with the addition of an eMHC antibody staining, as eMHC expressing muscle fibers is a clear indication of regeneration (Rigon, Hörner et al. 2020). In agreeance with our other data, we found that some muscle fibers qualitatively did express eMHC at seven days, Figure 48(A). Furthermore, NMJs found in this region reflected an unhealthy, weak, and semi fragmented structure, Figure 48(A,B).

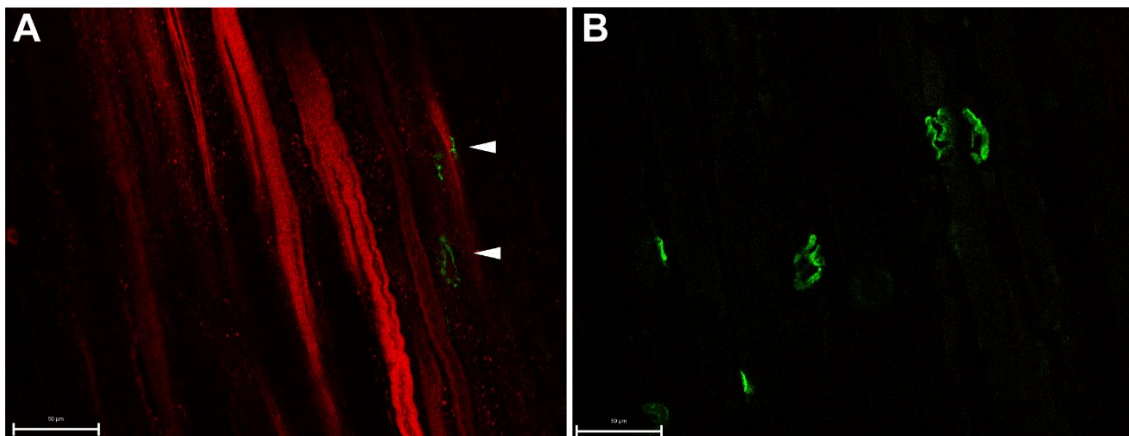


Figure 48 – Sepsis leads to the expression of eMHC by the seventh day post-septic insult. Mouse hemidiaphragms from seven days post-insult septic mice were PFA fixed, stained with BGT-AF555 (green) and eMHC-AF647 (red), and imaged on an inverted Leica SP8, as before. We found many regenerating muscle fibers (A) by the seventh day post-insult. Furthermore, the NMJs located in this region qualitatively exhibited extremely weak signals, compared to NMJs located outside of this region at the same depth into the tissue. Scale bar = 50 μm

5. Discussion

5.1 MYOCLEAR, a reliable skeletal muscle tissue clearing protocol but with limitations

Since the key objective of this work was to evaluate the septic induced changes in the volumetric distribution and morphological state of NMJs as well as their spatial relationship to specific structures, such as the SNS, a relevant TOC method was needed. Unfortunately, the field of tissue clearing has been largely based around the clearing of more homogeneous tissues, such as the brain (Richardson and Lichtman 2015). While there has been a recent trend to apply TOC methods to other, harder to clear tissues, skeletal muscle has been essentially neglected. This is evident by out of the plethora of published clearing protocols, many skeletal muscle TOC studies have only been investigative by nature with only two methods, published in 2019, demonstrating any real promise for clearing and imaging deep into skeletal muscle (Williams, Rigon et al. 2019, Yin, Yu et al. 2019). This can be attributed to the heterogeneous nature of skeletal muscle, which, in our hands, has demonstrated itself to be a highly complex and difficult task. Further compounding the issue, there are no practical substitutes for BGT, the most widely used post-synaptic NMJ marker, which has been found to be incompatible with many of the currently available TOC protocols, with sparse or misleading information regarding the underlining cause.

Therefore, we set out to create a method to deal with the excessive light scattering induced by the various layers of densely packed lipid membranes and connective tissue. While also being compatible with our accessible microscopes as well as retain BGT fluorescence to enable the morphological analysis of NMJs in skeletal muscle. Initially, this led us to investigate CLARTIY based tissue transformation TOC protocols, as they boast the widest range of compatible stainings, portray a decent clearing capacity for more heterogeneous tissues, and are also well suited for most microscopy objectives (Lee, Choi et al. 2016). However, in accordance with Milgroom et al. (2016) and Zhang et al. (2018), we found that preparing and clearing samples using CLARITY based protocols led to a quantitative loss of BGT fluorescence. The interpretation of these studies was that the hydrogel cross-linking in addition to PFA fixation prevented access of the toxin to AChRs. Although, given that many large antibodies, ≥ 150 kDa, are aided by the embedded hydrogel, coupled with the relatively small size of BGT, 7 kDa, we assumed this was most likely not the case. Therefore, we set out to determine the actual cause and found that the loss of fluorescence was directly tied to SDS and not affected by the embedded hydrogel. We assume the reason for this to be since SDS does denature proteins, it denatures AChRs to the point BGT cannot bind, or in the case of staining before clearing, denatures AChRs to the point it releases BGT from its binding site. Therefore, SDS should not be used to delipidate samples when BGT is needed. Moreover, as for antibodies, the embedded hydrogel was found to aid BGT and led to increased imaging depths and a reduction in background auto-fluorescence in the near-infrared channel, presumably due to the hydrogel either supporting BGT-AF647 in a way that it can reach its target more accurately or aiding in washing out unspecific BGT-AF647 signals. These findings led to the establishment of the MYOCLEAR protocol, where samples are not delipidated with SDS but hydrogel embedded, stained, and RI matched using 88% glycerol.

To evaluate the applicability of this method as well as for proof-of-concept, MDX mouse EDLs were chosen due to being well characterized in literature (McGreevy, Hakim et al. 2015). Additionally, the extensive fibrosis exhibited by MDX muscle served as a “worst case scenario” as it has an extremely high probability of negatively impacting the optical properties of skeletal

muscle. Yet, this method did allow for the comparison of most, if not all, NMJs between wild type and MDX mouse EDL muscles. Moreover, it allowed for the evaluation of the area, fragmentation index, perimeter, and bounding rectangle diagonal of NMJs. While impressive on its own, multi-stained skeletal muscle was still needed to evaluate our septic muscle tissue. Unfortunately, MYOCLEAR presented a strong autofluorescence in the blue to red fluorescent wavelength range, most likely due to the formation of Schiff's bases during the PFA- fixation step (Richardson and Lichtman 2015), which made tagging and imaging more than one target impossible within the same tissue. Though, the autofluorescence obtained in the green and red fluorescent channels was rather useful in our preliminary evaluation of septic mice where it was applied to assess diaphragm width and individual fiber diameter changes between our control and septic group. However, even with this analysis, additional markers were still needed as discerning fiber type, selective or non-selective fiber type/myosin loss, and the presence of centro-nucleated fibers are not possible with autofluorescence alone.

Therefore, to permit at least two different structures to be simultaneously marked, we employed the slightly wavelength-shifted dyes AlexaFluor647 and Draq5 in combination with spectral unmixing, since this could give insight into regenerating, centro-nucleated fibers in our septic tissue. Here, we were able to nicely demonstrate the ability to image both dyes up to 1000 μm in adult EDL mouse skeletal muscle. However, it must be stated that NMJs beyond a depth of about 700 to 800 μm from the surface are hardly above background and rendered automated segmentation, volumetric, or in-depth morphological analyses of these synapses and nuclei impossible. Moreover, the imaging of additional channels greatly increased the acquisition time needed. We found that, on average, it takes $\sim 15 - 20$ hours, consists of $\sim 60,000$ individual images, and creates file sizes of around 30 – 50 GB to acquire just one channel of whole mount EDL data using confocal microscopy, depending on the sample and the image quality needed, with the addition of just one channel doubling these factors. Thus, making acquisition a highly time intensive process and highlights the need for adapting this method to faster imaging techniques, such as LSM. Additionally, the simultaneous acquisition of BGT-AF647 and DRAQ5 was only possible due to two main factors: Draq5's unique excitation/emission profile which is shifted far enough away from AF647 to be spectrally unmixed, Figure 49(A), and the use of a confocal microscope's prism to finely adjust the emission collection wavelength range of the two dyes. Unfortunately, Draq5 utilizes a non-protein anthracene derived organic fluorophore and, although literature does state it is possible to conjugate anthraquinones to proteins (Kondzior and Grabowska 2020), there were no commercially available options at the time of writing. Furthermore, unlike the tunable multiband prism used for separating the channels in many confocal microscopes, light sheet microscopes, in particular Leica's DLS microscope, utilize fixed range filter sets which cannot be adjusted or split as was previously done. To address both issues, we decided to investigate a commercially available alternative fluorophore to DRAQ5 and found Phycoerythrin-Cyanine7 (PE-Cy7) as a quality candidate. Given PE-Cy7's peak emission (774 nm) and excitation (565 nm), it would create the possibility of exciting the fluorophore with a 553-nm excitation laser and collect the emission wavelength in the near-infrared channel, with only a slight overlap in the dyes emission Figure 49(B). Which, in turn, would also have the benefit of making light sheet acquisition possible since there would be no need to adjust the emission collection window. Unfortunately, the tested PE-Cy7 conjugated secondary antibody was found to be highly unspecific and was therefore deemed unusable, data not shown. Therefore, we conclude that, while this method is useful for studying the relationship between a single structure and its associated nuclei, it would not be completely applicable in the analysis and evaluation needed for our septic tissue, with this only becoming possible when more robust and specific fluorophore options are commercially available.

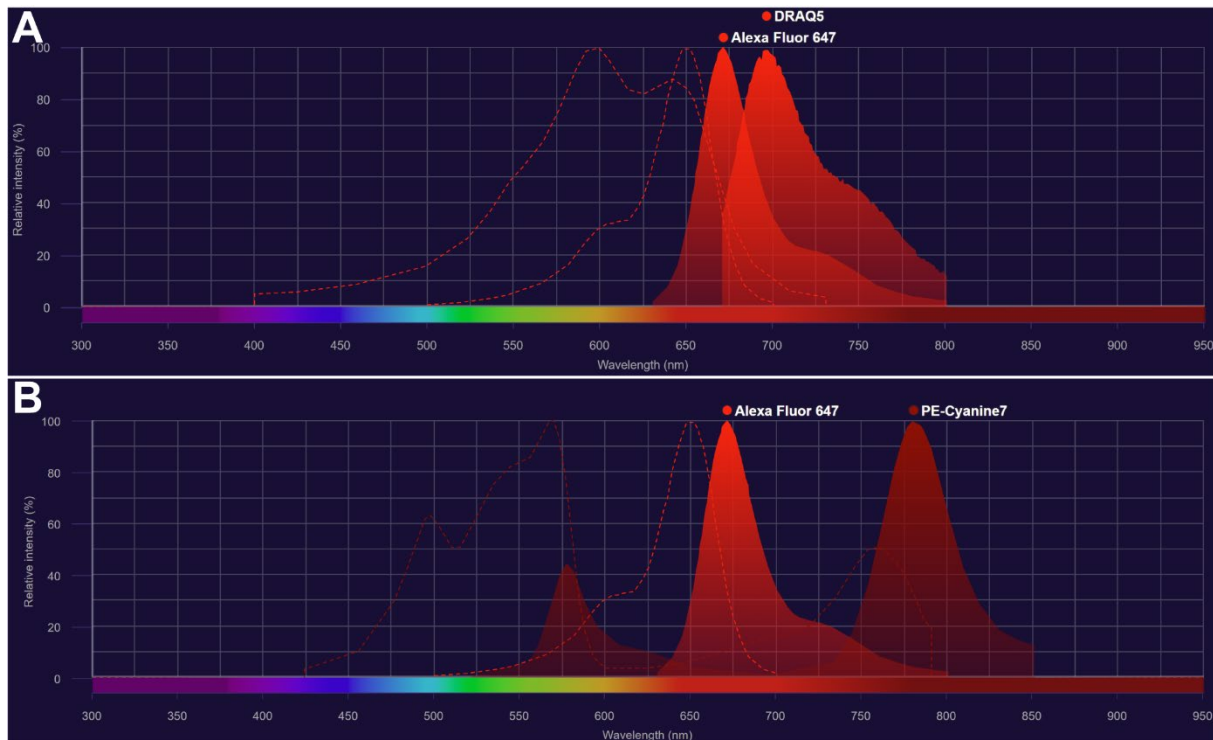


Figure 49 - Comparison of emission and excitation profiles of AF647, DRAQ5, and PE-Cy7. Excitation and emission (A) comparison of AF647 and DRAQ5 and (B) AF647 and PE-Cy7. Images were created using ThermoFisher Scientific's fluorescence spectrviewer.

5.2 MYOCLEAR+, a promising approach for multi-channel LSM acquisition

To circumvent the shortcomings of the original MYOCLEAR protocol, we set out to reduce or remove the PFA induced auto-fluorescence seen in the lower wavelength channels, which, in turn, would simultaneously free these channels for use and create a compatible method for multi-channel light sheet acquisition. Regarding the former, we initially attempted to reduce the fixation induced autofluorescence by lowering the concentration of PFA to 2% and/or shortening the incubation time. However, all variations resulted in the same high autofluorescence in the lower wavelength channels as before, data not shown. Therefore, we chose to evaluate acrylamide as an alternative to PFA for tissue fixation. However, while the practice of embedding tissue with acrylamide for homogenization predates CLARITY by over 30 years (Johnson and Blanks 1984), there has been extremely sparse investigations into its role as a linking agent to biological tissue. Though, Lai et al. (2016) did discover that acrylamide could interact with biological tissue by nucleophilic additions to formaldimines, nucleophilic addition of cysteines, lysine, or histidine to the Michael-receptive double bond of acrylamide, or the formation of simple adducts. Moreover, the authors also state that pre-fixing biological tissue with PFA could block many of these interactions since the reactive formaldimines are rapidly consumed during the PFA fixation process. Therefore, we opted to completely remove PFA and tested various combinations of acrylamide, bis-acrylamide, and VA-044 activator to determine the optimal ratio for fixing biological tissue. Here, we found that fixation with 4% acrylamide, 0.5% bis-acrylamide, and 0.25% of VA-044 reflected very promising results as it was able to qualitatively retain major morphological components including, nuclei, NMJs, and blood vessels. Even so, protein loss or degradation was still a key concern regarding this method. Therefore, we attempted to quantitatively approach this issue and although all values were under the LOD of the pierce 660nm protein assay used, we calculated that mouse EDLs

presumably lost less than 0.83% of protein content no matter the fixation conditions. Though, in hindsight, a more sensitive test should have been employed to confirm these results, such as running aliquots on a gel and using Coomassie blue to detect any protein that may be present as well as adding an un-fixed control sample to validate that our protein assay was able to detect protein loss. In addition, as previously stated, high concentrations of detergents, such as triton-x used to delipidate samples in hyperhydrating methods, has been shown to cause anywhere from 21 – 44 % protein loss in PFA fixed samples (Chung, Wallace et al. 2013). Although our evaluation included 0.5% tween-20 in the solution, protein loss should have been evaluated throughout the entire process to account for the increased concentrations of detergents found in the solutions used for washing, blocking, and antibody incubation. Therefore, the next steps should involve a more detailed investigation into how well acrylamide is able to fix and retain proteins in place to validate acrylamide as a reasonable alternative to PFA.

Nevertheless, the application of MYOCLEAR+ fixation was successful at significantly reducing the auto-fluorescence observed in the lower wavelength channels, thus making them usable for additional stainings. Although, it also, unexpectedly caused an increase in light scatterers across all wavelength channels. While we do not have the exact rationale for this, we assume PFA plays a lesser-known role in tissue RI homogenization as prolonged fixation is known to cause shrinkage and hardening of tissues (Wehrl, Bezrukov et al. 2015), insinuating that water content could be significantly reduced in PFA fixed tissue thereby reducing light scatterers within the tissue. At any rate, either a delipidation step was needed to further homogenize the tissue, or glycerol would need to be replaced with a better suited and more aggressive RI matching medium. Due to the nature of the experimental fixation process we opted not to pursue a delipidation step as this would have significantly increased the probability of protein loss and instead chose to investigate a better RI matching solution. After testing multiple chemicals alone and in combination with others, we found that DIMM was able to attenuate the light scatterers to an acceptable degree. This was especially evident in the more homogeneous brain samples which displayed very minimal scattering throughout the complete 1.5 mm imaging depth. However, for muscle, the quantitative loss of BGT, no matter if samples were prepared following the MYOCLEAR, MYOCLEAR+, or standard PFA fixation methods, was a major drawback of the new mounting solution and needed to be addressed. From literature, we found that the loss of BGT could be caused by the high pH of the DIMM solution as the stability of isolated AChRs during purification by monoclonal immunoadsorption was affected by a pH outside of 6.5 - 8, with a pH dependent decrease in binding efficacy up to 100%. In addition, urea was also cited as another possible cause as exposure to 2 M urea for as little as 60 minutes completely abolished the toxin-binding activity and/or antigenicity of muscle AChRs (Momoi and Lennon 1984). Though, it is important to stress that these results relate to purified AChRs thereby isolated from other factors which could play a role in the interaction of urea and pH with AChRs. Moreover, urea was found to act differently in a tissue clearing context and surprisingly demonstrated compatibility with many GFP and GFP-like proteins at concentrations of 4 M or less (Hama, Kurokawa et al. 2011). Therefore, we expected that the high pH of DIMM was causing the loss of BGT, with urea most likely only playing a marginal role. To test this, we chose to use traditional PFA fixation in combination with confocal microscopy as this drastically decreased the time needed to complete the study. Moreover, diaphragm tissue was utilized as it can be easily cut into multiple sections to produce many samples for testing, in contrast to the EDL. We found that pH does play a vital role in the binding efficacy of AChRs not only in isolated conditions but also in a tissue clearing context, with pH adjustments able to preserve BGT-AF647 fluorescence. Though, urea's role in the loss of BGT fluorescence was not as clear cut. While urea did contribute to overall weaker signal intensities, it did not completely quench the signal and qualitatively represented a more homogeneous signal intensity over the depth of the diaphragm. Additionally, the ability to

image the entire depth of the diaphragm was achievable with or without the addition of urea. Therefore, we can conclude that if BGT is needed, pH should be accounted for in the mounting medium as this has a detrimental impact on signal integrity. However, we cannot say if the increased clearing capacity of urea outweighs the disadvantage of weaker signal intensities as the experimental design using diaphragm did not provide enough imaging depth for this determination. Therefore, additional experiments imaging thicker muscles, such as mouse EDL, stained with BGT, incubated in DIMM with and without urea, using either LSFM or a large working distance confocal objective is needed to compare signal strength and imaging depth of the two mounting mediums. Lastly, we were not immune to the notoriously difficult sample mounting issues LSFM is known for. Unfortunately, since Leica's DLS requires the excitation laser to pass through the bottom of the dish, this meant that the custom-made mounting dish used for MYOCLEAR could no longer be employed. Moreover, prepared samples must be raised roughly 500 μm from the bottom of the imaging dish to allow room for the mirrors to align and image the bottom of the sample. Therefore, samples were mounted on very thin slices of silicon with the use of surgical string and fixed to the base of a glass bottom dish using a small amount of poster putty. While this method does work, it is a very time consuming and tedious task, as one can imagine. Therefore, easier, and more sensible mounting options should be explored for LSFM to increase the ease and practicality of this method. Though, another possible option would be to use MYOCLEAR+ with light sheet microscopes other than Leica's SP8 DLS, as many of these use quartz cuvettes to suspend the sample for imaging, thereby avoiding the tedious mounting process and tissue size limitations of the SP8 DLS.

5.3 Cecal slurry model of sepsis, a robust animal model for evaluating muscle wasting

As previously mentioned, great care must be taken when selecting the correct septic animal model, in relation to its effectiveness in mimicking the specific human pathophysiology which is intended to be studied. Since our main goal was to study the effects of sepsis on diaphragm and distal skeletal muscle tissue, we needed a model that would be severe and chronic enough to cause systemic sepsis induced neuropathies and myopathies. Therefore, all toxemia and purified bacterial injection models could not be used. These are tempting models from an ease-of-use standpoint; however, they fail at replicating most of the long-term tissue damage caused by sepsis and are only a viable option when studying specific, early onset mechanisms (Buras, Holzmann et al. 2005). Other models, such as pneumonia and urosepsis, were also easily taken out of consideration as it was thought that since these are specific compartmental bacterial loads, classifying the initial onset of sepsis as well as inducing distal muscle damage could be problematic. Therefore, we considered the "Gold Standard" CLP method as our model of choice. Indeed, this model has been shown to capture the effects of sepsis on muscle and has been widely used to study muscle in a septic state (Tsukagoshi, Morita et al. 1999, Ito, Fujimura et al. 2006, Píriz, Nin et al. 2008). Unfortunately, due to the ethical scrutiny surrounding the CLP model, invasiveness of the procedure, and lack of robustness, we were unable to get approval from the animal ethics committee, an unfortunate growing trend regarding this model. By default, this excluded the use of CASP as well. From the few murine septic models still left for consideration, the cecal slurry model seemed to be the most promising from the standpoint of animal welfare, ease of use, and reproducibility. However initially, the implementation of this model did raise a few significant concerns. Critics of bolus bacterial insult models have pointed out that CS could result in a model of endotoxemia, rather than a true septic state. Although, this theory has since been, for the most part, proven incorrect by Starr et al. (2014) who revealed that an injection of CS does result in the colonization and replication of bacteria, given that intervention is administered after bacteria has started to circulate, colonize, and

replicate. Therefore, we attempted to create a model based on the protocol published by Starr et al. (2014). Although, it was quickly realized that within their protocol, while successful in inducing sepsis, the administered treatment regimen was too potent and mice rapidly recovered from their septic state, no matter of the CS dose used or time of initial intervention, data not shown. Therefore, the treatment schedule was changed from every 12 hours to every 16 hours, which successfully lengthened the time mice stayed septic based on the MSS scoring system. Though, we found extending the septic state beyond this point using the CS model alone not attainable and marks the only limitation of this model. However, this is understandable given that CS is a bolus injection model which mimics abdominal septic shock via an intestinal rupture. Although, there are publications that have successfully implemented a “two hit” model where an initial abdominal sepsis insult, induced by CLP, is followed by administering bacteria to the respiratory system to mimic the development of hospital acquired pneumonia in human patients after abdominal sepsis (Muenzer, Davis et al. 2006). Therefore, by following up the CS injection with either a pneumonia or urosepsis protocol, it could be possible to overcome this limitation and extend the septic state of mice into a chronic time frame within our model. Nevertheless, as indicated by our bacterial load data, it was determined that our treatment was not administered too early and that bacteria had started to replicate and circulate. Thus, suggesting that our model should reflect sepsis induced proximal and distal muscle alterations. Moreover, we found that our model did reflect the classical activation of the ubiquitin pathway in the diaphragm, indicated by significant increases in MuRF1 as well as multi-ubiquitin at 24 hours post-CS injection. Though, the preservation of MyBP-C as well as α -actinin was not completely expected, as these proteins should have decreased to reflect thick filament unraveling and the subsequent loss of myosin, as well as the loss of thin filaments, respectively (McNamara and Sadayappan 2018). However, we assume that this could be due to either an equivalent decrease of all proteins, which would cause reductions in these proteins not to be reflected in the western blot results or since we demonstrate that regeneration has started by the seventh day, it is also possible that we just missed the time frame which would have reflected a loss and that by seven days, MyBP-C and α -actinin had already regenerated to control levels. Therefore, more time resolved sampling points would be needed to further evaluate the loss of these structural proteins in our model.

However, investigating sepsis induced muscle wasting is not so straight forward, as many risk factors, independent of sepsis, have been shown to contribute to the loss of muscle mass, activation of the UPS, as well as the loss of structural proteins during the course of the disease (Scheffold, Wollersheim et al. 2020). Therefore, glucose levels were analyzed as hyperglycemia is a common occurrence in septic patients and intensive insulin therapy has been associated with lower incidences of ICUAW (shefold 2010). Though, no significant difference was found. We attribute this to the fact that mice did not undergo fasting prior to sample collection, which when taken into account, puts all of our levels within a normal range (Han, Hao et al. 2008). Moreover, the drop in glucose levels seen at six and 24 hours post-CS injection, was most likely caused from the mice fasting due to the immobility triggered by sepsis, as evidenced by the activity tracking data. Therefore, we cannot determine if our model replicates the hyperglycemic state seen in human patients or if it plays a role in inducing muscle atrophy in our model. For this, fasting glucose levels would need to be collected in the future. Although, this does raise the question if fasting could play a role in muscle atrophy in our model. In addition, we did not see any significant difference in creatinine levels. While it has been stated that plasma creatinine levels, under a steady state, can serve as a reliable muscle mass biomarker, many other factors, such as glomerular filtration rate, can impact these values (Patel, Molnar et al. 2013). Therefore, this result was not completely unexpected. Although, since AST increased more than ALT, it can be inferred that there was liver damage as well as an additional source for this enzyme, such as muscle (Giboney 2005). Another major independent risk factor

that is thought not to be present in pure septic animal models is immobility, as animals are not immobilized and only periodically sedated during the procedure. Moreover, CIM induced selective and preferential myosin loss has not been observed in CLP or LPS septic animal models and is therefore thought to play an insignificant role within these models (Friedrich, Reid et al. 2015). However, we show for the first time that immobility should be taken into account as our model, inadvertently, did cause a substantial and significant immobile period due to the severity of the disease itself. Therefore, CIM induced atrophy could play a role in muscle loss in the case of our model. Since CIM affects proximal muscle groups more often than distal (Schefold, Wollersheim et al. 2020), we did attempt to quantify if the diaphragm exhibited the hallmark preferential and selective loss of myosin, as well as the presence of predominant type II muscle fiber atrophy. Though, unfortunately our lysates were found to be incompatible with the necessary antibodies for western blotting and new samples prepared with a urea-based lysis solution would be needed for this analysis. In addition, diaphragm and distal slow and fast twitch representative muscle samples should be collected around the three to four day mark, since if immobility does play a role, this time point would be just before mice become active and should reflect the hallmarks of CIM before the manifestation of CIP. Which we do believe to be the case as the increase in fibrosis seen in the diaphragm is more associated with CIM than CIP. Therefore, it is our impression and in agreement with Friedrich et al. (2015) that CIM is most likely present in pure sepsis animal models, and this has not been confirmed due to the need of more time resolved data points. Though, it is also possible that previously used models were not severe enough or did not keep the animals in a septic state long enough to produce the immobility seen in our model.

In addition, we display a large amount of evidence that CIP did manifest itself in our model by the seventh day post-insult, with a significant increase in both NCAM and ANKRD2 indicating a substantial loss of innervation in the diaphragm. Moreover, while we do partially attribute the significant increase in β -actin and tubulin to fibrosis, it has been shown that regenerating motor neurons after a spinal cord injury can contribute to increases in both proteins as well (Bisby and Tetzlaff 1992, Lund, Machado et al. 2002). Therefore, it would be interesting to investigate if regenerating nerves also played a role in these observed increases. Moreover, given the alterations detected in these routinely used housekeeping proteins for western blotting, we recommend that future studies use caution when selecting β -actin or tubulin for the purpose of protein normalization for the analysis of septic tissue. Even GAPDH, the housekeeping protein utilized in this study, has been shown to be altered in the case of sepsis (Sarveswaran, Orsi et al. 2012, Cummings, Sarveswaran et al. 2014), which is why we confirmed the protein content of our lysates using two different protein assays as well as with the use of Coomassie blue. Therefore, we suggest a protein assay, in combination with Coomassie blue always be included when analyzing septic tissue and that better housekeeping proteins should be investigated in the future.

Although not significant, we also show an initial increase of TH, most likely due to increased activity for immunoregulation (Pongratz and Straub 2014), followed by a decrease at day seven. Thus, indicating, for the first time, a partial loss of the SNS induced by sepsis in the diaphragm. Though, it should be noted that only two controls were used for statistical calculations and that including additional samples would more than likely reflect a significant loss and should be completed in the future. However, since the loss of sympathetic nerve fibers is used as a marker for the transition from acute to chronic inflammation, we can safely assume that our model reflects a sub-acute/chronic representation of sepsis (Wei, Liang et al. 2020). While we were successful in clearing and imaging control and septic diaphragms to further evaluate the decrease in TH in relation to the direct sympathetic innervation of NMJs, most data gave rise to atypical ring-like structures throughout, data not shown. At this point, we do not know

whether this was caused by sepsis or if it just represented artifacts in the images. Therefore, all acquired data is considered unusable until this can be determined in the future. Nevertheless, the unexpected decrease in ADRB2 seems to be either a diaphragm or sepsis specific mechanism, as ADRB2 has only been shown to either remain at a constant level or increase in its expression after SNS ablation in the gastrocnemius and tibialis anterior, respectively (Rodrigues, Messi et al. 2019). Although again, more samples should be added to the analysis to confirm if this is a significant loss or not.

At any rate, we hypothesize that the loss of both the SNS and ADRB2s plays an important role in septic induced muscle wasting, as NMJs would no longer be maintained by the SNS, which has been shown to be crucial for NMJ function and leads to muscle atrophy (Khan, Lustrino et al. 2016, Rodrigues, Messi et al. 2019). Moreover, the SNS has previously been shown to attenuate the expression of TNF- α , IL-6, IL-12, IFN- γ , MIP-1 α , and nitric oxide, while increasing the production of the anti-inflammatory IL-10 (Haskó and Szabó 1998). Therefore, it could also play an indirect, or possibly direct, role in the suppression of specific protein degradation pathways as well as preserving muscle function, with the loss of the SNS leading to increases in MuRF1, a known TNF- α stimulated E3 ubiquitin ligase, increases in local TNF- α levels which has been shown to induce muscle dysfunction by itself at high concentrations (Friedrich, Reid et al. 2015), and an increase loss in diaphragm width and fiber diameter. Therefore, it would be highly interesting to investigate if patient biopsies from terminal or non-terminal chronic septic patients also reflect this loss of the SNS and ADRB2 expression. As for our animal model, it would be interesting to see if extending the septic state of the mice into a chronic timeframe would result in an increased reduction in both sympathetic tone and ADRB2 expression. In addition, it would be interesting to see if treatment with a sympathomimetic would lead to a reduction in local, as well as systemic, levels of TNF- α , IL-6, IFN- γ , and nitric oxide which, in turn should reflect decreases in MuRF1 and atrogin-1 as well as a retention of diaphragm function, width, and fiber diameter. Although, it is important to note that autophagy is required to maintain muscle mass, with inhibitions or alterations to the ubiquitin-proteasome and autophagy-lysosome pathways possibly contributing to myofiber degeneration and weakness in muscle via the accumulation of abnormal mitochondria and inclusions (Masiero, Agatea et al. 2009). However, since there is a classical imbalance between protein synthesis and degradation to a detrimental point in sepsis (Schefold, Bierbrauer et al. 2010), treatment with a SNS agonist could have the potential to rebalance this and should be investigated in the future. Moreover, SNS ablation has been shown to cause an upregulation of MuRF1, muscle atrophy, and a downregulation of postsynaptic AChR (Rodrigues, Messi et al. 2019). Thus, providing additional evidence that treating the loss of the SNS and ADRB2 in septic patients has the potential to decrease muscle loss and improve the health-related quality of life of sepsis survivors.

6. Summary

In summary, we provide MYOCLEAR, a highly robust TOC protocol which enables the analysis of most, if not all, NMJs between wildtype and MDX mouse EDL muscles. In addition, it also allows for the evaluation of a single structure and its associated nuclei. We also provide a very promising MYOCLEAR+ protocol which removes the PFA-induced auto-fluorescence seen in the lower wavelength channels, as well as being compatible with LSFM. Though, in its present state, recommending MYOCLEAR+ for routine use may not be the best option as protein loss or degradation is still a key concern of this method and needs further evaluation. Nevertheless, we also present data that shows pH and urea do effect BGT binding efficacy in a tissue clearing context and should be accounted for when this type of staining is needed. Moreover, while adapting this method to LSFM did come with many unexpected issues, the acquisition time saved was found to be well worth the inherent drawbacks. Therefore, we recommend future developments to continue the adaptation of this and other TOC methods to LSFM or other faster imaging techniques. We also provide a new RI matching mounting medium, DIMM, which performed better than glycerol alone and can be used as a standalone high-refractive index aqueous solution for clearing relatively small or thin tissue or in combination with our TOC protocols described here as well as other tissue transformation and hyperhydrating methods. Lastly, while we did contemplate implementing the very promising approach Yin et al. (2019) developed using 3DISCO to clear skeletal tissue, this method and all other solvent based clearing methods could not be tested or directly compared to our approach due to our lack of availability to compatible microscopes. Though, it would be a highly interesting comparison given it is the only other published method that has successfully analyzed large, whole mount muscle data.

In relation to sepsis, since many past muscle wasting investigations utilized the “gold standard” CLP model of sepsis, not being able to use this model was initially considered a fairly detrimental setback of our project. Although, the overall robustness demonstrated by the CS model of sepsis in replicating such a heterogeneous disease far outweighed the disadvantages of not using CLP and, in retrospect, is considered a justifiable measure for animal welfare, even when considering the issues encountered while attempting to extend the model from a septic shock/acute model to a sub-acute/chronic model of sepsis. Moreover, unlike CLP which was adapted from use with large animals to small animal, cecal slurry was specifically created for small animals, which we found to be well suited for these types of studies (Buras, Holzmann et al. 2005). We also found that the batch preparation and storage of the CS stock solution proposed by Starr et al. (2014) to be great for classifying and determining the bacterial content prior to use and created to possibility to use the same batch for many rounds of experimentation. Thus, considerably increasing the robustness of this method as well as its ease of use compared to fresh fecal slurry alternatives, CLP, and CASP where the bacterial content of the insult cannot be accounted for. Though, no matter the model used, we strongly recommend that future studies implement a scoring system, such as the MSS, and that mortality rate should not be the only marker for a successful model. As this would be highly advantageous given how time sensitive sepsis is and would aid in the interpretation and comparisons between different studies and animal models. In addition, we found our modified CS model to be a clinically relevant sub-acute/chronic model which is able to reflect many of the muscular alterations associated with septic patients. Moreover, we provide evidence for the first time that specific independent muscle atrophy risk factors associated with CIM, such as immobility and fasting, should be investigated further for their role in pure sepsis animal models. Lastly, we provide evidence for the late manifestation of CIP and that the partial loss of the SNS is not just limited to the spleen and skin but also affects the diaphragm, with the observed decrease in ADRB2 a possible

diaphragm or sepsis specific mechanism. Therefore, future investigations should focus on the SNSs ability to regulate cytokine production, and if treatment for the partial loss of the SNS would attenuate the decreases in ADRB2 expression as well as the loss of muscle in septic patients.

7. Appendix

Figure List

- Figure 1 – Schematic diagram of the optical pathway and principal components of a laser scanning confocal microscope.** Adapted from Claxton, Fellers et al. (2005)..... 4
- Figure 2 – Representation of a microscopy Z-stack and tile scan merging.** Where (A) is a visual representation of a Z-stack and (B) of tile scan merging. Adapted from: www.Leica-Microsystems.com..... 5
- Figure 3 – Concepts of Microscopy.** Depiction of an air disk in XY (A) and XZ (B). While (C) portrays the beam path in the creation of the airy disk (a), its relative intensity distribution (b), as well as a 3D representation of the PSF. Adapted from: (A) <https://www.ibiology.org/talks/resolution-in-microscopy/>, (B) Conchello and Lichtman (2005), and (C) <http://zeiss-campus.magnet.fsu.edu/print/basics/resolution-print.html>..... 6
- Figure 4 – The effects of Numerical Aperture on resolution.** (A) low and (B) high NA objectives result in different banding patterns of diffracted light in XZ, with high NA objectives able to produce a wider separation between wavelets and a smaller central peak. This is due to (C) the higher NA objectives wider angular aperture (α) which allows for a more focused banding pattern while also collecting more of the emitted light. (D) depicts the effects of NA on the resolving power of an objective in XY while imaging the same beads with a (a) low, (b) average, and (c) high NA objective. Sources adapted from: (A and B) <https://www.ibiology.org/talks/resolution-in-microscopy/>, (C) <https://www.microscopyu.com/microscopy-basics/numerical-aperture>, and (D) Françon (1961) 7
- Figure 5 – Affected fluorophore bleaching areas of Confocal and Light Sheet microscopy.** (A,C) LSFM results in less out-of-focus fluorophore bleaching when compared to (C,D) confocal microscopy. Adapted from: <https://www.microscopyu.com/techniques/light-sheet/light-sheet-fluorescence-microscopy...> 8
- Figure 6 – Traditional light sheet microscope beam path.** Adapted from: <https://www.leica-microsystems.com/science-lab/confocal-and-digital-light-sheet-imaging/>.. 9
- Figure 7 – Leica Microsystem’s Digital Light Sheet.** (A) beam path of Leica’s DLS excitation laser, with a visual representation of (B) DLS compared to (C) traditional LSFM. Adapted from: <https://www.leica-microsystems.com/science-lab/confocal-and-digital-light-sheet-imaging/> 10
- Figure 8 – Representative fluorescent proteins across the spectrum.** created using ThermoFisher Scientific’s fluorescence spectraviewer..... 11
- Figure 9 – Constructive and destructive interference.** Visual representation of (a) constructive and (b) destructive interference. Adapted from: Geesink and Meijer (2018)..... 13
- Figure 10 - Updated classical taxonomy of tissue clearing methods.** Adapted from: Matryba, Kaczmarek et al. (2019)..... 15

Figure 11 - Distribution of NMJs and the innervation pattern of the gastrocnemius. Source: (Yin, Yu et al. 2019)	17
Figure 12 - Sepsis mortality rates in relation to disease severity. Adapted from: www.sepsis.com (2017)	21
Figure 13 - Inflammatory and anti-inflammatory cytokines response in sepsis. Adapted from: Buras, Holzmann et al. (2005).....	23
Figure 14 - Surgical methods for cecal ligation and puncture and colon ascendens stent peritonitis experimental sepsis models. Visual representation of (A) CLP and (B) CASP surgical techniques. Adapted from: Buras, Holzmann et al. (2005)	28
Figure 15 – Overview of skeletal muscle anatomy. Adapted from: Tortora and Derrickson (2012)	32
Figure 16 - Structural proteins and the organization of the sarcomere. Adapted from: Boland, Kaur et al. (2018).....	34
Figure 17 – Synaptic transmission at the neuromuscular junction. After calcium binds to synaptic vesicles due to an action potential, (1) acetylcholine (ACh) is released into the synaptic cleft and (2) binds to acetylcholine receptors (AChRs) located on the postsynaptic cleft. (3) Sodium is then released and an action potential is produced. (4) ACh is then broken down by acetylcholinesterase (AChE) and sent back into the presynaptic neuron where it is recycled for future use. Adapted from: Tortora and Derrickson (2012)	35
Figure 18 - Proposed mechanisms of muscle wasting in sepsis. Adapted from: Lee and Kim (2010)	37
Figure 19 - Risk factors involved in muscle wasting and ICUAW. Adapted from: Schefold, Bierbrauer et al. (2010)	38
Figure 20 – Workflow of the MYOCLEAR protocol. This panel gives a graphical overview of the MYOCLEAR protocol, with the images next to processing days 0, 10, and 17 depicting representative EDL muscles at their respective time points.	48
Figure 21 – Custom nitrogen bubbling chamber and mounting dish. (A) nitrogen bubbling chamber for degassing samples prior to polymerization, as well as a (B) top and (C) side view of the mounting dish used for MYOCLEAR processed EDLs.....	49
Figure 22 – Workflow of MYOCLEAR+ protocol. This panel gives a graphical overview of the MYOCLEAR+ protocol, with the images next to processing days 0 and 17 depicting representative EDL muscles at their respective time points.	50
Figure 23 - 3D print model of sample holder. In order to keep sample from floating, a custom sample holder was modeled using Inventor professional and printed on an Ender 3. (A) depicts a 3D render of the sample holder, with (B) displaying the printed holder in PLA.	51
Figure 24 – 3D model and print of Infrared camera mounting system. (A) represents a 3D render of the (B) printed camera mount used to track temperature and activity variations of septic mice.....	52

Figure 25 - Active and passive CLARITY-derived methods lead to a quantitative loss of BGT-AF647 staining but retain Lectin-mediated labelling of NMJ ECM. (A) EDL whole mounts were PFA fixed, embedded in hydrogel, and stained with BGT-AF647. After overnight incubation in 88 % glycerol, BGT-AF647 fluorescence was checked (before clearing). Then, glycerol was washed out via PTwH followed by different clearing procedures as indicated on the left. Finally, all samples were again equilibrated in 88 % glycerol and BGT-AF647 fluorescence was visualized (after clearing). Panels show maximum-z projections of confocal image stacks prepared on a Leica SP8. SNR \pm SD values are indicated on upper right angles of each panel. (B-C) EDL whole mounts were cleared using the X-CLARITY protocol and then stained with WGA-488. After overnight incubation in 88 % glycerol, WGA-488 fluorescence was measured. (A) Maximum-z projection of a representative confocal image stack prepared on a Leica SP8. Scale bar, 200 μ m. (B) Detail from the boxed region in A. Arrowheads, NMJs. Scale bar, 50 μ m. 55

Figure 26 - Sequence of staining and hydrogel embedding affects overall imaging depth and quality of muscle samples. All samples were imaged in 3D using a Leica SP8 confocal microscope and images were processed with Leica LAS X software. (A–C) Mouse EDL muscle was PFA-fixed, hydrogel embedded, stained with BGT-AF647, and then RI matched in 88% glycerol before imaging. (D–F) Mouse EDL was PFA-fixed, stained with BGT-AF647, hydrogel embedded, and then RI matched in 88% glycerol before imaging. (A,D) depict overviews of the whole mouse EDL muscles with the boxed region representing zooms shown in (B,E). (C,F) portray cross sections cropped from the center of the EDL imaging data and depth-coded on the z-axis in order to visualize imaging depth and quality for both methods. (G) Graphical display of NMJ-signal SNRs in correspondence to muscle tissue depth and staining / clearing order. Muscle tissue extension in the central muscle region is depicted in the background as reddish round shape. Mean SNR values are shown as horizontal bars with corresponding numbers next to it. Left and right halves correspond to muscles shown in (C,F), respectively. 57

Figure 27 - MYOCLEAR enables imaging of muscle fibers and myonuclei by using red autofluorescence and far-red wavelengths dyes. Mouse EDL was processed via the MYOCLEAR protocol and stained with BGT-AF555 and Draq5. (A) depicts a confocal section of the EDL, with (B) representing a zoom of the boxed region. Strong autofluorescence of the tissue in the AF555 channel (green) resulted in a poor signal to noise ratio for NMJ detection (some NMJs are highlighted in B, arrowheads). In contrast, the near-infrared dye Draq5 displayed crisp and clear nuclei. 58

Figure 28 - Spectral un-mixing together with MYOCLEAR allows NMJ and nuclei whole-muscle imaging in near-infrared wavelengths. Mouse EDL muscle was processed via the MYOCLEAR protocol and stained with BGT-AF647 and Draq5. In order to overcome the auto-fluorescence shown in Figure 27, the emission windows for each dye were adjusted according to their peak values and acquired separately using the same 633-nm excitation laser on a SP8 confocal microscope. The images were processed using Leica Las-X core software and spectrally un-mixed in ImageJ. (A) Maximum-z projection of the whole EDL before applying spectral un-mixing. Draq5, red; BGT-AF647, green. Green autofluorescence of the thread keeping the muscle in place for imaging is visible at the proximal and distal ends of the muscle. (B) Zoom view of the boxed region in A. (C-D) BGT-647 channel data as shown in A before (C) and after (D) spectral un-mixing. (E-F) Z-axis depth coding for signals of BGT-AF647 (E) and Draq5 (F) shown as cross sections after spectral un-mixing. 59

Figure 29 - MYOCLEAR is functional with adult mouse diaphragm muscle. Adult mouse diaphragm muscles were processed using the MYOCLEAR protocol and stained with Draq5 and BGT-AF647. (A) Maximum-z projection of a representative tile stack showing fluorescence signals of BGT and Draq5 in green and red, respectively. Note, that NMJs are not fragmented but partially covered by myonuclei. This is evident in the insert, which shows only BGT signals of a small region. (B) Side view to show depth extension of fluorescence signals. The entire depth of around 500 μm of the diaphragm became transparent. (C,D) Depth coded side views of nuclear (C) and NMJ signals (D). Pseudocolor code is explained on the right side. 60

Figure 30 - Analysis of whole mount NMJ morphology and quantification of NMJ numbers is enabled in wildtype and MDX muscles upon clearing. EDL muscles from wildtype (A,A',C,D) and dystrophic MDX mice (B,B',E,F) were processed using the MYOCLEAR protocol and stained with BGT-AF647. (A,B) Maximum-z projections of all NMJs detected by hand segmentation. Each cyan spot represents a single NMJ. (A',B') High-power images of some representative NMJs from each muscle shown in (A,B). (C,E) Upper panels, maximum-z projections of representative muscles showing BGT-staining signals. Lower panels, high power display of ROIs 1–5 in corresponding upper panel. (D,F) Quantitative analysis of key morphological parameters: area, fragmentation index, perimeter, and bounding rectangle diagonal of NMJs. Depicted are mean \pm SD for all en face NMJs detected as a function of ROI number. * $p < 0.05$, ** $p \leq 0.01$, *** $p \leq 0.001$, **** $p \leq 0.0001$ 61

Figure 31 - Integrity of NMJ presynapse and other muscle structures is maintained upon clearing. Adult mouse EDL muscles were processed using the MYOCLEAR protocol and co-stained with Draq5 and antibodies against either NMJ presynapse (A, vAChT), sarcolemma (B, dystrophin), ECM (C, collagen I), or sarcomere (D, troponin I). Images show maximum-z projections of confocal z-stacks with an interplane interval of 2 μm and depths from muscle surface of 466, 665, 104, and 214 μm for (A–D), respectively. 63

Figure 32 - Comparison of different acrylamide fixation techniques. A4P0B0.05 qualitatively displayed better retention of both blood vessels as well as nuclei when compared to A4P0B0 fixed samples. Freshly dissected adult mouse EDL muscles were incubated in either (A-C) 4% acrylamide, 0.05% bis-acrylamide, and 0.25% VA-044 activator (A4P0B0.05) or (D-F) 4% acrylamide and 0.25% VA-044 (A4P0B0) for five days at 4 $^{\circ}\text{C}$ on a roller mixer. Samples were then polymerized at 37 $^{\circ}\text{C}$ for four hours, washed overnight, blocked for two days with BnP, and stained with (A,D) mouse secondary antibody (488), (B,E) BGT-555, and (C,F) DRAQ5. $n = 2$, scale bar = 100 μm . In addition, mouse tibialis anterior muscles fixed with (G) A4P0B0.05 displayed considerably less fixation induced browning, when compared to (H) traditional PFA fixation. 65

Figure 33 – Effects of various concentrations of PFA, acrylamide, bis-acrylamide, and activator on protein loss. Freshly dissected adult mouse EDL muscles were incubated for five days at 4 $^{\circ}\text{C}$ on a roller mixer in various concentrations of PFA, acrylamide, bis-acrylamide, and activator, as listed in the figure legend. Samples were then polymerized at 37 $^{\circ}\text{C}$ for four hours, washed overnight, and then placed in 2 ml eppies. 2 ml of 1x PtWH was then added to each and eppies put in light protected, brown falcon tubes. Samples were then kept on a roller mixer at room temperature. Aliquots were then taken at day 0, 1, 3, 5, 14, and 35 and analyzed using the pierce 660 nm protein assay. No matter the fixation conditions, no samples were above the LOD after 35 days. PFA = PFA (%), A = Acrylamide (%), B = Bis-acrylamide (%), and I = VA-044 (mg). $n = 3$ for all groups 66

Figure 34 - Urea improves signal clarity in MYOCLEAR+ processed samples. Freshly dissected adult mouse EDL muscles were fixed and stained with DRAQ5 following the MYOCLEAR+ protocol. EDLs were then incubated in either (A) glycerol 88% or (B) 88% glycerol + 2 M urea for two days and imaged with light sheet using a Leica SP8 DLS microscope. (A,B) depict the quality and clarity differences muscles portrayed at an equal depth into the muscle. Scale bar = 50 μm 67

Figure 35 – MYOCLEAR+ with DIMM enable the use of the lower wavelength channels for light sheet acquisition. Freshly dissected adult mouse EDL muscles were fixed and stained with NF-488, CD-31-546, and BGT-647 following the MYOCLEAR+ protocol. EDLs were then incubated in DIMM for up to two weeks and imaged with light sheet using a Leica SP8 DLS microscope. (A-C) are representative images from the belly of the EDL, where (A) are motor neurons stained with NF-488, (B) are blood vessels stained with CD-31-546, and (C) is a merge of both channels. (D,E) are representative images of a distal, smaller section of the EDL with (D) depicting a depth view of NF-488 and CD-31-546 and (E) a merge of this section. Scale bar = (A,B) 200 μm , (C) 1 mm, (E) 500 μm 68

Figure 36 – Effects of pH and urea on the retention of BGT fluorescence. Adult mouse diaphragms were freshly dissected and fixed with 4% PFA for 5 minutes on a roller mixer at RT. Diaphragms were then cut into sections and stained with BGT-555 following the MYOCLEAR staining protocol. Each section was then incubated in either (A,D) 88% glycerol, (B,E) pH adjusted DIMM without urea, and (C,F) with urea. After 3 days, diaphragm sections were imaged with (A-C) depicting a top view as well as their corresponding depths (D-F). Scale bar = 200 μm 69

Figure 37 – MYOCLEAR+ with DIMM enables deep imaging of brain tissue. Freshly dissected adult mouse brain samples were fixed and stained with (A) CD-31-647 and (B) NF-488 following the MYOCLEAR+ protocol. Samples were then incubated in DIMM for up to one week, cut into smaller sections in order to fit between the mirrors, and imaged with light sheet using a Leica SP8 DLS. Although MYOCLEAR+ in combination with DIMM for RI matching impressively exhibited no issue imaging the full Z depth range of 1.5 mm, we found the samples more fragile and easier to damage compared to other tissues, with accidental damage caused by a pair of forceps while mounting the sample indicated by the arrow heads. 70

Figure 38 – MYOCLEAR+ with DIMM enables deep tissue imaging in the spleen. Freshly dissected adult mouse spleen samples were fixed and stained with CD-169-AF647, for visualizing CD169 positive macrophages located in the splenic marginal zone, following the MYOCLEAR+ protocol. Samples were then incubated in DIMM for up to one week, cut into smaller sections in order to fit between the mirrors, and imaged with light sheet using a Leica SP8 DLS. (A) depicts a top view with its (B) corresponding depth coded view. 71

Figure 39 – Adjusting the treatment regimen from every 12 hours post-intervention to 16 hours led to an extension of the septic state in mice. Mice were administered a lethal, 200 μl dose of CS IP for the induction of sepsis. 10 hours post-insult, intervention with 300 μl IPM and 700 μl saline was started and readministered SC every (black) 12 or (blue) 16 hours and the septic state of the mice evaluated at 2, 4, 6, 8, 10 and every 16 hours thereafter based on the MSS scoring system. We found that delaying treatment by 4 hours resulted in an extension of the septic state by roughly 48 hours, when compared to treatment every 12 hours, and an optimal mortality rate of 25%. n = 5 for the 12 hours group and n = 20 for the 16 hour group..... 72

Figure 40 - Bacterial load assessment of septic mice. Bacterial load of the (A) blood, (B) liver, and (C) spleen at 6 hours, 24 hours (with and without treatment), and 7 days post-insult. Mice were administered a lethal, 200 μ l dose of CS IP for the induction of sepsis. 10 hours post-insult, intervention with 300 μ l IPM and 700 μ l saline was started and readministered every 16 hours for the 24 hour (with treatment) and 7 day groups, with no intervention administered in an additional 24 hour group (denoted as “24 hr no AB”). Mice were sacrificed at each time point and blood, liver, and spleen samples collected, homogenized, and plated on blood agar plates in duplicates. Plates were then incubated for 24 hours and CFU manually counted for each. * $p < 0.05$, ** $p \leq 0.01$, *** $p \leq 0.001$, **** $p \leq 0.0001$ 73

Figure 41 – Plasma analysis of control and septic mice. Plasma analysis of (A) Lactate, (B) Glucose, (C) Urea, (D) ALT, (E) AST, and (F) Creatinine. Mice were administered a lethal, 200 μ l dose of CS IP for the induction of sepsis. 10 hours post-insult, intervention with 300 μ l IPM and 700 μ l saline was started and readministered every 16 hours for the 24 hour (with treatment) and 7 day groups, with no intervention administered in an additional 24 hour group (denoted as “24 hr no AB”). Blood was then collected from the orbital sinus of anaesthetized mice and placed in Heparin collection tubes. Then, tubes were centrifuged, the supernatant collected, and transferred into 1.5 ml eppies. Plasma was then stored at -20 °C and analyzed within two weeks from the collection date. $n = 10$ for all control and 24 hour with treatment groups, $n = 9$ for all 24 hour without treatment groups, $n = 8$ for lactate and glucose 6 hour and 7 day groups; ALT, AST, urea, and creatinine 7 day groups, $n = 7$ for ALT, AST, and urea 6 hour groups, and $n = 6$ for creatinine 6 hour group. * $p < 0.05$, ** $p \leq 0.01$, *** $p \leq 0.001$, **** $p \leq 0.0001$ 74

Figure 42 - Cytokine analysis reveals an exaggerated response to a cecal slurry sepsis insult. Mice were given 200 μ l IP injection of cecal slurry, with antibiotics and fluids administered 10 hours post-injection and every 16 hours thereafter. Then blood was collected, as before, in EDTA tubes, centrifuged, the supernatant collected, and cytokines quantified in duplicate on a MILLIPLEX map mouse cytokine/chemokine magnetic bead panel. $n = 10$ for the control group and $n = 7$ for both 24 hour groups as well as the 7 day group. * $p < 0.05$, ** $p \leq 0.01$, *** $p \leq 0.001$, **** $p \leq 0.0001$ 75

Figure 43 - Tracking of mouse activity levels over the course of sepsis. (A) represents the overall activity level of septic mice over a seven day period, while (B) depicts the nightly activity level of mice in relation to control levels. Video recordings of control and septic mice were collected using a Flir A655sc infrared camera. Then, videos were broken into hours, processed, and segmented using the WrTrk ImageJ plugin. After segmentation, hourly data was divided by the amount of mice left in the cage at that time point. Nightly activity levels were calculated using the first 8 hours of activity per night $n = 10$ for septic mice and $n = 15$ for control **** $p \leq 0.0001$ 76

Figure 44 – Sepsis causes a reduction of both diaphragm width and fiber diameter. Sepsis contributed to a reduction in both (A) width and (B) fiber diameter of the diaphragm. Mouse hemidiaphragms from septic and control groups were PFA fixed, stained with BGT, and imaged on an inverted Leica SP8. The acquired images were then stitched, rotated 90°, and diaphragm width and fiber diameter analyzed by hand within the NMJ band region. $N = 3$ for both groups * $p < 0.05$ 77

Figure 45 - Sepsis leads to a transient upregulation of MuRF1 and the UPS. (left) representative western blots of MyBP-C, α -Actinin, Murf1, Multi Ubiquitin, and ANKRD1, with (right) their relative ratios normalized to GAPDH. The UPS was found to be upregulated

via increases in both Murf1 and multi-ubiquitin, though, key structural proteins (MyBP-C and α -actinin) seemed relatively unaffected. Whole mouse diaphragms from control, 24 hour post-insult with no intervention, and 7 days were freshly dissected, placed into cryotubes, snap frozen in liquid nitrogen, and stored at -80°C . Samples were then transferred into 2 ml eppies, an equal amount of lysis buffer added to each, and lysed for 3 minutes at 30 Hz. Samples were then centrifuged and the super natant collected, aliquoted, and stored at -80°C . $n = 3$ for all groups * $p < 0.05$, ** $p \leq 0.01$ 78

Figure 46 – Loss of SNS in the diaphragm may contribute to NMJ instability in sepsis.

Sepsis resulted in a decreasing trend of SNS tone within the diaphragm, as well as significant denervation by the seventh day. (left) representative western blots of TH, ADRB2, Rab5, CDK5, NCAM, and ANKRD2 with (right) their relative ratios normalized to GAPDH. Whole mouse diaphragms from control, 24 hour post-insult with no intervention, and 7 days were freshly dissected, placed into cryotubes, snap frozen in liquid nitrogen, and stored at -80°C . Samples were then transferred into 2 ml eppies, an equal amount of lysis buffer added to each, and lysed for 3 minutes at 30 Hz. Samples were then centrifuged and the super natant collected, aliquoted, and stored at -80°C . $n = 2$ for TH, ADRB2, Rab5, and NCAM control groups and $n = 3$ for all other groups * $p < 0.05$, ** $p \leq 0.01$, *** $p \leq 0.001$ 79

Figure 47 – Sepsis results in an upregulation of the fibrosis pathway. Sepsis resulted in a significant increase in key pro-fibrotic proteins, SMAD2 and SMAD3. (left) representative western blots of β -actin, α -Tubulin, SMAD2, SMAD3, and YAP with (right) their relative ratios normalized to GAPDH. Whole mouse diaphragms from control, 24 hour post-insult with no intervention, and 7 days were freshly dissected, placed into cryotubes, snap frozen in liquid nitrogen, and stored at -80°C . Samples were then transferred into 2 ml eppies, an equal amount of lysis buffer added to each, and lysed for 3 minutes at 30 Hz. Samples were then centrifuged and the super natant collected, aliquoted, and stored at -80°C . $n = 3$ for all groups * $p < 0.05$, ** $p \leq 0.01$, *** $p \leq 0.001$ 80

Figure 48 – Sepsis leads to the expression of eMHC by the seventh day post-septic insult.

Mouse hemidiaphragms from seven days post-insult septic mice were PFA fixed, stained with BGT-AF555 and eMHC-AF647, and imaged on an inverted Leica SP8, as before. We found many regenerating muscle fibers (A) by seventh day post-insult. Furthermore, (B) NMJs located in this region qualitatively exhibited extremely weak signals, compared to NMJs located outside of this region at the same depth into the tissue. Scale bar = (A) 100 μm , (B) 50 μm 80

Figure 49 - Comparison of emission and excitation profiles of AF647, DRAQ5, and PE-Cy7. Excitation and emission (A) comparison of AF647 and DRAQ5 and (B) AF647 and PE-Cy7. Images were created using ThermoFisher Scientific's fluorescence spectraviewer. 83

8. References

- Ahrenholz, D. H. and R. L. Simmons (1980). "Fibrin in peritonitis. I. Beneficial and adverse effects of fibrin in experimental *E. coli* peritonitis." *Surgery* **88**(1): 41-47.
- Alberti, C., C. Brun-Buisson, H. Burchardi, C. Martin, S. Goodman, A. Artigas, A. Sicignano, M. Palazzo, R. Moreno, R. Boulmé, E. Lepage and R. Le Gall (2002). "Epidemiology of sepsis and infection in ICU patients from an international multicentre cohort study." *Intensive Care Med* **28**(2): 108-121.
- Alexander, J. W., S. J. Gonce, P. W. Miskell, M. D. Peck and H. Sax (1989). "A new model for studying nutrition in peritonitis. The adverse effect of overfeeding." *Ann Surg* **209**(3): 334-340.
- Alverdy, J. C., R. Keskey and R. Thewissen (2020). "Can the Cecal Ligation and Puncture Model Be Repurposed To Better Inform Therapy in Human Sepsis?" *Infect Immun* **88**(9).
- Angus, D. C., W. T. Linde-Zwirble, J. Lidicker, G. Clermont, J. Carcillo and M. R. Pinsky (2001). "Epidemiology of severe sepsis in the United States: analysis of incidence, outcome, and associated costs of care." *Crit Care Med* **29**(7): 1303-1310.
- Aoyagi, Y., R. Kawakami, H. Osanai, T. Hibi and T. Nemoto (2015). "A rapid optical clearing protocol using 2,2'-thiodiethanol for microscopic observation of fixed mouse brain." *PLoS One* **10**(1): e0116280.
- Ariel, P. (2017). "A beginner's guide to tissue clearing." *Int J Biochem Cell Biol* **84**: 35-39.
- Azaripour, A., T. Lagerweij, C. Scharfbillig, A. E. Jadcak, B. Willershausen and C. J. Van Noorden (2016). "A survey of clearing techniques for 3D imaging of tissues with special reference to connective tissue." *Prog Histochem Cytochem* **51**(2): 9-23.
- Becker, K., N. Jährling, S. Saghafi, R. Weiler and H. U. Dodt (2012). "Chemical clearing and dehydration of GFP expressing mouse brains." *PLoS One* **7**(3): e33916.
- Bisby, M. A. and W. Tetzlaff (1992). "Changes in cytoskeletal protein synthesis following axon injury and during axon regeneration." *Molecular Neurobiology* **6**(2): 107-123.
- Bloos, F. (2018). "Diagnosis and therapy of sepsis." *Journal of Emergency and Critical Care Medicine* **2**(1).
- Boland, M., L. Kaur, F. M. Chian and T. Astruc (2018). Muscle Proteins. *Reference Module in Food Science*: np.
- Bone, R. C., W. J. Sibbald and C. L. Sprung (1992). "The ACCP-SCCM consensus conference on sepsis and organ failure." *Chest* **101**(6): 1481-1483.
- Brealey, D., S. Karyampudi, T. S. Jacques, M. Novelli, R. Stidwill, V. Taylor, R. T. Smolenski and M. Singer (2004). "Mitochondrial dysfunction in a long-term rodent model of sepsis and organ failure." *Am J Physiol Regul Integr Comp Physiol* **286**(3): R491-497.
- Brun-Buisson, C. (2000). "The epidemiology of the systemic inflammatory response." *Intensive Care Med* **26 Suppl 1**(Suppl 1): S64-74.
- Buchman, T. G., S. Q. Simpson, K. L. Sciarretta, K. P. Finne, N. Sowers, M. Collier, S. Chavan, I. Oke, M. E. Pennini, A. Santhosh, M. Wax, R. Woodbury, S. Chu, T. G. Merkeley, G. L. Disbrow, R. A. Bright, T. E. MaCurdy and J. A. Kelman (2020). "Sepsis Among Medicare Beneficiaries: 1. The Burdens of Sepsis, 2012-2018." *Crit Care Med* **48**(3): 276-288.
- Buras, J. A., B. Holzmann and M. Sitkovsky (2005). "Animal models of sepsis: setting the stage." *Nat Rev Drug Discov* **4**(10): 854-865.
- Callahan, L. A. and G. S. Supinski (2009). "Sepsis-induced myopathy." *Crit Care Med* **37**(10 Suppl): S354-367.
- Chaudhry, H., J. Zhou, Y. Zhong, M. M. Ali, F. McGuire, P. S. Nagarkatti and M. Nagarkatti (2013). "Role of cytokines as a double-edged sword in sepsis." *In Vivo* **27**(6): 669-684.
- Chousterman, B. G., F. K. Swirski and G. F. Weber (2017). "Cytokine storm and sepsis disease pathogenesis." *Semin Immunopathol* **39**(5): 517-528.

- Chung, K. and K. Deisseroth (2013). "CLARITY for mapping the nervous system." Nat Methods **10**(6): 508-513.
- Chung, K., J. Wallace, S. Y. Kim, S. Kalyanasundaram, A. S. Andalman, T. J. Davidson, J. J. Mirzabekov, K. A. Zalocusky, J. Mattis, A. K. Denisin, S. Pak, H. Bernstein, C. Ramakrishnan, L. Grosenick, V. Gradinaru and K. Deisseroth (2013). "Structural and molecular interrogation of intact biological systems." Nature **497**(7449): 332-337.
- Clancy, B. and L. J. Cauller (1998). "Reduction of background autofluorescence in brain sections following immersion in sodium borohydride." J Neurosci Methods **83**(2): 97-102.
- Clark, K. A., A. S. McElhinny, M. C. Beckerle and C. C. Gregorio (2002). "Striated muscle cytoarchitecture: an intricate web of form and function." Annu Rev Cell Dev Biol **18**: 637-706.
- Claxton, N. S., T. Fellers and M. Davidson (2005). LASER SCANNING CONFOCAL MICROSCOPY.
- Clowes, G. H., Jr., W. Zuschneid, M. Turner, G. Blackburn, J. Rubin, P. Toala and G. Green (1968). "Observations on the pathogenesis of the pneumonitis associated with severe infections in other parts of the body." Ann Surg **167**(5): 630-650.
- Collins, J. S. and T. H. Goldsmith (1981). "Spectral properties of fluorescence induced by glutaraldehyde fixation." J Histochem Cytochem **29**(3): 411-414.
- Conchello, J. A. and J. W. Lichtman (2005). "Optical sectioning microscopy." Nat Methods **2**(12): 920-931.
- Cranfill, P. J., B. R. Sell, M. A. Baird, J. R. Allen, Z. Lavagnino, H. M. de Gruiter, G. J. Kremers, M. W. Davidson, A. Ustione and D. W. Piston (2016). "Quantitative assessment of fluorescent proteins." Nat Methods **13**(7): 557-562.
- Cross, A. S., S. M. Opal, J. C. Sadoff and P. Gemski (1993). "Choice of bacteria in animal models of sepsis." Infect Immun **61**(7): 2741-2747.
- Cryan, J. F. and C. Mombereau (2004). "In search of a depressed mouse: utility of models for studying depression-related behavior in genetically modified mice." Molecular Psychiatry **9**(4): 326-357.
- Cummings, M., J. Sarveswaran, S. Homer-Vanniasinkam, D. Burke and N. M. Orsi (2014). "Glyceraldehyde-3-phosphate dehydrogenase is an inappropriate housekeeping gene for normalising gene expression in sepsis." Inflammation **37**(5): 1889-1894.
- Decroix, L., V. Van Muylder, L. Desender, M. Sampaolesi and L. Thorrez (2015). "Tissue clearing for confocal imaging of native and bio-artificial skeletal muscle." Biotech Histochem **90**(6): 424-431.
- Denk, W. and H. Horstmann (2004). "Serial block-face scanning electron microscopy to reconstruct three-dimensional tissue nanostructure." PLoS Biol **2**(11): e329.
- Dodart, J. C., H. Meziane, C. Mathis, K. R. Bales, S. M. Paul and A. Ungerer (1999). "Behavioral disturbances in transgenic mice overexpressing the V717F beta-amyloid precursor protein." Behav Neurosci **113**(5): 982-990.
- Dotd, H.-U., U. Leischner, A. Schierloh, N. Jährling, C. P. Mauch, K. Deininger, J. M. Deussing, M. Eder, W. Zieglgänsberger and K. Becker (2007). "Ultramicroscopy: three-dimensional visualization of neuronal networks in the whole mouse brain." Nature Methods **4**(4): 331-336.
- Drewry, A. M. and R. S. Hotchkiss (2015). "Revising definitions of sepsis." Nature Reviews Nephrology **11**(6): 326-328.
- Duong, H. and M. Han (2013). "A multispectral LED array for the reduction of background autofluorescence in brain tissue." J Neurosci Methods **220**(1): 46-54.
- Dyson, A. and M. Singer (2009). "Animal models of sepsis: why does preclinical efficacy fail to translate to the clinical setting?" Crit Care Med **37**(1 Suppl): S30-37.
- Ebert, S. M., A. Al-Zougbi, S. C. Bodine and C. M. Adams (2019). "Skeletal Muscle Atrophy: Discovery of Mechanisms and Potential Therapies." Physiology **34**(4): 232-239.

- Ertürk, A., K. Becker, N. Jährling, C. P. Mauch, C. D. Hojer, J. G. Egen, F. Hellal, F. Bradke, M. Sheng and H.-U. Dodt (2012). "Three-dimensional imaging of solvent-cleared organs using 3DISCO." Nature Protocols **7**(11): 1983-1995.
- Fahrbach, F. and W. Knebel (2019). Method for examining a sample by means of light sheet microscopy, and light sheet microscope, U.S. Patent Application No. 16/064,533.
- Ferreira, J. A. and B. D. Bissell (2018). "Misdirected Sympathy: The Role of Sympatholysis in Sepsis and Septic Shock." Journal of Intensive Care Medicine **33**(2): 74-86.
- Fink, M. P. (2014). "Animal models of sepsis." Virulence **5**(1): 143-153.
- Fink, M. P. and S. O. Heard (1990). "Laboratory models of sepsis and septic shock." Journal of Surgical Research **49**(2): 186-196.
- Fleischmann, C., M. Hartmann, C. S. Hartog, T. Welte, S. Heublein, D. Thomas-Rueddel, U. Dennler and K. Reinhart (2015). "Epidemiology of Sepsis in Germany: Incidence, Mortality And Associated Costs of Care 2007-2013." Intensive Care Med **Exp** **3**(Suppl 1).
- Françon, M. (1961). Progress in microscopy. Oxford, New York,, Pergamon Press.
- Friedrich, O., M. B. Reid, G. Van den Berghe, I. Vanhorebeek, G. Hermans, M. M. Rich and L. Larsson (2015). "The Sick and the Weak: Neuropathies/Myopathies in the Critically Ill." Physiol Rev **95**(3): 1025-1109.
- Frye, E. B., T. P. Degenhardt, S. R. Thorpe and J. W. Baynes (1998). "Role of the Maillard reaction in aging of tissue proteins. Advanced glycation end product-dependent increase in imidazolium cross-links in human lens proteins." J Biol Chem **273**(30): 18714-18719.
- Garg, B. K. and R. H. Loring (2017). "Evaluating Commercially Available Antibodies for Rat $\alpha 7$ Nicotinic Acetylcholine Receptors." J Histochem Cytochem **65**(9): 499-512.
- Geesink, H. J. and D. K. Meijer (2018). "Mathematical structure for electromagnetic frequencies that may reflect pilot waves of Bohm's implicate order." Journal of Modern Physics **9**(05): 851.
- Giboney, P. T. (2005). "Mildly elevated liver transaminase levels in the asymptomatic patient." Am Fam Physician **71**(6): 1105-1110.
- Girkin, J. M. and M. T. Carvalho (2018). "The light-sheet microscopy revolution." Journal of Optics **20**(5): 053002.
- Gonnert, F. A., P. Recknagel, M. Seidel, N. Jbeily, K. Dahlke, C. L. Bockmeyer, J. Winning, W. Losche, R. A. Claus and M. Bauer (2011). "Characteristics of clinical sepsis reflected in a reliable and reproducible rodent sepsis model." J Surg Res **170**(1): e123-134.
- Guo, Y., W. Gao, H. Yang, C. e. Ma and S. Sui (2016). "De-escalation of empiric antibiotics in patients with severe sepsis or septic shock: A meta-analysis." Heart & Lung **45**(5): 454-459.
- Gyawali, B., K. Ramakrishna and A. S. Dhmoon (2019). "Sepsis: The evolution in definition, pathophysiology, and management." SAGE Open Med **7**: 2050312119835043.
- Hagberg, L., I. Engberg, R. Freter, J. Lam, S. Olling and C. Svanborg Edén (1983). "Ascending, unobstructed urinary tract infection in mice caused by pyelonephritogenic Escherichia coli of human origin." Infect Immun **40**(1): 273-283.
- Hama, H., H. Kurokawa, H. Kawano, R. Ando, T. Shimogori, H. Noda, K. Fukami, A. Sakaue-Sawano and A. Miyawaki (2011). "Scale: a chemical approach for fluorescence imaging and reconstruction of transparent mouse brain." Nature Neuroscience **14**(11): 1481-1488.
- Han, B. G., C.-M. Hao, E. E. Tchekneva, Y.-Y. Wang, C. A. Lee, B. Ebrahim, R. C. Harris, T. S. Kern, D. H. Wasserman, M. D. Breyer and Z. Qi (2008). "Markers of glycemic control in the mouse: comparisons of 6-h- and overnight-fasted blood glucoses to Hb A1c." American Journal of Physiology-Endocrinology and Metabolism **295**(4): E981-E986.
- Haskó, G. and C. Szabó (1998). "Regulation of cytokine and chemokine production by transmitters and co-transmitters of the autonomic nervous system." Biochemical Pharmacology **56**(9): 1079-1087.
- Hearse, D. J. (1997). "Myocardial hibernation. A form of endogenous protection?" Eur Heart J **18 Suppl A**: A2-7.

- Hecht, E. (2002). *Optics*. Reading, Mass., Addison-Wesley.
- Holcomb, L. A., M. N. Gordon, P. Jantzen, K. Hsiao, K. Duff and D. Morgan (1999). "Behavioral changes in transgenic mice expressing both amyloid precursor protein and presenilin-1 mutations: lack of association with amyloid deposits." *Behav Genet* **29**(3): 177-185.
- Hooijman, P. E., A. Beishuizen, C. C. Witt, M. C. de Waard, A. R. Girbes, A. M. Spoelstra-de Man, H. W. Niessen, E. Manders, H. W. van Hees, C. E. van den Brom, V. Silderhuis, M. W. Lawlor, S. Labeit, G. J. Stienen, K. J. Hartemink, M. A. Paul, L. M. Heunks and C. A. Ottenheijm (2015). "Diaphragm muscle fiber weakness and ubiquitin-proteasome activation in critically ill patients." *Am J Respir Crit Care Med* **191**(10): 1126-1138.
- Hoover, D. B., T. C. Brown, M. K. Miller, J. B. Schweitzer and D. L. Williams (2017). "Loss of Sympathetic Nerves in Spleens from Patients with End Stage Sepsis." *Front Immunol* **8**: 1712.
- Hotchkiss, R. S., P. E. Swanson, B. D. Freeman, K. W. Tinsley, J. P. Cobb, G. M. Matuschak, T. G. Buchman and I. E. Karl (1999). "Apoptotic cell death in patients with sepsis, shock, and multiple organ dysfunction." *Crit Care Med* **27**(7): 1230-1251.
- Hou, B., D. Zhang, S. Zhao, M. Wei, Z. Yang, S. Wang, J. Wang, X. Zhang, B. Liu, L. Fan, Y. Li, Z. Qiu, C. Zhang and T. Jiang (2015). "Scalable and DiI-compatible optical clearance of the mammalian brain." *Front Neuroanat* **9**: 19.
- Huang, J., C. Brenna, A. u. M. Khan, C. Daniele, R. Rudolf, V. Heuveline and N. Gretz (2019). "A cationic near infrared fluorescent agent and ethyl-cinnamate tissue clearing protocol for vascular staining and imaging." *Scientific Reports* **9**(1): 521.
- Ichimura, K., N. Miyazaki, S. Sadayama, K. Murata, M. Koike, K. Nakamura, K. Ohta and T. Sakai (2015). "Three-dimensional architecture of podocytes revealed by block-face scanning electron microscopy." *Sci Rep* **5**: 8993.
- Imamura, M. and G. H. Clowes, Jr. (1975). "Hepatic blood flow and oxygen consumption in starvation, sepsis and septic shock." *Surg Gynecol Obstet* **141**(1): 27-34.
- Ito, T., N. Fujimura, K. Omote and A. Namiki (2006). "A selective beta2-adrenergic agonist, terbutaline, improves sepsis-induced diaphragmatic dysfunction in the rat." *Life Sci* **79**(9): 905-912.
- Jackman, R. W. and S. C. Kandarian (2004). "The molecular basis of skeletal muscle atrophy." *Am J Physiol Cell Physiol* **287**(4): C834-843.
- Johnson, L. V. and J. C. Blanks (1984). "Application of acrylamide as an embedding medium in studies of lectin and antibody binding in the vertebrate retina." *Current Eye Research* **3**(7): 969-974.
- Jones, R. A., C. D. Reich, K. N. Dissanayake, F. Kristmundsdottir, G. S. Findlater, R. R. Ribchester, M. W. Simmen and T. H. Gillingwater (2016). "NMJ-morph reveals principal components of synaptic morphology influencing structure-function relationships at the neuromuscular junction." *Open Biol* **6**(12).
- Jung, B., S. Nougaret, M. Conseil, Y. Coisel, E. Futier, G. Chanques, N. Molinari, A. Lacampagne, S. Matecki and S. Jaber (2014). "Sepsis Is Associated with a Preferential Diaphragmatic Atrophy: A Critically Ill Patient Study Using Tridimensional Computed Tomography." *Anesthesiology* **120**(5): 1182-1191.
- Ke, M.-T., S. Fujimoto and T. Imai (2013). "SeeDB: a simple and morphology-preserving optical clearing agent for neuronal circuit reconstruction." *Nature Neuroscience* **16**(8): 1154-1161.
- Ke, M. T., Y. Nakai, S. Fujimoto, R. Takayama, S. Yoshida, T. S. Kitajima, M. Sato and T. Imai (2016). "Super-Resolution Mapping of Neuronal Circuitry With an Index-Optimized Clearing Agent." *Cell Rep* **14**(11): 2718-2732.
- Kell, D. and E. Pretorius (2017). "To What Extent Are the Terminal Stages of Sepsis, Septic Shock, Systemic Inflammatory Response Syndrome, and Multiple Organ Dysfunction

Syndrome Actually Driven by a Prion/Amyloid Form of Fibrin?" Seminars in Thrombosis and Hemostasis **44**.

Khalil, R. (2018). Ubiquitin-Proteasome Pathway and Muscle Atrophy. Muscle Atrophy. J. Xiao. Singapore, Springer Singapore: 235-248.

Khan, M. M., D. Lustrino, W. A. Silveira, F. Wild, T. Straka, Y. Issop, E. O'Connor, D. Cox, M. Reischl, T. Marquardt, D. Labeit, S. Labeit, E. Benoit, J. Molgó, H. Lochmüller, V. Witzemann, I. C. Kettelhut, L. C. Navegantes, T. Pozzan and R. Rudolf (2016). "Sympathetic innervation controls homeostasis of neuromuscular junctions in health and disease." Proc Natl Acad Sci U S A **113**(3): 746-750.

Kim, S. Y., J. H. Cho, E. Murray, N. Bakh, H. Choi, K. Ohn, L. Ruelas, A. Hubbert, M. McCue, S. L. Vassallo, P. J. Keller and K. Chung (2015). "Stochastic electrotransport selectively enhances the transport of highly electromobile molecules." Proc Natl Acad Sci U S A **112**(46): E6274-6283.

Kondzior, M. and I. Grabowska (2020). "Antibody-Electroactive Probe Conjugates Based Electrochemical Immunosensors." Sensors (Basel) **20**(7).

Korneev, K. V. (2019). "[Mouse Models of Sepsis and Septic Shock]." Mol Biol (Mosk) **53**(5): 799-814.

Krans, J. L. (2010). "The sliding filament theory of muscle contraction." Nature Education **3**(9): 66.

Lai, H. M., A. K. Liu, W. L. Ng, J. DeFelice, W. S. Lee, H. Li, W. Li, H. M. Ng, R. C. Chang, B. Lin, W. Wu and S. M. Gentleman (2016). "Rationalisation and Validation of an Acrylamide-Free Procedure in Three-Dimensional Histological Imaging." PLoS One **11**(6): e0158628.

Lang, C. H., R. A. Frost and T. C. Vary (2007). "Regulation of muscle protein synthesis during sepsis and inflammation." Am J Physiol Endocrinol Metab **293**(2): E453-459.

Latronico, N., M. Filosto, N. Fagoni, L. Gheza, B. Guarneri, A. Todeschini, R. Lombardi, A. Padovani and G. Lauria (2013). "Small nerve fiber pathology in critical illness." PLoS One **8**(9): e75696.

Laure, L., L. Suel, C. Roudaut, N. Bourg, A. Ouali, M. Bartoli, I. Richard and N. Danièle (2009). "Cardiac ankyrin repeat protein is a marker of skeletal muscle pathological remodelling." The FEBS Journal **276**(3): 669-684.

Lee, E., J. Choi, Y. Jo, J. Y. Kim, Y. J. Jang, H. M. Lee, S. Y. Kim, H. J. Lee, K. Cho, N. Jung, E. M. Hur, S. J. Jeong, C. Moon, Y. Choe, I. J. Rhyu, H. Kim and W. Sun (2016). "ACT-RESTO: Rapid and consistent tissue clearing and labeling method for 3-dimensional (3D) imaging." Sci Rep **6**: 18631.

Lee, G. D. and H. C. Kim (2010). "Mechanisms of Muscle Wasting in Patients with Sepsis." Korean J Crit Care Med **25**(1): 9-15.

Legesse, F. B., O. Chernavskaia, S. HEUKE, T. BOCKLITZ, T. MEYER, J. POPP and R. HEINTZMANN (2015). "Seamless stitching of tile scan microscope images." Journal of Microscopy **258**(3): 223-232.

Levy, M. M., M. P. Fink, J. C. Marshall, E. Abraham, D. Angus, D. Cook, J. Cohen, S. M. Opal, J. L. Vincent and G. Ramsay (2003). "2001 SCCM/ESICM/ACCP/ATS/SIS International Sepsis Definitions Conference." Crit Care Med **31**(4): 1250-1256.

Lewis, A. J., C. W. Seymour and M. R. Rosengart (2016). "Current Murine Models of Sepsis." Surg Infect (Larchmt) **17**(4): 385-393.

Lichtman, J. W. and J. A. Conchello (2005). "Fluorescence microscopy." Nat Methods **2**(12): 910-919.

Liu, J., D. Saul, K. O. Böker, J. Ernst, W. Lehman and A. F. Schilling (2018). "Current Methods for Skeletal Muscle Tissue Repair and Regeneration." Biomed Res Int **2018**: 1984879.

Lopatina, O., T. Yoshihara, T. Nishimura, J. Zhong, S. Akther, A. A. K. M. Fakhrul, M. Liang, C. Higashida, K. Sumi, K. Furuhashi, Y. Inahata, J.-J. Huang, K. Koizumi, S. Yokoyama, T. Tsuji, Y. Petugina, A. Sumarokov, A. B. Salmina, K. Hashida, Y. Kitao, O. Hori, M. Asano, Y.

- Kitamura, T. Kozaka, K. Shiba, F. Zhong, M.-J. Xie, M. Sato, K. Ishihara and H. Higashida (2014). "Anxiety- and depression-like behavior in mice lacking the CD157/BST1 gene, a risk factor for Parkinson's disease." Frontiers in Behavioral Neuroscience **8**(133).
- Lund, D. D., M. M. Knuepfer, M. J. Brody, R. K. Bhatnagar, P. G. Schmid and R. Roskoski (1978). "Comparison of tyrosine hydroxylase and choline acetyltransferase activity in response to sympathetic nervous system activation." Brain Research **156**(1): 192-197.
- Lund, L. M., V. M. Machado and I. G. McQuarrie (2002). "Increased β -Actin and Tubulin Polymerization in Regrowing Axons: Relationship to the Conditioning Lesion Effect." Experimental Neurology **178**(2): 306-312.
- Lyons, P. R. and C. R. Slater (1991). "Structure and function of the neuromuscular junction in young adult mdx mice." J Neurocytol **20**(12): 969-981.
- Magliaro, C., A. L. Callara, G. Mattei, M. Morcinelli, C. Viaggi, F. Vaglini and A. Ahluwalia (2016). "Clarifying CLARITY: Quantitative Optimization of the Diffusion Based Delipidation Protocol for Genetically Labeled Tissue." Front Neurosci **10**: 179.
- Martin, M., J. L. Lefaix, P. Pinton, F. Crechet and F. Daburon (1993). "Temporal modulation of TGF-beta 1 and beta-actin gene expression in pig skin and muscular fibrosis after ionizing radiation." Radiat Res **134**(1): 63-70.
- Masiero, E., L. Agatea, C. Mammucari, B. Blaauw, E. Loro, M. Komatsu, D. Metzger, C. Reggiani, S. Schiaffino and M. Sandri (2009). "Autophagy is required to maintain muscle mass." Cell Metab **10**(6): 507-515.
- Matryba, P., L. Kaczmarek and J. Golab (2019). "Advances in Ex Situ Tissue Optical Clearing." Laser & Photonics Reviews **13**: 1800292.
- McGreevy, J. W., C. H. Hakim, M. A. McIntosh and D. Duan (2015). "Animal models of Duchenne muscular dystrophy: from basic mechanisms to gene therapy." Dis Model Mech **8**(3): 195-213.
- McNamara, J. W. and S. Sadayappan (2018). "Skeletal myosin binding protein-C: An increasingly important regulator of striated muscle physiology." Arch Biochem Biophys **660**: 121-128.
- Milgroom, A. and E. Ralston (2016). "Clearing skeletal muscle with CLARITY for light microscopy imaging." Cell Biol Int **40**(4): 478-483.
- Minsky, M. (1988). "Memoir on inventing the confocal scanning microscope." Scanning **10**(4): 128-138.
- Molbay, M., Z. I. Kolabas, M. I. Todorov, T. L. Ohn and A. Ertürk (2021). "A guidebook for DISCO tissue clearing." Mol Syst Biol **17**(3): e9807.
- Momoi, M. Y. and V. A. Lennon (1984). "The Stability of Solubilized Mammalian Muscle Acetylcholine Receptors During Purification by Monoclonal Immunoabsorption." Journal of Neurochemistry **42**(1): 59-64.
- Muenzer, J. T., C. G. Davis, B. S. Dunne, J. Unsinger, W. M. Dunne and R. S. Hotchkiss (2006). "Pneumonia after cecal ligation and puncture: a clinically relevant "two-hit" model of sepsis." Shock **26**(6): 565-570.
- Munford, R. S. (2006). "Severe sepsis and septic shock: the role of gram-negative bacteremia." Annu Rev Pathol **1**: 467-496.
- Nakamura, K. and S. F. Morrison (2011). "Central efferent pathways for cold-defensive and febrile shivering." J Physiol **589**(Pt 14): 3641-3658.
- Nowak, J. E., K. Harmon, C. C. Caldwell and H. R. Wong (2012). "Prophylactic zinc supplementation reduces bacterial load and improves survival in a murine model of sepsis." Pediatr Crit Care Med **13**(5): e323-329.
- Orellana, R. A., P. M. O'Connor, H. V. Nguyen, J. A. Bush, A. Suryawan, M. C. Thivierge, M. L. Fiorotto and T. A. Davis (2002). "Endotoxemia reduces skeletal muscle protein synthesis in neonates." Am J Physiol Endocrinol Metab **283**(5): E909-916.

- Osler, W. (1892). The principles and practice of medicine : designed for the use of practitioners and students of medicine. New York, D. Appleton and Company.
- Owen, A. M., S. P. Patel, J. D. Smith, B. K. Balasuriya, S. F. Mori, G. S. Hawk, A. J. Stromberg, N. Kuriyama, M. Kaneki, A. G. Rabchevsky, T. A. Butterfield, K. A. Esser, C. A. Peterson, M. E. Starr and H. Saito (2019). "Chronic muscle weakness and mitochondrial dysfunction in the absence of sustained atrophy in a preclinical sepsis model." Elife **8**.
- Patel, S. S., M. Z. Molnar, J. A. Tayek, J. H. Ix, N. Noori, D. Benner, S. Heymsfield, J. D. Kopple, C. P. Kovesdy and K. Kalantar-Zadeh (2013). "Serum creatinine as a marker of muscle mass in chronic kidney disease: results of a cross-sectional study and review of literature." J Cachexia Sarcopenia Muscle **4**(1): 19-29.
- Pawley, J. B. (2006). Handbook of biological confocal microscopy. New York, NY, Springer.
- Piñol-Jurado, P., X. Suárez-Calvet, E. Fernández-Simón, E. Gallardo, N. de la Oliva, A. Martínez-Muriana, P. Gómez-Gálvez, L. M. Escudero, M. Pérez-Peiró, L. Wollin, N. de Luna, X. Navarro, I. Illa and J. Díaz-Manera (2018). "Nintedanib decreases muscle fibrosis and improves muscle function in a murine model of dystrophinopathy." Cell Death Dis **9**(7): 776.
- Píriz, H., N. Nin, J. Boggia, M. Angulo and F. J. Hurtado (2008). "[Salbutamol improves diaphragm force generation in experimental sepsis]." Arch Bronconeumol **44**(3): 135-139.
- Pongratz, G. and R. H. Straub (2014). "The sympathetic nervous response in inflammation." Arthritis Research & Therapy **16**(6): 504.
- Prasher, D. C., V. K. Eckenrode, W. W. Ward, F. G. Prendergast and M. J. Cormier (1992). "Primary structure of the Aequorea victoria green-fluorescent protein." Gene **111**(2): 229-233.
- Qi, Y., T. Yu, J. Xu, P. Wan, Y. Ma, J. Zhu, Y. Li, H. Gong, Q. Luo and D. Zhu (2019). "FDISCO: Advanced solvent-based clearing method for imaging whole organs." Sci Adv **5**(1): eaau8355.
- Randazzo, D., U. Khalique, J. J. Belanto, A. Kenea, D. M. Talsness, J. T. Olthoff, M. D. Tran, K. J. Zaal, K. Pak, I. Pinal-Fernandez, A. L. Mammen, D. Sackett, J. M. Ervasti and E. Ralston (2019). "Persistent upregulation of the β -tubulin tubb6, linked to muscle regeneration, is a source of microtubule disorganization in dystrophic muscle." Hum Mol Genet **28**(7): 1117-1135.
- Remick, D., P. Manohar, G. Bolgos, J. Rodriguez, L. Moldawer and G. Wollenberg (1995). "Blockade of tumor necrosis factor reduces lipopolysaccharide lethality, but not the lethality of cecal ligation and puncture." Shock **4**(2): 89-95.
- Remick, D. G. and P. A. Ward (2005). "Evaluation of endotoxin models for the study of sepsis." Shock **24 Suppl 1**: 7-11.
- Renier, N., Z. Wu, D. J. Simon, J. Yang, P. Ariel and M. Tessier-Lavigne (2014). "iDISCO: a simple, rapid method to immunolabel large tissue samples for volume imaging." Cell **159**(4): 896-910.
- Rhodes, A., L. E. Evans, W. Alhazzani, M. M. Levy, M. Antonelli, R. Ferrer, A. Kumar, J. E. Sevransky, C. L. Sprung, M. E. Nunnally, B. Rochwerg, G. D. Rubenfeld, D. C. Angus, D. Annane, R. J. Beale, G. J. Bellingham, G. R. Bernard, J. D. Chiche, C. Coopersmith, D. P. De Backer, C. J. French, S. Fujishima, H. Gerlach, J. L. Hidalgo, S. M. Hollenberg, A. E. Jones, D. R. Karnad, R. M. Kleinpell, Y. Koh, T. C. Lisboa, F. R. Machado, J. J. Marini, J. C. Marshall, J. E. Mazuski, L. A. McIntyre, A. S. McLean, S. Mehta, R. P. Moreno, J. Myburgh, P. Navalesi, O. Nishida, T. M. Osborn, A. Perner, C. M. Plunkett, M. Ranieri, C. A. Schorr, M. A. Seckel, C. W. Seymour, L. Shieh, K. A. Shukri, S. Q. Simpson, M. Singer, B. T. Thompson, S. R. Townsend, T. Van der Poll, J. L. Vincent, W. J. Wiersinga, J. L. Zimmerman and R. P. Dellinger (2017). "Surviving Sepsis Campaign: International Guidelines for Management of Sepsis and Septic Shock: 2016." Intensive Care Med **43**(3): 304-377.
- Richardson, D. S. and J. W. Lichtman (2015). "Clarifying Tissue Clearing." Cell **162**(2): 246-257.

- Ridgway, E. B. and C. C. Ashley (1967). "Calcium transients in single muscle fibers." Biochem Biophys Res Commun **29**(2): 229-234.
- Rigon, M., S. J. Hörner, T. Straka, K. Bieback, N. Gretz, M. Hafner and R. Rudolf (2020). "Effects of ASC Application on Endplate Regeneration Upon Glycerol-Induced Muscle Damage." Front Mol Neurosci **13**: 107.
- Rittirsch, D., L. M. Hoesel and P. A. Ward (2007). "The disconnect between animal models of sepsis and human sepsis." J Leukoc Biol **81**(1): 137-143.
- Röder, I. V., S. Strack, M. Reischl, O. Dahley, M. M. Khan, O. Kassel, M. Zaccolo and R. Rudolf (2012). "Participation of myosin Va and Pka type I in the regeneration of neuromuscular junctions." PLoS One **7**(7): e40860.
- Rodrigues, A. C. Z., M. L. Messi, Z. M. Wang, M. C. Abba, A. Pereyra, A. Birbrair, T. Zhang, M. O'Meara, P. Kwan, E. I. S. Lopez, M. S. Willis, A. Mintz, D. C. Files, C. Furdui, R. W. Oppenheim and O. Delbono (2019). "The sympathetic nervous system regulates skeletal muscle motor innervation and acetylcholine receptor stability." Acta Physiol (Oxf) **225**(3): e13195.
- Rudd, K. E., S. C. Johnson, K. M. Agesa, K. A. Shackelford, D. Tsoi, D. R. Kievlan, D. V. Colombara, K. S. Ikuta, N. Kissoon, S. Finfer, C. Fleischmann-Struzek, F. R. Machado, K. K. Reinhart, K. Rowan, C. W. Seymour, R. S. Watson, T. E. West, F. Marinho, S. I. Hay, R. Lozano, A. D. Lopez, D. C. Angus, C. J. L. Murray and M. Naghavi (2020). "Global, regional, and national sepsis incidence and mortality, 1990-2017: analysis for the Global Burden of Disease Study." Lancet **395**(10219): 200-211.
- Rudolf, R. and T. Straka (2019). "Nicotinic acetylcholine receptor at vertebrate motor endplates: Endocytosis, recycling, and degradation." Neuroscience Letters **711**: 134434.
- Sarveswaran, J., N. M. Orsi, M. Cummings, S. Homer-Vanniasinkam and D. Burke (2012). "GAPDH: is it a reliable housekeeper gene to use in sepsis research?" Critical Care **16**(Suppl 3): P107-P107.
- Schabbauer, G. (2012). "Polymicrobial sepsis models: CLP versus CASP." Drug Discovery Today: Disease Models **9**(1): e17-e21.
- Schefold, J. C., J. Bierbrauer and S. Weber-Carstens (2010). "Intensive care unit-acquired weakness (ICUAW) and muscle wasting in critically ill patients with severe sepsis and septic shock." J Cachexia Sarcopenia Muscle **1**(2): 147-157.
- Schefold, J. C., T. Wollersheim, J. J. Grunow, M. M. Luedi, W. J. Z'Graggen and S. Weber-Carstens (2020). "Muscular weakness and muscle wasting in the critically ill." J Cachexia Sarcopenia Muscle **11**(6): 1399-1412.
- Schiaffino, S. and C. Reggiani (2011). "Fiber types in mammalian skeletal muscles." Physiol Rev **91**(4): 1447-1531.
- Shah, A. A., D. Kulkarni, Y. Ingale, A. V. Koshy, S. Bhagalia and N. Bomble (2017). "Kerosene: Contributing agent to xylene as a clearing agent in tissue processing." J Oral Maxillofac Pathol **21**(3): 367-374.
- Shimomura, O. (1995). "A Short Story of Aequorin." Biological Bulletin **189**(1): 1-5.
- Shrum, B., R. V. Anantha, S. X. Xu, M. Donnelly, S. M. Haeryfar, J. K. McCormick and T. Mele (2014). "A robust scoring system to evaluate sepsis severity in an animal model." BMC Res Notes **7**: 233.
- Silveira, W. A., D. A. Gonçalves, F. A. Graça, A. L. Andrade-Lopes, L. B. Bergantin, N. M. Zanon, R. O. Godinho, I. C. Kettelhut and L. C. C. Navegantes (2014). "Activating cAMP/PKA signaling in skeletal muscle suppresses the ubiquitin-proteasome-dependent proteolysis: implications for sympathetic regulation." Journal of Applied Physiology **117**(1): 11-19.
- Silvestri, L., I. Costantini, L. Sacconi and F. S. Pavone (2016). "Clearing of fixed tissue: a review from a microscopist's perspective." J Biomed Opt **21**(8): 081205.
- Skorna, M., R. Kopacik, E. Vlckova, B. Adamova, M. Kostalova and J. Bednarik (2015). "Small-nerve-fiber pathology in critical illness documented by serial skin biopsies." Muscle Nerve **52**(1): 28-33.

- Sordi, R., O. Menezes-de-Lima, A. M. Della-Justina, E. Rezende and J. Assreuy (2013). "Pneumonia-induced sepsis in mice: temporal study of inflammatory and cardiovascular parameters." *Int J Exp Pathol* **94**(2): 144-155.
- Spalteholz, W. (1914). Über das durchsichtigmachen von menschlichen und tierischen präparaten und seine theoretischen bedingungen. n.p.
- Starr, M. E., A. M. Steele, M. Saito, B. J. Hacker, B. M. Evers and H. Saito (2014). "A new cecal slurry preparation protocol with improved long-term reproducibility for animal models of sepsis." *PLoS One* **9**(12): e115705.
- Steele, A. M., M. E. Starr and H. Saito (2017). "Late Therapeutic Intervention with Antibiotics and Fluid Resuscitation Allows for a Prolonged Disease Course with High Survival in a Severe Murine Model of Sepsis." *Shock* **47**(6): 726-734.
- Stevens, R. D., S. A. Marshall, D. R. Cornblath, A. Hoke, D. M. Needham, B. de Jonghe, N. A. Ali and T. Sharshar (2009). "A framework for diagnosing and classifying intensive care unit-acquired weakness." *Crit Care Med* **37**(10 Suppl): S299-308.
- Straka, T., C. Schröder, A. Roos, L. Kollipara, A. Sickmann, M. P. I. Williams, M. Hafner, M. M. Khan and R. Rudolf (2021). "Regulatory Function of Sympathetic Innervation on the Endo/Lysosomal Trafficking of Acetylcholine Receptor." *Frontiers in Physiology* **12**(221).
- Suffredini, A. F. and R. J. Noveck (2014). "Human endotoxin administration as an experimental model in drug development." *Clin Pharmacol Ther* **96**(4): 418-422.
- Susaki, E. A., K. Tainaka, D. Perrin, H. Yukinaga, A. Kuno and H. R. Ueda (2015). "Advanced CUBIC protocols for whole-brain and whole-body clearing and imaging." *Nature Protocols* **10**(11): 1709-1727.
- Tainaka, K., S. I. Kubota, T. Q. Suyama, E. A. Susaki, D. Perrin, M. Ukai-Tadenuma, H. Ukai and H. R. Ueda (2014). "Whole-body imaging with single-cell resolution by tissue decolorization." *Cell* **159**(4): 911-924.
- Toga, A. W., K. L. Ambach and S. Schluender (1994). "High-resolution anatomy from in situ human brain." *Neuroimage* **1**(4): 334-344.
- Tortora, G. J. and B. Derrickson (2012). Principles of anatomy & physiology. Hoboken, NJ, Wiley.
- Tsai, P. S., P. Blinder, B. J. Migliori, J. Neev, Y. Jin, J. A. Squier and D. Kleinfeld (2009). "Plasma-mediated ablation: an optical tool for submicrometer surgery on neuronal and vascular systems." *Curr Opin Biotechnol* **20**(1): 90-99.
- Tsukagoshi, H., T. Morita, K. Takahashi, F. Kunimoto and F. Goto (1999). "Cecal ligation and puncture peritonitis model shows decreased nicotinic acetylcholine receptor numbers in rat muscle: immunopathologic mechanisms?" *Anesthesiology* **91**(2): 448-460.
- Tu, W. Y., W. Xu, K. Zhang and C. Shen (2020). "Whole-mount staining of neuromuscular junctions in adult mouse diaphragms with a sandwich-like apparatus." *J Neurosci Methods* **350**: 109016.
- Tungtur, S. K., N. Nishimune, J. Radel and H. Nishimune (2017). "Mouse Behavior Tracker: An economical method for tracking behavior in home cages." *Biotechniques* **63**(5): 215-220.
- van der Poll, T. (2012). "Preclinical sepsis models." *Surg Infect (Larchmt)* **13**(5): 287-292.
- Vary, T. C. and S. R. Kimball (1992). "Sepsis-induced changes in protein synthesis: differential effects on fast- and slow-twitch muscles." *Am J Physiol* **262**(6 Pt 1): C1513-1519.
- Wagenlehner, F. M., A. Pilatz and W. Weidner (2011). "Urosepsis--from the view of the urologist." *Int J Antimicrob Agents* **38** Suppl: 51-57.
- Wehrli, H. F., I. Bezrukov, S. Wiehr, M. Lehnhoff, K. Fuchs, J. G. Mannheim, L. Quintanilla-Martinez, U. Kohlhofer, M. Kneilling, B. J. Pichler and A. W. Sauter (2015). "Assessment of murine brain tissue shrinkage caused by different histological fixatives using magnetic resonance and computed tomography imaging." *Histol Histopathol* **30**(5): 601-613.

- Wei, Y., Y. Liang, H. Lin, Y. Dai and S. Yao (2020). "Autonomic nervous system and inflammation interaction in endometriosis-associated pain." Journal of Neuroinflammation **17**(1): 80.
- Wichterman, K. A., A. E. Baue and I. H. Chaudry (1980). "Sepsis and septic shock--a review of laboratory models and a proposal." J Surg Res **29**(2): 189-201.
- Williams, M. P. I., M. Rigon, T. Straka, S. J. Hörner, M. Thiel, N. Gretz, M. Hafner, M. Reischl and R. Rudolf (2019). "A Novel Optical Tissue Clearing Protocol for Mouse Skeletal Muscle to Visualize Endplates in Their Tissue Context." Front Cell Neurosci **13**: 49.
- Wright, C. J., J. H. Duff, A. P. McLean and L. D. MacLean (1971). "Regional capillary blood flow and oxygen uptake in severe sepsis." Surg Gynecol Obstet **132**(4): 637-644.
- Xu, N., A. Tamadon, Y. Liu, T. Ma, R. K. Leak, J. Chen, Y. Gao and Y. Feng (2017). "Fast free-of-acrylamide clearing tissue (FACT)—an optimized new protocol for rapid, high-resolution imaging of three-dimensional brain tissue." Scientific Reports **7**(1): 9895.
- Yin, X., T. Yu, B. Chen, J. Xu, W. Chen, Y. Qi, P. Zhang, Y. Li, Y. Kou, Y. Ma, N. Han, P. Wan, Q. Luo, D. Zhu and B. Jiang (2019). "Spatial Distribution of Motor Endplates and its Adaptive Change in Skeletal Muscle." Theranostics **9**(3): 734-746.
- Zantl, N., A. Uebe, B. Neumann, H. Wagner, J.-R. Siewert, B. Holzmann, C.-D. Heidecke and K. Pfeffer (1998). "Essential role of gamma interferon in survival of colon ascendens stent peritonitis, a novel murine model of abdominal sepsis." Infection and immunity **66**(5): 2300-2309.
- Zhang, W. L., S. H. Liu, W. C. Zhang, W. Hu, M. Jiang, A. Tamadon and Y. Feng (2018). "Skeletal Muscle CLARITY: A Preliminary Study of Imaging The Three-Dimensional Architecture of Blood Vessels and Neurons." Cell J **20**(2): 132-137.
- Zimmermann, T., J. Rietdorf, A. Girod, V. Georget and R. Pepperkok (2002). "Spectral imaging and linear un-mixing enables improved FRET efficiency with a novel GFP2–YFP FRET pair." FEBS letters **531**(2): 245-249.
- Zolfaghari, P. S., B. B. Pinto, A. Dyson and M. Singer (2013). "The metabolic phenotype of rodent sepsis: cause for concern?" Intensive Care Medicine Experimental **1**(1): 6.

9. Curriculum Vitae and Publications

Marion Patrick Ivey Williams

Marion@g.clemson.edu

Pfalzplatz 4

68163 Mannheim

(+49) 152 03455629 (DE Cell)

+1 (843) 907-2747 (US Cell)

Nationality: American



Education

PhD focus in microscopy and animal models, Universität Heidelberg, Sept. 2016 - Present

Thesis: Characterization of muscle tissue in sepsis induced mouse models

Master in Biotechnology, Mannheim University of Applied Sciences, Sept. 2014 - Aug. 2016

Thesis: Tissue clearing optimization for structural changes in skeletal muscle

Final mark: 1.6 (German scale)

Bachelor of Science in Biological Sciences, Clemson University, SC (U.S.), May 2010

GPA: 3.37 of 4.0 (U.S. scale)

North Greenville University, Tigerville, SC (U.S.), Majored in Biology, 2005 - May 2008

Carvers Bay High School, Georgetown, SC (U.S.), Class of 2005

Work Experience

Medizinische Fakultät Mannheim, Universität Heidelberg, Mannheim, Fellowship, Sept. 2016 - Present

Research in novel tissue clearing methods, staining protocols, and imaging using confocal and digital light sheet microscopy (DLS)

Research in establishing acute and chronic septic models to study the effects on muscle tissue

Responsible for setting up, training, and troubleshooting users on confocal and DLS microscopes

Help others with various tissue clearing methods and post processing of microscopy data

Responsible for setting up, expanding, streamlining, and maintaining 100 TB cloud storage solution

Responsible for building and maintaining PCs for microscopy data processing and analysis

Nutra Manufacturing, Anderson, SC (U.S.), Quality Control Chemist, Jan. 2011- Aug. 2014

Responsible for a sundry of assays with emphasis on iodine via ICP-MS and UV-Vis items

Perform routine maintenance and monthly calibration checks on lab equipment

Place orders for the solutions and standards used every month

Troubleshoot standard protocols if problems arise with testing

Run various types of analytical lab equipment including: Physical testing, dissolution,

disintegration, Auto-Titrator, IR, UV-Vis, ICP-MS, ICP, HPLC, and TLC

Required to follow GMP as well GLP protocol to insure compliance with FDA and other

global regulatory bodies

Creation and validation of a new ICP-MS method for the detection of Iodine

Jordan Labs, Clemson University, Clemson, SC (U.S.), Teaching Assistant, Aug. 2009 - May 2010

Courses taught: Comparative Physiology and Systems Physiology
Make various chemical compounds used in a lab setting
Teach students a variety of different research and lab techniques
Grade papers and other documents that are submitted by students

Creative Inquiry and Undergraduate Research, May 2009 - May 2010

Data compilation in turtle biomechanics project
Sample collection, cataloging, and literature review for butterfly distribution

Publications

Straka T, Schröder C, Roos A, Kollipara L, Sickmann A, **Williams MPI**, Hafner M, Khan MM, Rudolf R. Regulatory Function of Sympathetic Innervation on the Endo/Lysosomal Trafficking of Acetylcholine Receptor. *Front Physiol.* 2021 Mar 11;12:626707. doi: 10.3389/fphys.2021.626707. PMID: 33776791; PMCID: PMC7991846.

Williams, M., Rigon, M., Straka, T., Hörner, S. J., Thiel, M., Gretz, N., ... Rudolf, R. (2019). A Novel Optical Tissue Clearing Protocol for Mouse Skeletal Muscle to Visualize Endplates in Their Tissue Context. *Frontiers in cellular neuroscience*, 13, 49. doi:10.3389/fncel.2019.00049

Straka, T., Vita, V., Prokshi, K., Hörner, S. J., Khan, M. M., Pirazzini, M., **Williams, M.**, ... Rudolf, R. (2018). Postnatal Development and Distribution of Sympathetic Innervation in Mouse Skeletal Muscle. *International journal of molecular sciences*, 19(7), 1935. doi:10.3390/ijms19071935

Certifications

FELASA B certified (Laboratory Animal Science and Methods of Animal Experimentation)
SAS Certified Base Programmer for SAS 9

Skills

Experienced with various types of analytical lab equipment, cell based techniques, PCR, Western Blotting, Microplate readers, and corresponding software
Knowledge of Labworks, I-5, Onbase, Total Chrome, Mymstat, Logger Pro, Microsoft Office Suite, Adobe Suite, Huygens SVI, Leica LAS-X, ImageJ, and Fusion
Advanced knowledge of confocal and light sheet microscopy, tissue clearing, and tissue staining techniques
Research experience in establishing and validating mouse animal models
Research experience in the sympathetic innervation of muscle tissue and its close relationship to ICUAW in the critically ill
Research experience in animal biomechanics and butterfly distribution ecology
Experienced with using Infrared cameras to track animal activity levels
Experience with Autodesk Inventor for 3D modeling and Cura for FDM style printing
Proficient with Windows and Mac operating systems

Above average team building and leadership skills
Above average analytical thinking and problem solving

Achievements

Cellular Neuropathology Editor's Pick 2021 for "A Novel Optical Tissue Clearing Protocol for Mouse Skeletal Muscle to Visualize Endplates in Their Tissue Context."

References

Prof. Dr. rer. nat. Rüdiger Rudolf
Faculty of Biotechnology Mannheim University of Applied Sciences
Interdisciplinary Center of Neurosciences (IZN), University of Heidelberg
r.rudolf@hs-mannheim.de

Prof. Dr. med. Manfred Thiel
Director of Anästhesiologie und Operative Intensivmedizin, Universitätsklinikum Mannheim
Manfred.Thiel@medma.uni-heidelberg.de

PD Dr. rer. nat. Christian Witt
Medizinische Fakultät Mannheim der Universität Heidelberg
Klinik für Anästhesie und Operative Intensivmedizin
Christian.Witt@medma.uni-heidelberg.de

10. Acknowledgements

My personal love for microscopy and the intricacies of muscle helped drive me to the completion of my PhD. Though, none of this would have been possible without the help, support, and knowledge gained from many of the wonderful people I have met along this rather tough journey. Therefore, I would like to thank Prof. Dr. med. Thiel for his guidance, financial support, and critical input for the completion and evaluation of the sepsis aspects of my project. I would also like to thank Prof. Dr. rer. nat. Rudolf for his financial support, vast knowledge of microscopy which he instilled in me, and the guidance I received from him. Lastly, this work would not be possible without PD Dr. med. Tsagogiorgas, who provided vital input and dedication to the establishment of the sepsis model and PD Dr. rer. nat. Witt who helped guide me through ICU- acquired weakness and its relation to sepsis.

I am also very grateful for the help of the many others who went through this process with me and provided advice and assistance with all aspects of my project. Specifically, Tatjana, Sarah, and Franziska for their help with many experiments at Hochschule Mannheim. Elina for helping me adjust to Mannheim life and showing me the great aspects and hidden places in the city. Matteo for introducing me to the wonderful aspects of Italy, his support in the lab, and his patience with me for still pronouncing his name incorrectly at times. Alex for his friendship and analytical knowledge. Max for his immunology knowledge and all the beers shared. Diego for all the exciting trips we took together and the great advice and help I received. Laura for the invaluable help she provided running and establishing the sepsis model. Sina for her extraordinary help throughout this process, as well as the support given from the animal house, ZMF, and the Anästhesiologie research group at the clinic.

I also want to give a special thanks to my family and friends back home, as the love and emotional support they provided made this possible and the homesickness bearable. Though the loss of my grandparents, Dr. Benton Williams, Sam Grayson, and Barbara Grayson during this period made it extremely difficult at times, their overwhelming love, support, and the occasional fried shrimp will never be forgotten. Lastly, I would like to thank Kathrin, for her overwhelming love and support, as I would have surly failed without her continued belief in me even when I did not believe in myself and Rigby, for all his licks, emotional support, and insight that, life is not just work and worry and sometimes, you have to take a moment to stop and sniff the roses.